UC San Diego
UC San Diego Electronic Theses and Dissertations

Title

Lung tumor tracking, trajectory reconstruction, and motion artifact removal using rotational cone-beam projections

Permalink

Author

Lewis, John Henry

Publication Date

2010

Peer reviewed|Thesis/dissertation

UNIVERSITY OF CALIFORNIA, SAN DIEGO

Lung Tumor Tracking, Trajectory Reconstruction, and Motion Artifact Removal
using Rotational Cone-Beam Projections

A dissertation submitted in partial satisfaction of the requirements for the
degree of Doctor of Philosophy

in

Physics (Biophysics)

by

John Henry Lewis

Committee in charge:

        Professor Steve B. Jiang, Chair
        Professor Herbert Levine, Co-Chair
        Professor Hans P. Paar
        Professor Todd A. Pawlicki
        Professor Clifford M. Surko

2010

This dissertation of John Henry Lewis is approved, and it is acceptable in

quality and form for publication on microfilm and electronically:

Co-Chair

Chair

University of California, San Diego

2010

Dedicated to

my wife
Jennifer Christina Lewis

and

my mother
Cathryn McDonald Lewis

Table of Contents

List of Figures

List of Tables

List of Abbreviations

1D	One-dimensional
2D	Two-dimensional
3D	Three-dimensional
4D	Four-dimensional
4DCT	Four-dimensional Computed Tomography
AP	Anterior-posterior
CBCT	Cone-Beam Computed Tomography
CT	Computed Tomography
DC	Duty Cycle
DRR	Digitally Reconstructed Radiograph
e_{95}	95th Percentile Absolute Error
e_{rms}	Root Mean Square Error
HU	Hounsfield Units
IMRT	Intensity-Modulated Radiation Therapy
LR	Left-right
MI	Mutual Information
NCAT	NURBS-based Cardiac-Torso
NCC	Normalized Cross Correlation
NMI	Normalized Mutual Information
NMSE	Normalized Mean Squared Error

NURBS	Non-Uniform Rational B-Spline
PDF	Probability Density Function
ROI	Region of Interest
SI	Superior-inferior
SSD	Sum of Squared Difference
TV	Total Variation
VMAT	Volumetric Modulated Arc Therapy
VOI	Volume of interest

Acknowledgements

I would like to acknowledge Dr. Steve B. Jiang for serving as my adviser, and for introducing me to the field of medical physics. Dr. Jiang is an exemplary mentor in every sense. His guidance has helped me grow as a person and a scientist. Any success I have in this field I owe to him.

I would also like to thank the entire "CART" research team for help, collaboration, inspiration, and friendship during my time as a graduate student. In particular I would like to thank Dr. Ruijiang Li for his patience through the endless questions I asked him. Without the many hours Dr. Li spent helping me, I might never have graduated.

I would also like to express my gratitude to Dr. Herbert Levine for serving as the co-chair of my committee, and to the University of California, San Diego Physics Department for allowing me to pursue my interests in Medical Physics. Additionally, I would like to thank Dr. Hans P. Paar, Dr. Todd A. Pawlicki, and Dr. Clifford M. Surko for serving on my committee.

Chapter 4 contains material being prepared for publication. Lewis, John H.; Li, Ruijiang; Jia, Xun; Watkins, W. Tyler; Song, William Y.; Jiang, Steve B. The dissertation author was the primary investigator and author of this material.

Vita

Education

2004 B.A.	Physics	Occidental College
summa cum laude	GPA 3.94/4.00	Los Angeles, CA
2007 M.S.	Physics	University of California, San Diego
	GPA 4.00/4.00	La Jolla, CA
2010 Ph.D.	Physics	University of California, San Diego
	GPA 4.00/4.00	La Jolla, CA

Professional Appointments

2006-2009	Teaching Assistant	University of California, San Diego
2007-2010	Research Assistant	University of California, San Diego
2010	Instructor	Harvard Medical School, Boston

Honors and Awards

2005-2009	Eugene Cota-Robles Fellowship
2004	Phi Beta Kappa Honor Society

Journal Papers

JH Lewis, R Li, WT Watkins, JD Lawson, WP Segars, LI Cerviño, WY Song, SB Jiang, Markerless lung tumor tracking and trajectory reconstruction in rotational cone-beam projections, Phys. Med. Biol. 55(9): 2505-2522, 2010.

JH Lewis and SB Jiang, A theoretical model for respiratory motion artifacts in free breathing CT scans, *Phys. Med. Biol.* 54(3): 745–755, 2009.

R Li, JH Lewis, Real-time volumetric image reconstruction and 3D tumor localization based on a single x-ray projection image for lung cancer radiotherapy, *Med. Phys.* (accepted 2010).

R Li, JH Lewis, LI Cerviño, and SB Jiang, 4D CT sorting based on patient internal anatomy, *Phys. Med. Biol.* 54(15): 4821-4833, 2009.

R Li, JH Lewis, LI Cerviño, and SB Jiang, A feasibility study of markerless fluoroscopic gating for lung cancer radiotherapy using 4DCT templates, *Phys. Med. Biol.* 54(20): N489-N500, 2009.

N Tyagi, JH Lewis, CM Yashar, D Vo, LK Mell, SB Jiang, AJ Mundt, Impact of internal organ motion and deformation on target coverage in intact cervical cancer patients undergoing IMRT: A daily cone-beam CT study, *Int. J. Radiat. Oncol. Biol. Phys.* (submitted 2009).

WT Watkins, R Li, JH Lewis, A Sandhu, SB Jiang, WY Song, Patient-specific internal target volume margin assessment during four-dimensional computed tomography of lung cancer, *Phys. Med. Biol.* (accepted 2010).

X Jia, Y Lou, JH Lewis, R LI, X Gu, C Men, WY Song, SB Jiang, GPU-based fast low-dose cone-beam CT reconstruction via Total Variation, *Med. Phys.* (submitted 2010).

Y Liang, BS Rose, KM Messer, JH Lewis, SB Jiang, CM Yashar, AJ Mundt LK Mell, The impact of bone marrow radiation dose on acute hematologic toxicity in cervical cancer: principal components analysis on high dimensional data, *Int. J. Radiat. Oncol. Biol. Phys.* (accepted 2009).

DP Cruikshank, TR Geballe, TC Owen, CM Dalle Ore, TL Roush, RH Brown, JH Lewis, Search for the 3.4-μm C-H Bands on Low-Albedo Asteroids, *Icarus* 156: 434-441, 2002.

ABSTRACT OF THE DISSERTATION

Lung Tumor Tracking, Trajectory Reconstruction, and Motion Artifact Removal using Rotational Cone-Beam Projections

by

John Henry Lewis

Doctor of Philosophy in Physics (Biophysics)

University of California, San Diego, 2010

Professor Steve B. Jiang, Chair
Professor Herbert Levine, Co-Chair

Management of lung tumor motion is a challenging and important problem for modern, highly conformal radiotherapy. Poorly managed tumor motion can lead to imaging artifacts, poor target coverage, and unnecessarily high dose to normal tissues. The goals of this dissertation are to develop a real-time localization algorithm that is applicable to rotational cone-beam projections acquired during regular (~60 seconds) cone-beam computed

tomography (CBCT) scans, and to use these tracking results to reconstruct a tumor's trajectory, shape and size immediately prior to treatment.

Direct tumor tracking is performed via a multiple template matching algorithm where templates are derived from digitally reconstructed radiographs (DRRs) generated from four-dimensional computed tomography (4DCT). Three-dimensional (3D) tumor trajectories are reconstructed by binning two-dimensional (2D) tracking results according to their corresponding respiratory phases. Within each phase bin a point is calculated approximating the 3D tumor position, resulting in a 3D phase-binned trajectory. These 3D trajectories are used to construct motion blurring functions which are in turn used to remove motion blurring artifacts from reconstructed CBCT volumes with a deconvolution algorithm. Finally, the initial direct tracking algorithm is combined with diaphragm-based tracking to develop a more robust "combined" tracking algorithm.

Respiratory motion phantoms (digital and physical), and example patient cases were used to test each technique. Direct tumor tracking performed well for both phantom cases, with sub-millimeter root mean square error (e_{rms}) in the axial and tangential imager dimensions. In patient studies the algorithm performed well for many angles, but exhibited large errors for some projections. Accurate 3D trajectories were successfully reconstructed for patients and phantoms. Errors in reconstructed trajectories were smaller than the errors in the direct tracking results in all cases. The deblurring algorithm

performed excellently in phantom studies. Deblurring was also effective on an example patient case, though the benefits were less stark. Finally, the combined tracking algorithm performed equally to or better than direct tumor tracking in the phantom and patient cases examined. While the preliminary results for each technique are promising, the algorithms must be tested on a larger data set with well defined ground truth to investigate potential clinical applications.

1.   Introduction

1.1. Overview of Radiation Therapy

Along with chemotherapy and surgery, radiation therapy is one of the three main modalities of cancer treatment. Radiation can be used with either palliative or curative purpose, and is often combined with other treatments. It can be used in many situations where surgery is not an acceptable option due to risks of complication. It is estimated that radiation is incorporated into the treatments of over 50% of cancer patients (Van Dyk 1999).

The purpose of radiation therapy is to deliver sufficient dose to the malignant tissue (target) while minimizing the dose to normal, healthy tissues. Radiation damages cells by creating free radicals within a cell which in turn interact with and damage DNA, harming a cell's ability to multiply. While in general cancer cells are less able to repair the damage caused by radiation than normal cells, damage to normal tissues can still cause severe complications, so it is essential to minimize the dose to healthy tissue (Hall and Giaccia 2006).

The most common type of radiation therapy is external beam radiation therapy. A compact linear accelerator mounted on a gantry that can rotate around the patient is used to deliver a high energy beam to the patient. An electron gun produces an electron beam which is accelerated to high energy, typically in the 4-20 MeV range. This beam is aimed toward the patient with a bending magnet. The electron beam collides with a tungsten target, stopping the electrons and producing bremsstrahlung radiation. This photon beam passes through a system of beam modulators and shapers to create a beam which then enters the patient. An image of a typical linear accelerator is showed in Figure 1.1.

Since radiation can cause significant harm to normal tissues, much work is done during the radiation therapy process in an attempt to achieve an optimal balance between sufficient dose to the target and minimal dose to healthy tissues. The radiation therapy process will be discussed in more detail in the following sections, but will be explained briefly here. The first step in treating a patient who has been prescribed radiation is to build a patient model upon which the treatment can be planned. This phase of the radiation therapy process is called treatment simulation, and is usually based around a computed tomography (CT) scan. Other imaging modalities such as nuclear magnetic resonance imaging (MRI) or positron emission tomography (PET) are sometimes also incorporated (Van Dyk 1999). The simulation scan is used to define relationships between the target and important normal critical

structures. These relationships are used during the next phase of radiation therapy, treatment planning. In treatment planning, the patient model is input into software which also models the treatment machine that will be used. An interactive optimization procedure is used to determine the best beam angles, shapes, and intensities to use in order to deliver a dose which conforms tightly to the target, and does not surpass tolerable dose levels for critical structures. Together, treatment simulation and planning compose the treatment preparation piece of the radiation therapy process. The next piece is treatment execution.

During treatment execution, the patient will return for treatment multiple times, each time receiving a fraction of their total prescribed dose. The first step in each treatment fraction is patient positioning, where the patient must be positioned carefully under the treatment machine in order to match the reference geometry established during treatment planning as closely as possible. Since modern radiation technologies allow for a highly conformal dose to be delivered to the target, there is a significant risk of partially missing and under-dosing the target if the patient is not positioned correctly. Several imaging modalities can be used to assist in this process, with the state of the art currently being a cone-beam CT (CBCT) scanner mounted on the treatment machine. Once the patient has been positioned, the last step is to turn on the radiation beam and deliver the treatment. During treatment delivery, it is important to monitor the patient to ensure that the reference

geometry established during treatment planning (and matched during patient setup) is maintained throughout the treatment.

Organ and target motions cause significant challenges in each step of the radiation therapy process. Motion can occur both between treatments (interfraction motion) and during treatments (intrafraction motion), and has a variety of causes including the cardiac, respiratory, and gastrointestinal systems, weight loss, tumor shrinkage, and skeletal muscular motion. Motion can cause significant artifacts in the imaging modalities used during treatment simulation (Balter *et al* 1996, Nehmeh *et al* 2002, Caldwell *et al* 2003, Taguchi 2003, Chen *et al* 2004, Lewis and Jiang 2009). Optimized treatment planning must account for an expected amount of organ motion. Accurate patient setup should account for deformations in patient anatomy, and the target's motion should be monitored and accounted for during treatment delivery. In general, failure to account for organ motion at the various steps in the radiation process can result in both an under-dosing of the target and in increased dose to normal tissues.

Respiratory motion is a particularly challenging type of motion to manage, and will be the primary focus of this dissertation. Lung tumors have been measured to exhibit superior-inferior (SI) motion of as large as 5.0 cm, and breathing patterns which vary both between and during treatment fractions (Keall *et al* 2006). Many lung patients have compromised lung function, so it is impractical to ask them to hold their breath for extended

periods of time while receiving treatment. In the United States, lung cancer is the third most common cancer, but is the leading cause of cancer death, as is shown in Figure 1.2 (Group 2009). There is a great need for more effective lung cancer therapies. Better motion management during radiation therapy could allow for increased dose to be delivered to lung tumors, and there is clinical evidence to suggest that increased dose to lung tumors provides advantage to local control and survival rates (Perez *et al* 1980, Choi and Doucette 1981, Perez *et al* 1987, Okunieff *et al* 1995, Martel *et al* 1999, McGarry *et al* 2005, Wulf *et al* 2005). In the ensuing sections, I will give more detail on each step of the radiation process, with specific focus given to the challenges caused by respiratory motion.

Figure 1.1: A linear accelerator used to treat patients at the University of California, San Diego.

Top 10 Cancer Sites: 2005, Male and Female, United States—All Races

Cancer Site	Rate per 100,000
Prostate	142.4
Female Breast	117.7
Lung & Bronchus	67.7
Colon & Rectum	48.3
Corpus & Uterus, NOS	23.4
Urinary Bladder	21.1
Non-Hodgkin Lymphoma	18.9
Melanomas of the Skin	18.5
Kidney & Renal Pelvis	14.5
Ovary	12.4

Rates per 100,000‡

Top 10 Cancer Sites: 2005, Male and Female, United States—All Races

Cancer Site	Rate per 100,000
Lung & Bronchus	52.8
Prostate	24.7
Female Breast	24.0
Colon & Rectum	17.4
Pancreas	10.8
Ovary	8.6
Leukemias	7.2
Non-Hodgkin Lymphoma	6.9
Liver & IBD	5.3
Esophagus	4.4

Rates per 100,000†
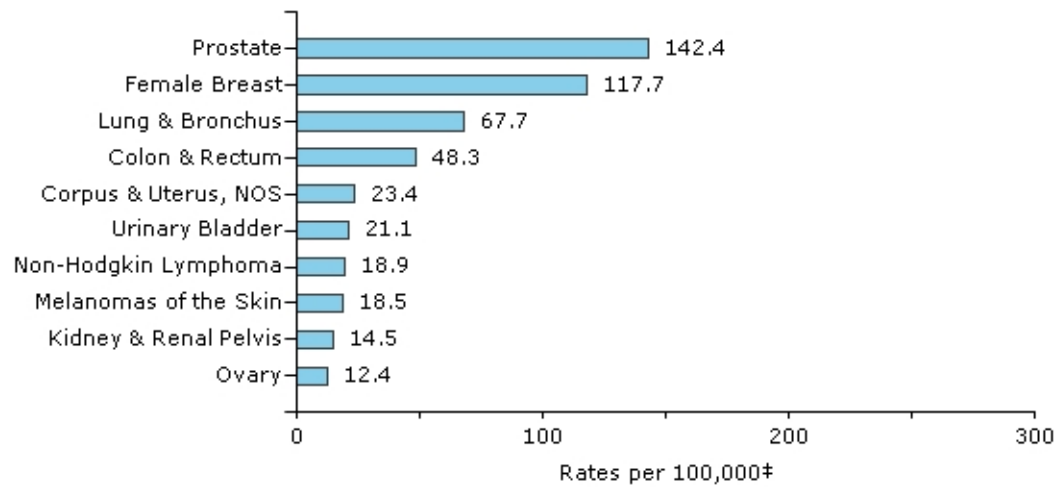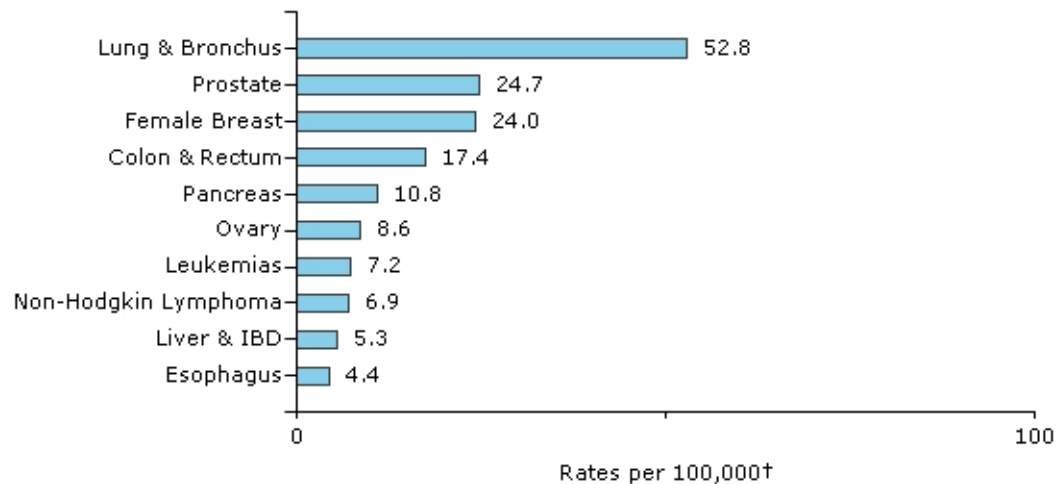
Figure 1.2: Charts showing the incidence (above) and death (below) rates for cancer in the United States. Both breast and prostate cancer are more common than lung cancer, but lung cancer causes the most deaths. Courtesy of the Center for Disease Control.

1.2. Treatment Simulation

Historically, treatment simulation could be based on orthogonal radiographs or clinical examination, but now it almost always is based on a CT

scan. A CT scanner uses an x-ray source and a line of detectors which rotate around the patient's long axis, as illustrated by Figure 1.3. A series of projections are acquired by the detector, with each projection measuring the linear attenuation of the photon beam along the path connecting the source to the detector, as governed by the Beer-Lambert Law. These projections are used to reconstruct a slice of a patient's anatomy using a filtered back projection algorithm (Kak *et al* 1988). This procedure is repeated slice by slice for a patient until the entire volume is reconstructed.

Respiratory motion can cause lung tumors and other organs to appear severely distorted in reconstructed CT volumes (Balter *et al* 1996, Chen *et al* 2004). Conventional reconstruction algorithms generally assume that the volume being reconstructed is static, so objects that move substantially during projection acquisition are not reconstructed accurately. In some cases tumor motion and the corresponding artifacts can be suppressed by asking the patient to hold her breath during image acquisition (Dawson *et al* 2001, Cheung *et al* 2003, Berson *et al* 2004). However, lung cancer patients with compromised lung function often cannot tolerate this type of breathing restriction. Sometimes the acquisition parameters of a free-breathing CT scan can be adjusted to minimize motion artifacts, but the utility of this method is somewhat limited as it relies on some prior knowledge or assumptions about a tumor's motion (Lewis and Jiang 2009).

Ideally, one would like to reconstruct not just a single, artifact free image of a patient's anatomy, but a movie or several frames showing how the patient's anatomy moves during respiratory motion. A recent technology that attempts to achieve this is four-dimensional CT (4DCT). During 4DCT a surrogate for a patient's breathing motion is also recorded as projections are being acquired. Common breathing surrogates include the motion of a patient's abdomen, or a patient's tidal volume as measured by a spirometer (Ford *et al* 2003, Low *et al* 2003, Vedam *et al* 2003a, Keall *et al* 2004, Mageras *et al* 2004). As each CT slice is reconstructed, it is tagged with the corresponding respiratory data. Each slice of a patient is oversampled so that several slices exist for the same location in the patient, representing different pieces of the breathing cycle. Once all slices are acquired a sorting algorithm is used to bin each slice into a representative piece of the breathing cycle. Most commonly a patient's breathing cycle is divided into ten phases ranging from max exhale (0%, phase bin 1) to max inhale (50%, phase bin 6) back to just before max exhale(90%, phase bin 10), and slices are assigned to each bin based on which phase of the breathing cycle they were acquired during. It is also possible to sort into bins based on the amplitude of the breathing motion, and recently our research group has developed a method for sorting 4DCT based only on internal information stored in the projections, without the need for an external respiratory signal (Li *et al* 2009a). When every slice has been sorted into its corresponding bin, the result is several CT volumes

corresponding to different pieces of the breathing cycle. Together, these volumes can be considered to form the frames a video which shows how a patient's anatomy deforms with respiratory motion.

A significant limitation of 4DCT is that it assumes a regular periodic motion for a patient's breathing pattern. If a patient breathes irregularly, the sorting algorithm may bin together slices representing different deformations of the patient's anatomy. These binning errors can result in unrealistic discontinuities or deformations in the reconstructed volume (Keall *et al* 2004, Abdelnour *et al* 2007, Starkschall *et al* 2007, Li *et al* 2009a). In many cases these artifacts can be minimized by using breathing-coaching, where a patient is coached via visual or audio cues as to when and how deeply to breath (Kini *et al* 2003, Haasbeek *et al* 2008, Spoelstra *et al* 2008, Nakamura *et al* 2009).
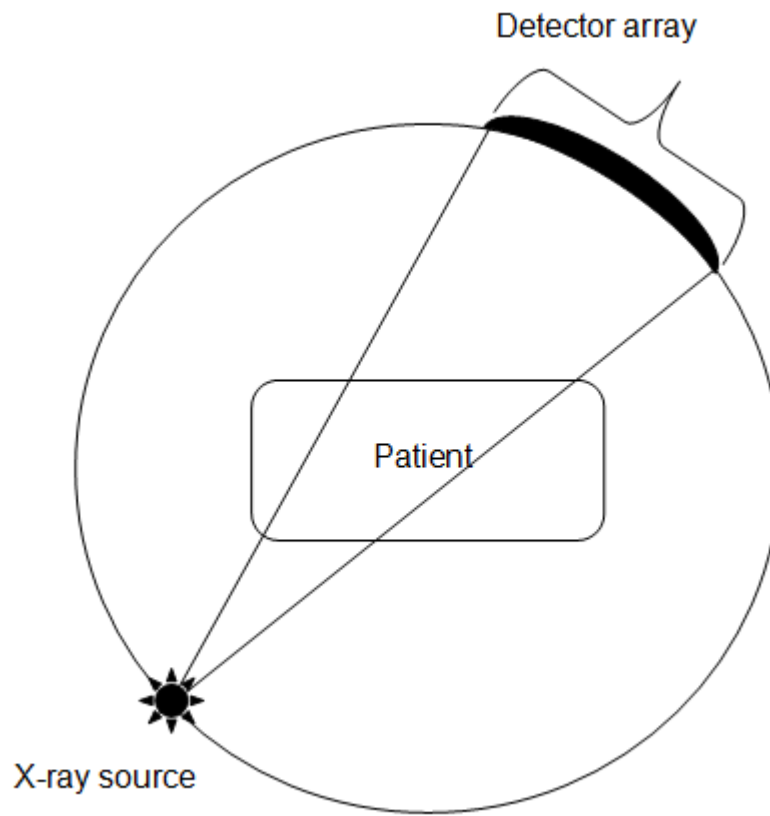
Figure 1.3: An illustration of a typical fan beam CT geometry.

1.3. Treatment Planning

In treatment planning, the patient model acquired during treatment simulation is input into software which has also been programmed with a computerized model of the intended treatment machine. The planning software can use the virtual patient and treatment machine to calculate the expected dose distribution in the patient given a set of parameters defining the treatment beams. Previously, the person developing the treatment plan would manipulate the beam parameters through a process of educated trial and error

until an acceptable dose distribution was achieved. More modern treatment planning software now approaches the problem as an optimization procedure. The software incorporates user defined constraints on dose distributions to various organs and the target region, and optimizes the beam parameters to best meet the constraints. Modern treatment techniques such as intensity-modulated radiation therapy (IMRT) allow for the intensity of each beam to be modulated along the beam's cross section, allowing for a much larger set of parameters to be optimized by the planning system, and making highly conformal dose distributions possible.

For treatment planning of organs which may move substantially during treatment, the general approach is to incorporate margins around the target which include the region in which the target is likely to move. The best way to determine appropriate treatment margins is an ongoing area of investigation (van Herk 2004, Maxim *et al* 2007, Burnett *et al* 2008, Colgan *et al* 2008, Coolens *et al* 2008, Mutaf and Brinkmann 2008, Panakis *et al* 2008, Richter *et al* 2008, Sonke *et al* 2008, Wu *et al* 2008b, Yeung *et al* 2009). For treatment of lung tumors, a tumor's range of motion, called the internal target volume (ITV), can be estimated from 4DCT. In addition to the margin defined by the ITV, an additional margin is added to account for possible changes in the tumor's motion, or patient positioning errors. While adding margins is important for ensuring that the target receives the prescribed dose, larger margins mean that more normal tissue is irradiated, and it is a major goal of radiation therapy

to decrease the margins as much as possible while maintaining reliable target coverage. Some advanced treatment delivery techniques, as will be discussed in Section 1.4, allow for substantial reduction of motion margins in lung cancer patients.

For more information related to treatment planning of moving targets, the reader is directed to multiple references (Leong 1987, Lujan *et al* 1999, Bortfeld *et al* 2002, Chetty *et al* 2003, Senan *et al* 2004a, Senan *et al* 2004b, Trofimov *et al* 2005, Unkelbach and Oelfke 2005, Bortfeld and Paganetti 2006, Chan *et al* 2006a, McShan *et al* 2006, Heath *et al* 2009).

1.4. Patient Positioning

Patient positioning for lung tumor patients is a challenging task due to the various kinds of motions and deformations relevant to lung tumors. Before in-room imaging techniques were developed for external beam treatments, patients were often positioned using skin markers made during treatment simulation and lasers mounted in the treatment room. This type of setup can be quite inaccurate since the motion of the internal structures relative to the skin markers is not incorporated (Van Dyk 1999). A superior alternative is to use orthogonal radiographs taken of the patient in treatment position. Such radiographs can be used to align the patient based on clearly visible internal structures, such as bones. This technique, however, is also limited, as it does

not account for the potentially changing relationship between bony anatomy and soft tissue. In the case of lung tumors, it has been shown that the mean position and trajectory of a tumor can change between treatments, so patient positioning based on bony anatomy is not ideal (Seppenwoolde *et al* 2002, Berbeco *et al* 2005a, Berbeco *et al* 2006, Shirato *et al* 2006, Ionascu *et al* 2007, Nishioka *et al* 2008). Recently, soft tissue registration for patient alignment has been made possible by the advent of on-board CBCT.

Like regular CT, CBCT reconstructs a volume where each voxel value represents the linear x-ray attenuation of that point. While regular (or fan-beam) CT uses a line of detectors to acquire one-dimensional (1D) projections and uses these projections to reconstruct a patient's anatomy slice by slice, CBCT uses a flat-panel detector to acquire two-dimensional (2D) projections and uses these to reconstruct a three-dimensional (3D) patient volume directly. On-board CBCT imaging systems are mounted on the same gantry as the treatment linear accelerator, and projection data is acquired by rotating the gantry around the patient. Due to the more limited sampling of data, increase noise from Compton scattering, and more complex reconstruction algorithms, CBCT images are generally of poorer quality than a regular CBCT, but can provide an image of adequate quality for soft-tissue based patient alignment. A comparison of regular fan-beam CT and CBCT images acquired at the University of California, San Diego are shown in Figure 1.4.
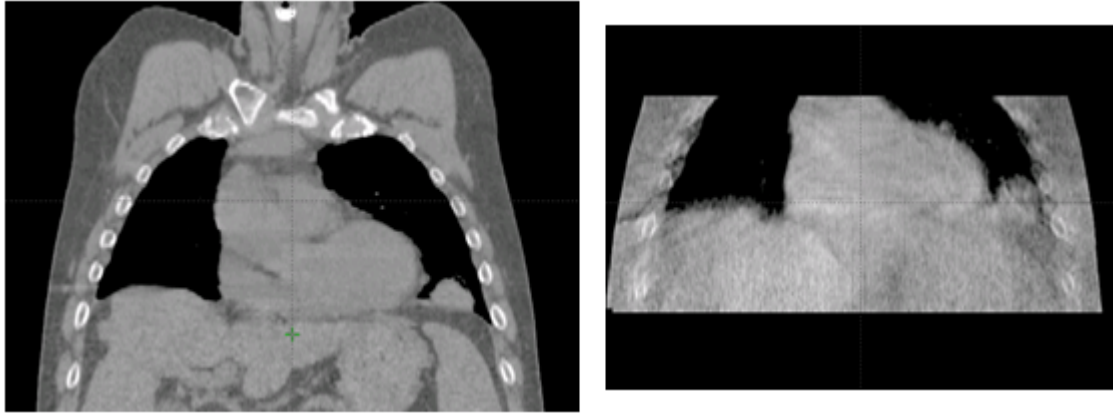
Figure 1.4: A comparison of CT volumes acquired using regular (left) and cone-beam (right) imagine systems. While the CBCT image can be used to determine the position of some soft-tissue structures, it is of noticeably poorer quality than the regular CT. Blurring artifacts are also caused by motion.

In additional the generally poorer image quality of CBCT images, motion artifacts can cause significant blurring of reconstructed images. During a typical CBCT scan, it takes approximately 60 seconds for the gantry to rotate around the patient and acquire a set of projections for CBCT reconstruction. For lung patients, 60 seconds encompasses several respiratory cycles, and the reconstructed CBCT will show organs and the tumor blurred out over the paths they followed during projection acquisition. While the blurred tumor image is more useful for patient positioning than bony anatomy alone, it does not provide clear information about a tumors precise shape or trajectory on the day of treatment, and leaves some ambiguity in determining the tumor position relevant for patient positioning.

Recent research on 4D CBCT has led to the successful reconstruction of respiratory correlated volumes (Sonke *et al* 2005, Li *et al* 2006b, Li *et al*

2007). Similar to 4DCT, these works use either internal or external surrogates to sort raw cone-beam projections into phase bins from which separate CBCT volumes are reconstructed. Motion artifacts are dramatically reduced by this technique, but since several phase-binned volumes are constructed, either substantially more projections must be acquired, or some sort of prior knowledge must be incorporated in order to prevent dramatic view-aliasing artifacts. Currently implemented methods for acquiring more projections include slowing the gantry rotation down to four minutes or more, or using multiple gantry rotations during acquisition. These techniques lead to increased scanning time and potentially increased imaging dose. It is important to minimize the scanning time because longer imaging procedures leave more time for intrafractional changes in patient anatomy, can cause the patient to become uncomfortable, and slow down a clinic's workflow. For many purposes, including lung patient setup, it may often be unnecessary to reconstruct a complete 4D set of volumes. Instead, the 3D trajectory of the tumor alone, combined with a regular CBCT scan, may be sufficient. In Chapter 3 I will present a method for determining a lung tumor's trajectory on the day of treatment using only a conventional 3D CBCT acquisition. In Chapter 4 I will show how the reconstructed tumor trajectory can be combined with a regular CBCT to remove motion artifacts and reconstruct a de-blurred tumor volume on the day of treatment.

1.5. Treatment Delivery

Multiple treatment delivery methods of varying technological complexity and potential treatment quality have been developed for lung tumors. The most straightforward solution is to incorporate margins into the target volume which cover the full estimated range of motion for a tumor so that, as long as the tumor's motion does not vary far from the initial estimation, the tumor will be inside the target region during all phases of the respiratory cycle. As mentioned in Section 1.2, the major drawback of this technique is that the increased target volume means that more radiation dose will be delivered to healthy tissues. In some cases, concern about increased dose to healthy tissues prevents an increased dose from being prescribed to the tumor, and could result in a less effective treatment. In order to reduce the necessary treatment margins, two types of treatment delivery have been developed which incorporate real-time information about a tumor's position. These treatment modalities are called gating and tracking, and will be discussed in the subsequent paragraphs.

Gating based treatments attempt to treat the tumor only during a portion of the respiratory cycle. The treatment beam is only switched on when the tumor is determined to be within a planned-for treatment region (*i.e.,* the gating window), then switched back off when the tumor moves outside of the gating window. Since the tumor is only being treated during a piece of the respiratory cycle, the margins defining the target volume need only encompass

corresponding fraction of the tumor's trajectory. The most critical component of an effective gating treatment is determining when the tumor is within the gating window. A good gating signal depends on real-time localization of tumor position, and is the subject of a great deal of research (Kubo *et al* 2000, Mageras *et al* 2001, Vedam *et al* 2001, Berbeco *et al* 2005a, Cui *et al* 2007b, Cui *et al* 2008, Wu *et al* 2008a, Li *et al* 2009b, Lin *et al* 2009b). An in depth review and discussion of real-time localization algorithms is presented in Section 1.6. While gating treatments offer a potentially very good treatment quality by reducing the treatment volume and allowing for increased dose to the tumor, it also can extend the treatment time significantly, since treatment is only being delivered during a piece of the breathing cycle. Many significant drawbacks are associated with increased treatment times. The patient is more likely to become uncomfortable or move during treatment, and the treatment requires more resources in terms of machine time and personnel from the treatment facility. Additionally, extending the period of time over which a radiation dose is administered can alter the radiobiological effects of the treatment. The trade off between smaller treatment margins and increased time can be expressed in terms of the target volume and the duty cycle (DC), defined as the time spent by the signal within the gate to the total treatment time. As the DC is increased, a larger piece of the respiratory cycle is being treated, and the planning margins must be increased accordingly. Decreasing the DC decreases the target volume but increases the treatment time. The

relationship between DC and target volume can be improved by treating the tumor during a piece of the respiratory phase where it exhibits the least motion, and gating window is usually defined around end of exhale for this reason (Berbeco *et al* 2005a, Cui *et al* 2007b, Jiang *et al* 2008).

Tracking-based treatments can also decrease the target volume, and unlike gating treatment, do not necessarily increase the treatment time. During a tracking treatment, the treatment beam is adapted to follow the target's tracked motion. An effective tracking treatment is difficult to implement, as it should incorporate; 1) real-time tumor localization; 2) a position prediction algorithm to account for system latency; 3) a method for moving the treatment beam to follow the tumor's position; and 4) a method to account for the changing position of the tumor and beam with respect to other changing anatomy. The first requirement, real-time tumor localization, is the most important and challenging task in implementing an effective tracking treatment and will be a primary focus of this dissertation (Keall *et al* 2006). In general, the real-time localization requirements for a tracking treatment are more difficult than for gating, since one is concerned with the exact tumor position at all pieces of the respiratory cycle, instead of only whether or not the tumor is within the gating window. The other three mentioned requirements for implementation of a tracking treatment are significant research topics, and the reader is referred to several references for more information (Murphy *et al* 2000, Schweikard *et al* 2000, Chen *et al* 2001, Keall *et al* 2001, Ozhasoglu

and Murphy 2002, Jiang *et al* 2003, Neicu *et al* 2003, Bortfeld *et al* 2004, Suh *et al* 2004, D'Souza *et al* 2005, Papiez and Rangaraj 2005, Papiez *et al* 2007).

Another recent development in treatment delivery for lung tumors is the popularization of rotational therapy, or volumetric modulated arc therapy (VMAT). Normally external beam radiation is delivered from a set of fixed beam angles, with the treatment beam turned off when the gantry is rotating from one angle to the next. In VMAT, the gantry rotates *during* treatment, and radiation is delivered in one or more arcs around the patient. Since VMAT is a relatively new technology, wide spread systematic studies comparing the quality of treatments delivered by VMAT compared to conventional fixed angle techniques has not yet been published. However, multiple papers have shown anecdotal evidence that VMAT can deliver comparable treatment quality to IMRT in many situations (Bedford 2009, Popescu *et al* 2009, Song *et al* 2009, Wolff *et al* 2009). A major advantage of VMAT treatments is that they can be delivered in a much shorter time than fixed-angle treatments, with treatment times reportedly being reduced by up to a factor of four (Bedford *et al* 2008, Bedford 2009, Popescu *et al* 2009). This has caused VMAT machines to be popular with many treatment centers, and VMAT is rapidly becoming a preferred treatment modality. If VMAT is to be used for lung cancer patients, it would not be practical to use a gating treatment, because it would require repeatedly stopping the gantry rotation during delivery. Therefore, tracking treatments would be the more suitable method for reduction of target volume.

A major purpose of this dissertation is to develop an algorithm for real-time localization of lung tumors during VMAT by tracking the tumor in rotational cone-beam projections which could be acquired during treatment.

1.5. Real-time Localization

An accurate and reliable method for determining the target position in real-time is of the utmost importance for gating or tracking lung tumor treatments. Poor tracking results could lead to dramatically reduced treatment quality. Lung tumor tracking techniques can generally be categorized as either direct tumor tracking, tracking via breathing surrogates, or tracking of implanted markers. Tracking based on fiducial implants has been shown to be highly accurate (Seiler *et al* 2000, Sharp *et al* 2004, Balter *et al* 2005, Tang *et al* 2007). For this type of tracking, a small radio-opaque marker is implanted into the tumor then tracked in x-ray projections during treatment. Two significant drawbacks of implanted marker tracking are risks of clinical complications such as pneumothorax (Arslan *et al* 2002, Geraghty *et al* 2003) and the possibility of marker migration (Nelson *et al* 2007). When possible, it is preferable to determine tumor locations without the additional risks caused by implantation of fiducial markers. Breathing surrogate-based tracking is appealing because well chosen surrogates can be easily tracked, sometimes with no additional radiation dose to the patient (*e.g.,* optical tracking), and do

not require an additional implantation procedure. While studies have shown that certain surrogates often have a strong correlation with tumor motion, it has also been shown that the relationship can often vary both during and between treatments (Hoisak *et al* 2004, Berbeco *et al* 2005b, Wu *et al* 2008a, Cervino *et al* 2009). The problems associated with marker and surrogate-based tracking could be avoided with a markerless tracking system, where the tumor is tracked directly based on its image in x-ray projections. While direct markerless tracking is appealing because it does not rely on the relationship of the tumor's motion with a surrogate, and does not require any additional implantation procedures, the tumor is often much more difficult to track than high contrast fiducial markers or breathing surrogates. Tumors often lack sufficient contrast or a clear border, and can be difficult to distinguish from other nearby anatomy in projection images.

Several papers have been published on methods for markerless tracking of lung tumors in fluoroscopic images, with highly accurate tracking results achieved in some patients when the tumor is imaged from the anterior-posterior (AP) direction (Cui *et al* 2007a, Xu *et al* 2008, Lin *et al* 2009a). A significant drawback of these techniques is the requirement for fluoroscopic data to be acquired prior to treatment, and the need for a clinician to define tumor positions in the images for model training purposes. In addition, a fluoroscopic training sequence must be developed for each beam angle at which the tumor will be tracked. The increase in time associated with these

tasks, and the fact that tumors are often difficult to visualize in fluoroscopic data, means that reliance on fluoroscopic training data may not be clinically practical. Furthermore, since training data must be developed for each treatment angle, these techniques are not applicable to the 3D geometry of rotational cone-beam projections. This paper presents an algorithm that avoids these issues through the use of digitally reconstructed radiographs (DRRs) generated from 4DCT acquired prior to treatment. Many previous works have also shown that DRRs can be used for localization of bony anatomy such as the spine in 2D projection images, with or without the aide of additional fiducial markers, and have shown that these localization results can be applied to the 2D/3D registration problem of patient position monitoring based on orthogonal x-ray projections (Lemieux *et al* 1994, Penney *et al* 1998, Penney *et al* 2001, Rohlfing *et al* 2005). Recently the feasibility of using DRR templates derived from 4DCT for markerless fluoroscopic gating treatments of lung tumors has been studied (Moser *et al* 2008, Li *et al* 2009b).

1.6. Objectives and Organization

The goals of this dissertation are to develop a real-time localization algorithm that is applicable to rotational cone-beam projections, and to use tracking results from a set of projections acquired during a regular 3D CBCT scan to reconstruct a tumor's trajectory, size, and shape on the day of

treatment. In Chapter 2 the foundation of the rotational tracking algorithm and some direct tracking results will be presented. In Chapter 3 a method for using tracking results from a regular 3D CBCT scan to reconstruct a patient's 3D tumor trajectory on the day of treatment will be presented. In Chapter 4 the reconstructed 3D trajectory obtained in Chapter 3, combined with a reconstructed 3D CBCT volume will be used in order to reconstruct an image of the tumor on the day of treatment from which motion blurring has been removed. In Chapter 5 a potentially more robust combined tracking algorithm is presented which combines diaphragm-based and direct tumor tracking in an attempt to exploit the benefits of each technique while minimizing the corresponding weaknesses.

2. Direct Tracking in Rotational Cone-Beam Projections

2.1. Overview

Real-time localization of lung tumors can significantly improve treatment quality for lung cancer patients. While accurate tracking results are possible when a fiducial marker is surgically implanted into a tumor, the associated risks of pneumothorax or other complications make this procedure undesirable for lung tumors (Arslan *et al* 2002, Geraghty *et al* 2003). Previous work has shown success in direct lung tumor tracking in fluoroscopic x-ray series acquired from a fixed angle in the AP direction (Cui *et al* 2007a, Xu *et al* 2008, Lin *et al* 2009a). Recently, VMAT has gained increasing popularly in external beam radiation therapy. Unfortunately, none of the previous techniques used for markerless tracking in fluoroscopic images are applicable to the rotational geometry associated with VMAT. In this chapter, algorithms for direct tumor tracking in rotational cone-beam projections will be developed. The feasibility of the algorithm will be demonstrated on a digital phantom, a physical

phantom, and patients. Tracking results were obtained by comparing reference templates generated from 4DCT to rotational cone-beam projections. Direct tumor tracking in rotational projections could be clinically useful for rotational therapies, and has other potential uses discussed in later chapters.

2.2. Methods

2.2.1. Markerless tracking algorithm for rotational geometry

Previous algorithms for markerless tracking of lung tumors in x-ray projections rely on fluoroscopic training data acquired prior to tracking for training purposes. This training data is acquired from the same angle at which the tumor will be tracked, and must cover several different tumor locations as viewed from the projection angle. When a treatment is delivered from multiple fixed angles, a new set of training images must be acquired for each new view of the tumor, and a physician must define the tumor position in the training images. For VMAT, the tumor is treated from many angles in continuous succession as the gantry rotates around the patient. In order to track the tumor using an x-ray imaging device mounted on the gantry, the tumor must be tracked in images acquired as the gantry is rotating around the patient. It would be extremely impractical to attempt to acquire a set of fluoroscopic

training data for each view around the patient, so another method must be developed for tracking in rotational cone-beam projections.

In this chapter a direct tracking algorithm based on multiple reference templates is developed which avoids the need for fluoroscopic training data by generating templates from data already acquired during standard treatment simulation procedures. The templates are used to determine the tumor positions in rotational cone-beam projections by comparing each template, representing different tumor positions and poses, to each projection in which the tumor is to be tracked.

2.2.2. Generating reference templates

The need for fluoroscopic training data is eliminated by generating simulated x-ray projections, known as DRRs, from a set of 4DCT volumes acquired during treatment simulation. Since a 4DCT can represent tumor positions corresponding to each piece of the breathing cycle, DRRs generated from 4DCT can also represent multiple tumor positions and poses.

DRRs are generated using the fact that each voxel of a 4DCT represents the linear x-ray attenuation of that voxel. The Beer-Lambert law states that

$$I = I_0 e^{-\int \mu(\mathbf{x},\mathrm{E})\, dl},$$

(2.1)

where I_0 is the incident photon intensity, I is the photon intensity after attenuation, $\mu(\mathbf{x}, E)$ is the linear attenuation coefficient of the material at position $\mathbf{x}$ and with photon energy E, and l is the path the photon beam follows through the attenuating material (in this case, the patient). The linear attenuation coefficient is dependent on energy because the energy of the photon beam determines the probability of various types of interactions of photon beams with matter, including coherent scattering, the photoelectric effect, Compton interactions, and pair production. The value of each voxel in a CT volume is properly given in Hounsfeld Units (HU) defined as

$$HU = \frac{\mu - \mu_{H2O}}{\mu_{H2O}} * 1000 \tag{2.2}$$

where μ_{H2O} is the linear attenuation of water for a given energy. Therefore, using knowledge of the x-ray source used during imaging, a CT volume can be converted back into an attenuation matrix. Since x-ray sources are rarely monoenergetic, an equivalent energy is approximated for a given energy spectrum when calculating linear attenuation coefficients. Once a CT volume has been converted to attenuation coefficients, simulated x-ray projections can be computed by calculating the line integral of this attenuation matrix along a ray connecting the simulated x-ray source to each pixel in the simulated

imager. Many variations of algorithms have been proposed for DRR generation including discrete or interpolated ray casting, voxel projection, shear-warp factorization, and others (Siddon 1985, Lacroute and Levoy 1994, Jacobs *et al* 1998, Freund *et al* 2004, Birkfellner *et al* 2005). For the purposes of this work, a version of Siddon's ray tracing algorithm for DRR generation using the C programming language was implemented.

Reference templates were created by generating DRRs from 4DCT volumes with projection geometry corresponding to the cone-beam projections in which the lung tumor was tracked. As shown in Figure 2.1, the tumor was first contoured in each phase of 4DCT. These contours were used to define the tumor's centroid position in each template. Using the geometry shown in Figure 2.2, for projection angle θ, the position of a point defined in 3D Cartesian coordinates (x, y, z) projected onto the detector's coordinate system (i, j) is given by

$$j = \frac{(R+r)(x\sin(\theta) - y\sin(\theta))}{x\cos(\theta) + y\sin(\theta) + r}, \quad (2.3)$$

$$i = z\frac{R+r}{x\cos(\theta) + y\sin(\theta) + r}, \quad (2.4)$$

where R is the source-to-detector distance, and r is distance between the rotational isocenter and the detector. The origin of the Cartesian coordinate

system is the rotational isocenter, while the origin of the detector's coordinate system is the projected position of the isocenter in the detector. In addition to tumor contours, a cylindrical volume of interest (VOI) encompassing the complete range of tumor motion derived from 4DCT was defined. The cylindrical VOI was made as small as possible while still containing the full tumor trajectory. It is also possible to define other VOI in order to track other surrogates, such as the diaphragm or abdomen surface, and the potential benefit of using other surrogates will be investigated in Chapter 5. For the study in this chapter, only the tumor was tracked.
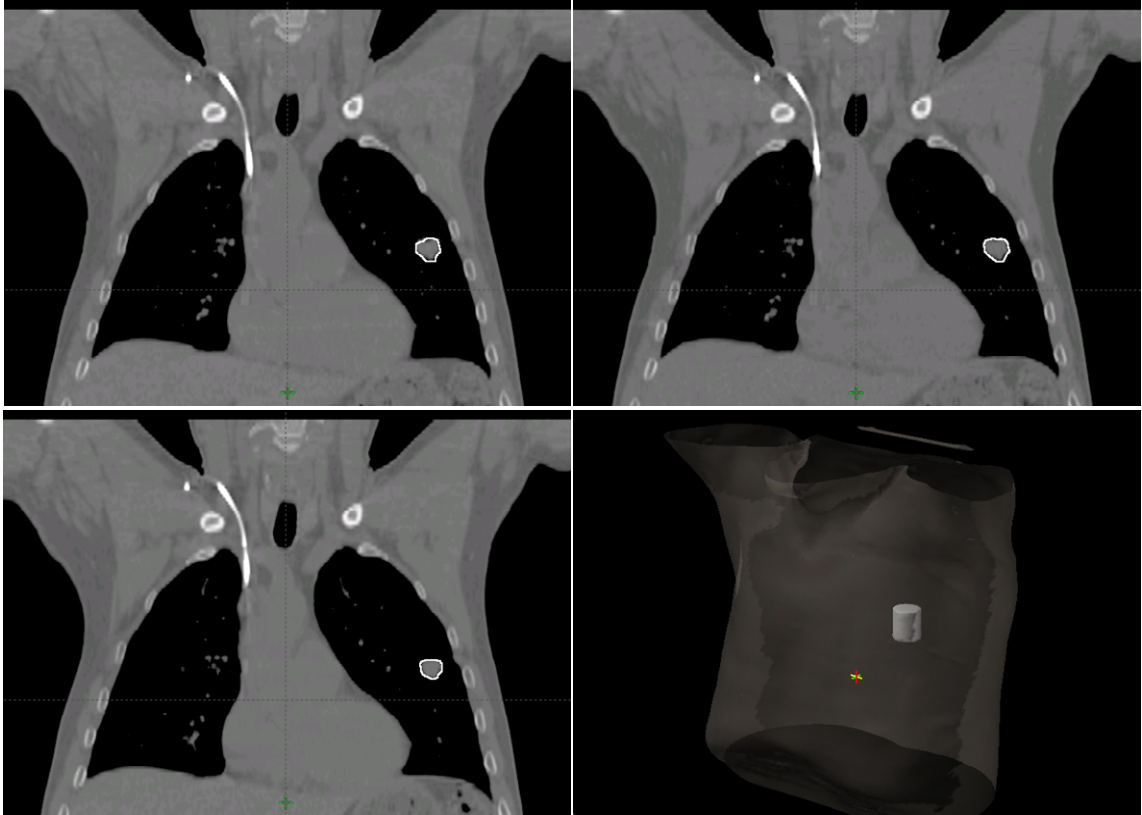
Figure 2.1: Coronal slices from three breathing phases of a patient's 4DCT. The tumor is contoured on each phase to define its position in the corresponding templates. The lower right quadrant shows the cylindrical volume of interest (VOI) encompassing the tumor's full motion range derived from all phases.
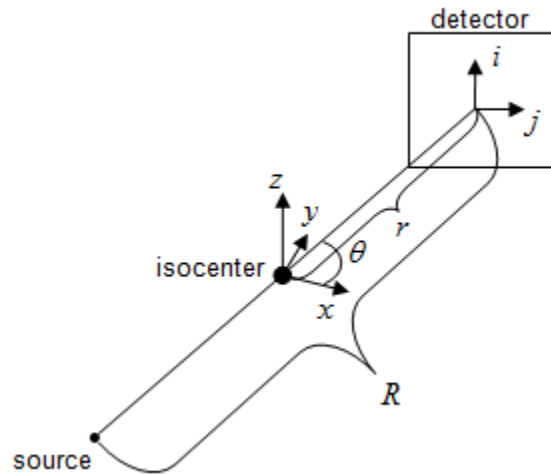
Figure 2.2: A diagram showing the geometry of a cone-beam scan with a flat panel detector.

Next, the 4DCT was rigidly registered to a CBCT based on bony anatomy. Interpolation was used to match the resolution of the 4DCT to the CBCT, and then thresholds were applied to both 4DCT and CBCT to remove soft tissue. The resultant bony images were registered using a multiple-resolution search to maximize the similarity between the two images. Image similarity was measured using normalized mutual information, as defined in the following section. DRRs were then created from every phase of 4DCT at angles corresponding to the rotational cone-beam projections in which the tumor was tracked. The previously defined VOI was also projected with the same geometry, and used as a binary mask to define regions of interest (ROI) on each DRR. These masked DRRs form the templates upon which the tracking algorithm was based, and the number of templates for each angle equals the number of 4DCT phases used. For each cone-beam projection in

which the tumor was tracked, the VOI was projected as a mask to define an

ROI matching that of the DRRs (Figure 2.3).
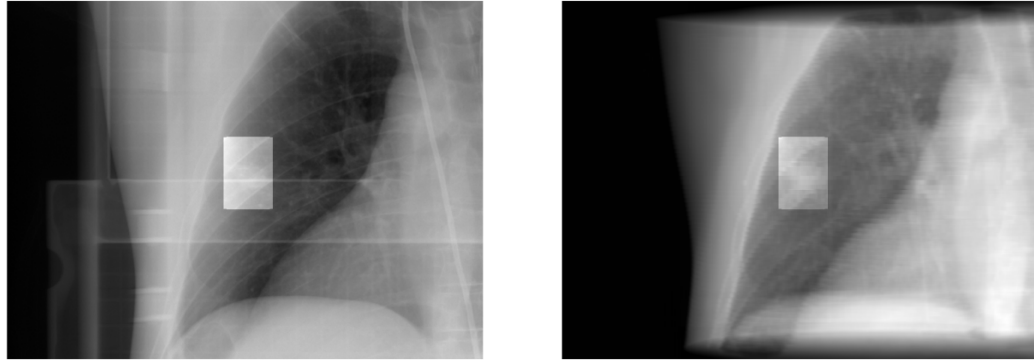
Figure 2.3: A cone-beam projection (left) and generated DRR (right) for one patient. The ROI is the brighter, highlighted region.

2.2.3. Calculating template similarity

There are multiple possible image similarity measures that could be used to compute the similarity between each DRR reference template and a cone-beam projection. One of the most simple metrics is the sum of squared difference (SSD), defined as

$$SSD = \frac{1}{N}\sum_{i}\left|A(i) - B(i)\right|^2 , \qquad (2.5)$$

where N is the number of pixels, i indexes the pixels of the image, and A and B are the images being compared. This measure has been shown to be the

best similarity measure when two images differ only be Gaussian noise (Hajnal *et al* 2001). A less restrictive condition on the images would be that there is a linear relationship between the pixel values in each image, in addition to some Gaussian noise. Under these conditions normalized cross correlation (NCC) is the preferable similarity measure, given by

$$NCC = \frac{\sum_i (A(i) - \overline{A}) * (B(i) - \overline{B})}{\sqrt{\sum_i (A(i) - \overline{A})^2 * \sum_i (B(i) - \overline{B})^2}} \, , \qquad (2.6)$$

where $\overline{A}$ and $\overline{B}$ represent the corresponding average pixel values for each image. If a CT volume could be reconstructed perfectly, and the algorithm used to generated DRRs perfectly modeled the physical process of x-ray attenuation and image generation for the imaging system being modeled, one of the above image similarity measures would be ideal for the purposes of this work. Unfortunately, real CT volumes often contain imaging artifacts, and DRR generating algorithms are not completely realistic in terms of modeling the energy spectra and scatter of x-ray imaging tubes. The probability of various interactions with matter (Compton, photoelectric, *etc.*,) depends on the energy of incident radiation. The material properties that determine the attenuation of radiation are different for each of these types of interactions (Z^3, electron density, *etc.*,). Therefore, the attenuation determined at one energy level may not be appropriate for another energy level. While the x-ray energy spectra

used for CT acquisition and reconstruction during simulation is usually similar to the x-ray energy spectra generated by on-board CBCT imaging devices, there is often some difference, meaning that the attenuation values represented in a CT volume may not be completely appropriate for the reconstruction of DRRs designed to match cone-beam projections acquired by the on-board imager. For these reasons, the relationship between intensity values in DRRs and in real cone-beam projections can sometimes be nonlinear, and a more robust image similarity measure is preferable.

Derived from the field of information theory, mutual information (MI) provides a more robust similarity measure that does not rely on a linear relationship between pixel values in each image, and has shown great success in registering images of different modalities (*e.g.,* MRI to CT registration) (Thurfjell *et al* 2000, McLaughlin *et al* 2004, Yokoi *et al* 2004, Yang *et al* 2008). Mutual information attempts to measure the amount of shared information in two images. It defined as

$$ MI(X;Y) = \sum_x \sum_y p(x,y) \log \left(\frac{p(x,y)}{p(x)p(y)} \right) , \qquad (2.7) $$

where X and Y are two random variables, $p(x,y)$ is the join probability distribution of X and Y, $p(X)$ is the marginal probability distribution of X, and $p(Y)$ is the marginal probability distribution of Y. In practice, the

probability distributions are estimated from histograms of image intensities. Some care must be taken in this step, as the choice of bin size and range can affect the shape of the histogram, and correspondingly the similarity score.

In this study, both DRR and cone-beam projections were normalized to a pixel value range of 0-255, then a normalized variant of mutual information was calculated between each masked projection and each DRR with corresponding angle (*e.g.,* a 10-phase 4DCT would lead to 10 DRRs to compare to each projection). Normalized mutual information (NMI) was defined as

$$NMI(X;Y) = \frac{MI(X;Y)}{H(X,Y)}, \tag{2.8}$$

where $H(X,Y)$ is the joint entropy between images X and Y. Histograms used to estimate distributions were defined on the integer set from 0-255. The program used to calculate NMI was developed based on a previously written software package (Peng *et al* 2005). Some additional concerns and potential problems with using NMI as a similarity measure are discussed in Section 2.5.

2.2.4. Determining tumor position from templates

For each projection, the two highest scoring templates from the set of DRRs with matching angle were selected and allowed to shift within a 21 by

21 pixel grid centered on the template (with pixel size 0.388 mm) until the highest *NMI* score was achieved. The optimal number of templates for every situation is hard to determine, but two is a reasonable choice. In some cases, template selection may choose a bad template, or one that is not close to the tumor's true position. In this case, having two templates allows for the effects of one badly selected template to be mitigated by the second (hopefully better) template. This shift was incorporated to allow for the fact the tumor's position may not be exactly represented by one of the 10 corresponding reference DRR templates. While the true motion of the lung is non rigid, the rigid template shifting is considered an acceptable approximation within a small search region. Positions derived from each of the two highest scoring templates were averaged together using Gaussian weights based on the magnitude of the template shift to produce a final tumor position. This weighting scheme was chosen based on the assumption that as templates are shifted from their initial position, they will generally become less reliable due to deformation or changes in the surrounding anatomy.

As described thus far, the algorithm locates the tumor in each 2D projection. Most lung tumor motion is along the SI axis of a patient, and since this axis is aligned with the axis of rotation for the cone-beam projections, the most important SI information is captured within each projection image. While this information is helpful for a tracking treatment, ideally one would prefer to know the true 3D position of the tumor as each projection is acquired. Using

these 2D positions to calculate the tumor's corresponding 3D position for each projection is an underdetermined problem, and cannot be done without using some method of approximation or incorporating some prior knowledge into a 3D model of tumor motion. In the next chapter we will outline a method for combining a set of projections to calculate a representative 3D tumor trajectory. For the purpose of analyzing the accuracy of the tracking algorithm itself, we will compare the algorithm output to the defined true tumor position in each projection image. Positions in the imager plane, with corresponding errors, are scaled back to the average tumor position derived from 4DCT (or in the phantom case, to the known tumor position). When the tumor is close to the isocenter, this is approximately equal to scaling by the source-axis distance divided by the source-to-imager distance. While this method of approximating the tracking error at the tumor's location is not exact since the tumor's exact 3D position is unknown, the approximation is quite accurate since the variability in the tumor's position is very small compared to the tumor-to-imager distance.

2.3. Materials

2.3.1. Digital NCAT phantom data

Initially, the algorithms were tested using a non-uniform rational B-spline (NURBS) based cardiac-torso (NCAT) phantom (Segars *et al* 1999,

Segars 2001, Segars *et al* 2001). This digital phantom is based on data from the Visible Human Project, while the respiratory motion model was developed based on basic knowledge of respiratory mechanics combined with a high resolution gated-CT data set. The phantom is very flexible, while also maintaining a high level of anatomical realism (a beating heart, detailed bronchial trees, etc.). DRRs generated from the phantom are shown in Figure 2.4.

DRRs were created at 1 degree intervals for a full 360 degree rotation, with the end of exhale tumor position centered at the rotational isocenter.

For simulating real cone-beam projections, a much higher resolution phantom was desired in order to simulate the continuous spatial and temporal information of a real patient. However, choosing too high of a resolution resulted in prohibitive computational times, so a phantom with 1mm x 1mm pixel size and 0.5 mm slice thickness was used, and 100 phase bins were created. DRRs were created from these high resolution phantoms, and treated as the simulated cone-beam projections. These simulated projections were put together based on patient breathing period and gantry rotation speed in order to create a complete breathing pattern for the full 360 degree rotation.
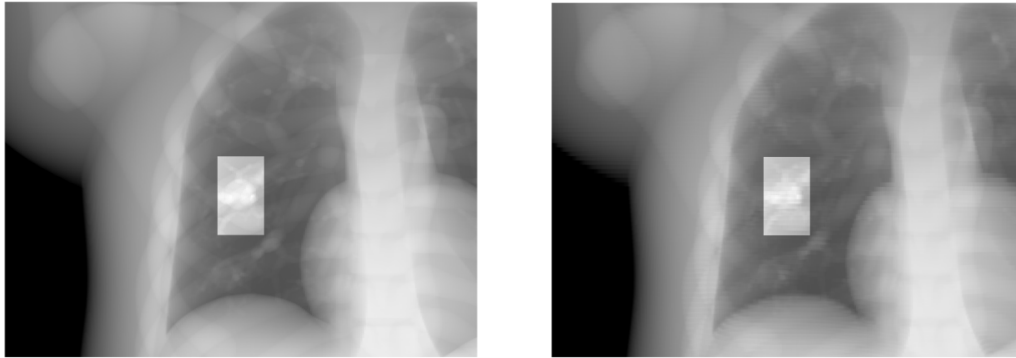
Figure 2.4: Simulated projection (left) and DRR template (right) created from NCAT phantom. The simulated projection has higher resolution. The ROI around the tumor is highlighted.

2.3.2. Physical phantom data

The algorithms were also tested on a simple physical respiratory phantom. The phantom consisted of a cork block resting on a platform that could be programmed to undergo translational motion in one dimension. This platform was used to simulate the SI respiratory motion of a lung tumor. Inside the cork block were embedded several tissue-like objects including an approximately 2.5 cm water balloon which was used as the tracking target. An additional, smaller platform could be programmed to move perpendicularly to the primary platform, simulating the AP motion of the abdomen during respiration. A picture of the phantom is shown in Figure 2.5.

4DCT was acquired using a GE four-slice LightSpeed CT scanner (GE Medical Systems, Milwaukee, WI, USA) and a Varian Real-time Position Management (RPM) system (Varian Medical Systems, Palo Alto, CA, USA). The RPM block was placed on the platform exhibiting AP motion. Cone-beam

projections were acquired using Varian On-Board Imager 1.4 in full-fan mode with 100 kVp, 80 mA, and 25 ms exposure time.

Figure 2.5: A picture of the physical phantom used (left). The sagittal CT slice on the right shows the objects embedded in the cork block.

2.3.2. Patient data

Lastly, three patient data sets were used to evaluate the algorithms. Data was acquired using the same systems as described for the physical phantom. Breathing signals were obtained using an RPM block placed on the patient's abdomen. CBCT scans were conducted in half-fan mode. Half-fan mode allows for larger volumes to be reconstructed by shifting the imager off-center laterally. Since the isocenter was not placed on the tumor, the tumor is not visible in some projections. The projections were taken with the imaging

system set to 110 kVp, 20 mA, and 20 ms exposure time. The 4DCT used to generate reference templates was acquired during simulation, approximately two weeks prior to the cone-beam scan. Figure 2.6 shows generated DRRs with centroid positions and projected contours derived from 4DCT for patient 2. The border of the tumor is difficult to discern in these magnified DRRs, and is particularly hard to see since the tumor edge is partially covered by the projected contours. The tumor is somewhat easier to see, for example, in Figure 2.3.

A ground truth to measure the tracking algorithm against was defined by asking a clinician to contour the tumor location in each cone-beam projection using a simple graphical user interface programmed in MATLAB 7.7. The patients chosen for this study had tumors that were visible to the clinician in cone-beam projections. From the contour the tumor centroid was calculated for each projection. Since the tumor is sometimes hard to see in these projections, the uncertainty in this definition of ground truth can be large, and may depend on the angle at which a projection is taken. A future study is planned to quantify this error more carefully, but a rough estimation based on comparing contours drawn from two observers suggests that the error in centroid position is patient 1 is on the order of about 2-3 mm, with larger errors occurring at angles where the view of the tumor is obstructed by other high contrast objects, such as the spine.
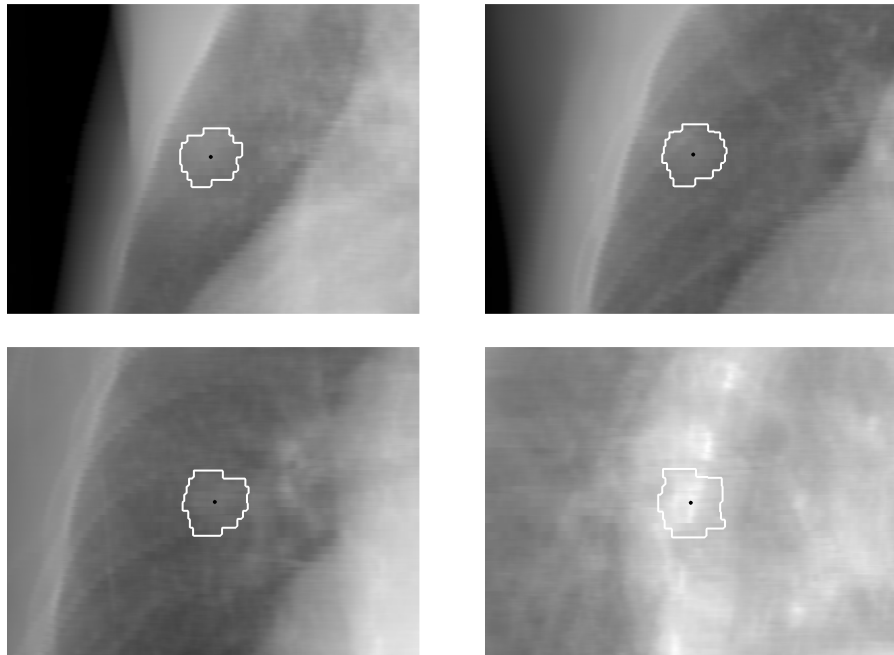
Figure 2.6: Four DRR templates generated with 30 degree spacing for patient 2, with tumor contours shown in white and centroid positions shown as black dots. The poorer resolution in the SI direction is due to the 2.5 mm CT slice thickness. When the tumor is behind the spine (lower right), its shape is very difficult to see.

2.4. Results

2.4.1. Digital NCAT phantom results

Tracking results for the NCAT phantom are shown in Figure 2.7 for both the axial (along the axis of rotation, or the SI direction) and the tangential (perpendicular to the axis of rotation) imager directions. The tangential direction represents a mixture of AP and left-right (LR) directions depending on the projection angle. All results have been scaled back to the known tumor position, as explained at the end of Section 2.1. The phantom was

programmed with 4 second period, 2.3 cm SI tumor amplitude, 0.9 cm AP amplitude, and 0.2 cm LR amplitude. Images were simulated at 1 degree intervals over a 360 degree arc, with a gantry rotation time of 61.2 s. The 1.8 cm diameter tumor was positioned in the middle of the right lung, as shown in Figure 2.4. For this situation, the root mean square error (e_{rms}) in the axial dimension was 0.6 mm, and the 95th percentile absolute error (e_{95}) is 1.1 mm. For the tangential direction, the corresponding e_{rms} was 0.4 mm and the e_{95} was 0.8 mm.
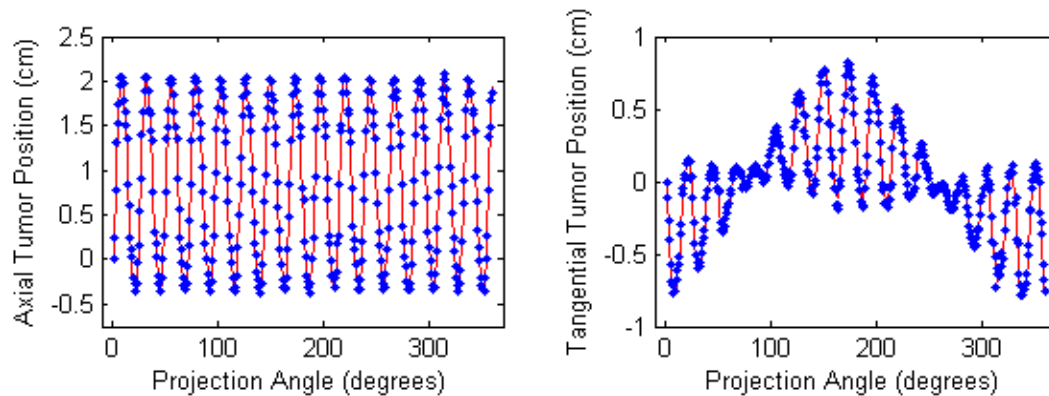
Figure 2.7: Tracking results for the NCAT phantom. Blue dots show the tracking output, and a red line shows the true tumor position. Results for the axial (left) and tangential (right) dimensions of the imager are shown. The axial e_{rms} is 0.6 mm, and the e_{95} is 1.1 mm. The tangential e_{rms} is 0.4 mm and the e_{95} is 0.8 mm.

2.4.2. Physical phantom results

Tracking results for the physical phantom are shown in Figure 2.8. The phantom was programmed to move sinusoidally in the SI direction with 4 second period and 1.5 cm amplitude. 359 projections were acquired over an

arc of 200 degrees with a frequency of 10.7 Hz. The tangential and axial imager directions are defined as described in Section 2.4.1, and the tracking results are scaled to the true tumor position. For the axial direction the e_{rms} is 0.8 mm, and the e_{95} is 1.7 mm. In the tangential direction the e_{rms} is 0.7 mm and the e_{95} is 1.7 mm.
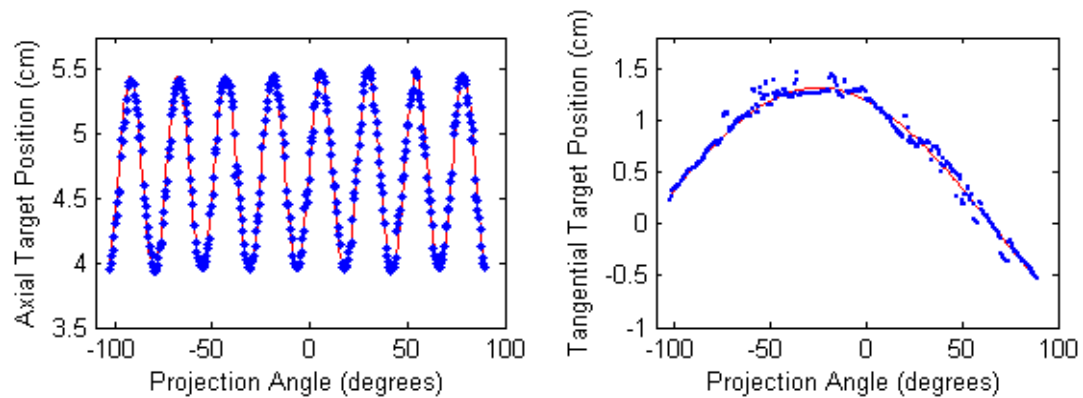
Figure 2.8: Tumor tracking results for the physical phantom. Ground truth is represented by a solid red line while tracking results are represented by blue dots. For the axial direction the e_{rms} is 0.8 mm, and the e_{95} is 1.7 mm. In the tangential direction the e_{rms} is 0.7 mm and the e_{95} is 1.7 mm.

2.4.3. Patient results

Results for patients 1, 2 and 3 are shown in Figure 2.9, Figure 2.10, and Figure 2.11 respectively. Approximately 650 projections were obtained for each patient over an arc of 360 degrees with a frequency of 10.7 Hz. However, since the scans were performed in half-fan mode (with the imager shifted laterally), and the tumor was not located at the isocenter of the cone-beam scan, the tumor is only visible in a subset of these projections. For each

patient, the tumor was tracked in the largest continuous set of projections in which the tumor was visible. For patient 1, this was 281 projections. For patient 2, 373 projections were used. For patient 3 235 projections were used.

In patient 1 the tracked tumor was located in the left lower lobe, just above the patient's diaphragm in the periphery of the lung. From 4DCT the tumor was estimated to have 1.8 cm diameter, and motion with 4.4 second period, 1.4 cm SI amplitude, 0.2 cm AP amplitude, and 0.9 cm LR amplitude. For the axial direction the e_{rms} is 1.7 mm, and the e_{95} is 3.2 mm. In the tangential direction the e_{rms} is 1.8 mm and the e_{95} is 3.3 mm.

In patient 2 the tracked tumor was located near the center of the left lung. From 4DCT the tumor diameter was estimated as 1.2 cm, with a 2.7 second breathing period and 0.5 cm, 0.3 cm, 0.4 cm amplitudes in the SI, AP, and LR directions respectively. For the axial direction the e_{rms} is 1.0 mm, and e_{95} is 1.9 mm. In the tangential direction the e_{rms} is 1.1 mm and the e_{95} is 1.6 mm.

In patient 3 the tumor was located near the spine in the lower right lung. From 4DCT the tumor diameter was estimated as 1.6 cm, with a 3.0 second breathing period and 1.9 cm, 0.1 cm, and 0.1 cm amplitudes in the SI, AP, and LR directions respectively. For the axial direction the e_{rms} is 2.5 mm, and e_{95} is 4.6 mm. In the tangential direction the e_{rms} is 1.1 mm and the e_{95} is 1.6 mm.
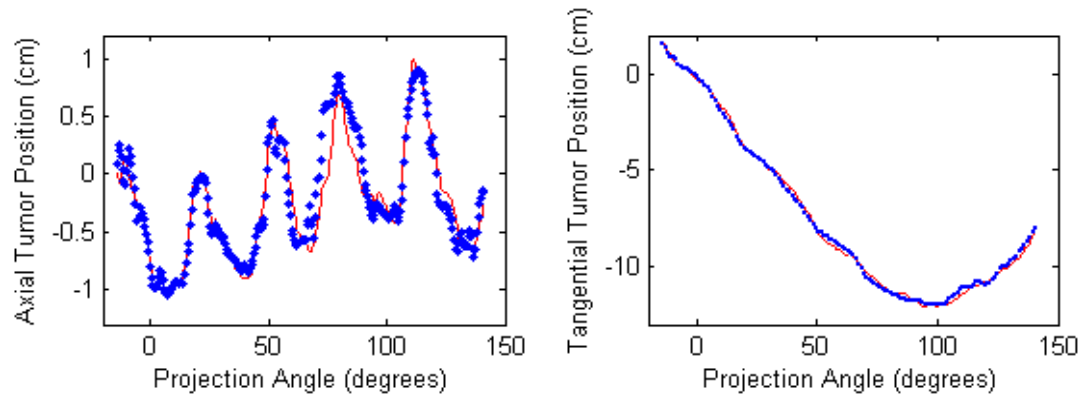
Figure 2.9: Tumor tracking results for patient 1. Ground truth is represented by a solid red line while tracking results are represented by blue dots. For the axial direction the e_{rms} is 1.7 mm, and e_{95} is 3.2 mm. In the tangential direction the e_{rms} is 1.8 mm and the e_{95} is 3.3 mm.
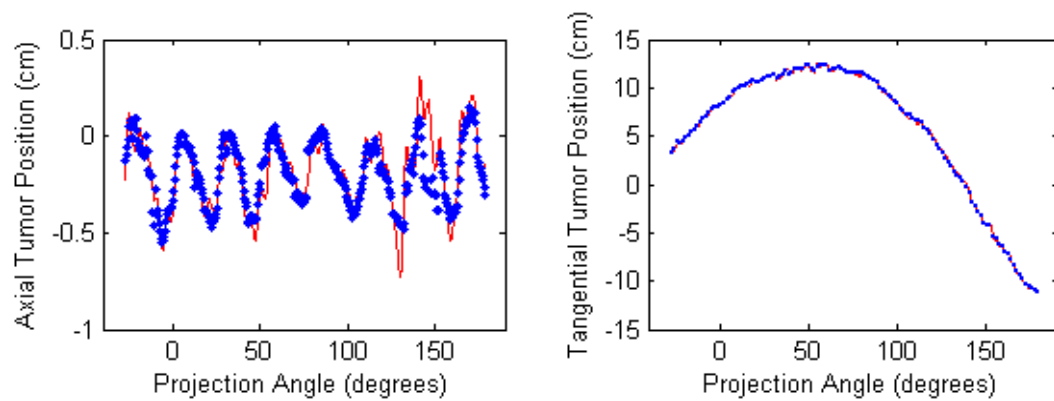
Figure 2.10: Tumor tracking results for patient 2. Blue dots represent the tracking output, and the tumor position is represented by a solid red line. For the axial direction the e_{rms} is 1.0 mm, and e_{95} is 1.9 mm. In the tangential direction the e_{rms} is 1.1 mm and the e_{95} is 1.6 mm.
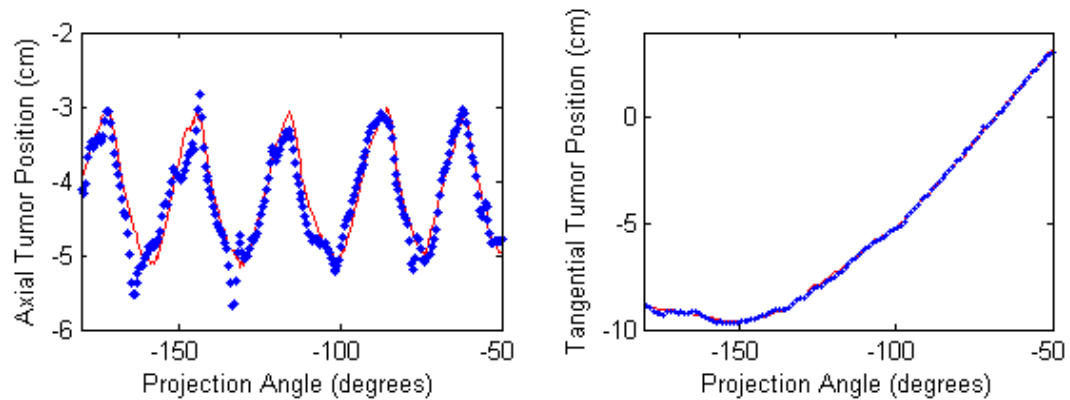
Figure 2.11: Tumor tracking results for patient 3. Blue dots represent the tracking output, and the tumor position is represented by a solid red line. For the axial direction the e_{rms} is 2.5 mm, and e_{95} is 4.6 mm. In the tangential direction the e_{rms} is 1.0 mm and the e_{95} is 1.7 mm.

2.5. Discussion

The proposed method for direct tumor tracking in rotational projections performed very well for phantom cases (better for the digital phantom), with sub-millimeter accuracy in both the axial and tangential imager dimensions. In patient studies, the algorithm performed well for most angles, but exhibited large errors for some projections.

One source of error in the tracking algorithm is the difficulty in localizing the tumor when other high contrast objects obscure its image (Figure 2.12). . For example, in patient 2 near the seventh breathing peak shown in Figure 2.12, the projections were acquired at an angle such that the spine was located in line with the tumor and the source, and the tracking results become quite poor. Patient 3 had the largest error, and also had the largest number of

projections where the tumor overlapped with the spine due to the tumor's location in the body. In patient 1, tracking results appear worst around the fourth peak, and were discovered to correspond to the projections at which the edge of the treatment couch was passing in front of the tumor in the projection images. It is clear that the couch could pose a problem, since it is not represented in the 4DCT. This issue could possibly be managed by pre-scanning and subtracting the couch from projection data, or by using inpainting methods to remove the couch (Chan *et al* 2006b, Cai *et al* 2008). The cause of the poor tracking near the spine is less obvious. Though the spine is present in both 4DCT and CBCT, it is possible that some deformation or registration error may occur between the two. Since the spine is a high contrast object, the template matching and local rigid registration may be dominated by the spine position, and the determination of the tumor position may become less accurate. It is also possible that the large errors are due more to the uncertainty in the clinician-defined ground truth than in the tracking algorithm. One potential solution is to separate the tumor image from the other obstructions using some variant of small angle digital tomosynthesis (DTS). However, given normal gantry rotation speeds and breathing periods, it is unlikely that images could be acquired from widely enough spaced angles to generate useful DTS images without too much blur being caused by respiratory motion. Another potential solution is to use surrogate based tracking when the tumor is unable to be tracked directly. This solution lends

itself particularly well to the algorithm of this chapter, since other surrogates can be tracked simply by defining VOI around other anatomical locations, such as the diaphragm or chest wall. This solution is explored further in Chapter 5, where a method for combining direct tumor tracking diaphragm-based tracking is presented.

Other significant sources of error may include artifacts in 4DCT, interfractional or intrafractional changes in anatomy or respiratory motion as compared with 4DCT, or deficiencies in the physics model used to generate DRRs. Each of these may result in reference templates which are not ideally suited to tracking the tumor motion on the day of treatment.

Phase-binning artifacts frequently occur in 4DCT of patients with irregular breathing patterns (Rietzel *et al* 2005). Even for regular breathing patterns, motion-induced artifacts will occur, which may partially explain why the physical phantom tracking results had larger errors than the digital phantom. These 4DCT artifacts will lead to the generation of DRR reference templates with distorted tumor images. Work is being done in an attempt to reduce 4DCT artifacts (Li *et al* 2009a), which could translate into improved reference templates and tracking results for this algorithm.

Changes in the anatomy or respiratory pattern pose perhaps the most difficult challenge for template based tracking algorithms. If, for example, the patient is breathing with much larger amplitude during treatment than is represented by the 4DCT, there may be no reference templates corresponding

to the extreme tumor positions. This type of "out of range" problem is partially managed by shifting the templates to extend the range covered, but this technique only helps over a limited range, as a rigid template shift does not account for movement or deformation of other anatomy. If available, 4D CBCT could be used to generate new templates on the day of treatment, minimizing the effects of interfractional variations. Intrafractional changes in breathing patterns could still cause difficulty (Keall *et al* 2006). Breathing-coaching could also be helpful in encouraging patients to produce regular, reproducible breathing patterns. For our study of three patients, templates generated from 4DCT acquired approximately two weeks prior to treatment, combined with template shifting, appeared to be adequate. This evidence is however only anecdotal, and a more thorough study needs to be conducted in order to test the robustness of this algorithm to irregular breathing and tissue deformations.

The DRR algorithm used to generate reference templates may also have an effect on the quality of the reference templates. DRRs should be generated by a model which represents the actual imaging system as closely as possible. In theory, a well designed DRR generation algorithm used on an artifact-free CT volume could produce DRRs with pixel values that correspond linearly to actual cone-beam projection images. In this case, a simpler similarity metric such as normalized cross correlation would be ideal. In practice, it may not be realistic to depend on such accurately generated DRRs. For example, if the x-ray energies used to obtain 4DCT data and CBCT

projections are different, the ratio of bone to tissue attenuation will also change, and the relationship between intensity values will be nonlinear. A similarity measure which does not assume a linear relationship, NMI, was selected for this tracking algorithm to help mitigate such potential differences between generated DRRs and real cone-beam projection images. When using NMI as a similarity measure for 2D/2D registration, troubles can arise if not enough pixels are present to accurately estimate the joint probability distribution function (Penney *et al* 1998). In a previous study of markerless spine tracking in fluoroscopic images it was shown that NMI is a suitable similarity measure for template sizes comparable to those used in this work ($\sim 10^4$ pixels), and claimed that NMI performed better than cross correlation for their data (Rohlfing *et al* 2005). Figure 2.13 shows a map of NMI scores over the 21 x 21 pixel window through which a template was allowed to shift for a projection from patient 1 (upper left). Scores on the map range from 0.151 to 0.186, with contour lines representing 5% increases between these values. Joint histograms are shown for positions successively closer to the template match, including 10 pixels off in both directions (upper right, NMI =0.161), 5 pixels off in both directions (lower left, NMI =0.173) and the best match (lower right, NMI =0.186). As the match point is approached, the dispersion in the joint histograms appears to decrease, as expected. The relationship shown in the joint histogram corresponding to the highest NMI score appears to be not quite linear. If the relationship is linear, then cross

correlation may be a preferable similarity measure. Whether or not linearity can be assumed will depend on the data; particularly on the process used to generate DRRs. NMI can work as a similarity measure for both linear and nonlinear relationships.

Speed is a concern if the algorithm is to be applied to a real-time tracking rotational treatment. DRR generation from 4DCT could be done prior to treatment by estimating the expected location of the rotational isocenter during CBCT scans, but the location of the isocenter relative to the patient's anatomy could change based on how the patient is set up. Errors may occur unless DRRs are generated after an initial registration of CBCT and 4DCT volumes. In this preliminary study, DRRs with pixel dimensions 768 x 1024 were computed in approximately 10 seconds using a 2.67 GHz processor with 8 GB of ram. Under these conditions, computing 10 DRRs for a set of 650 patient projections would require about 10 hours, which is obviously much too long for the practical use. A simple CUDA implementation of the algorithm was able to generate similar DRRs in approximately 50 ms using an NVIDIA Tesla C1060 GPU card. This 200 times speedup factor means DRRs could be generated in about 3 minutes. Parallel GPUs could be used for an even greater speedup factor. The next computationally intensive task in tracking is computing the similarity score between the images. Computation of NMI using the 2.67 GHz processor took approximately 1 ms for a 200 x 100 pixel ROI. Including template selection, and using a 21 x 21 pixel search window

with two templates, this calculation must be made 891 times per projection, taking approximately 0.9 seconds. This is an unacceptable length of time since the tumor could move substantially in 0.9 seconds. In the future, the similarity score computation will be implemented on GPU. Since the calculation for each point within the 21 x 21 pixel search window can be performed independently, a significant speedup factor is expected.
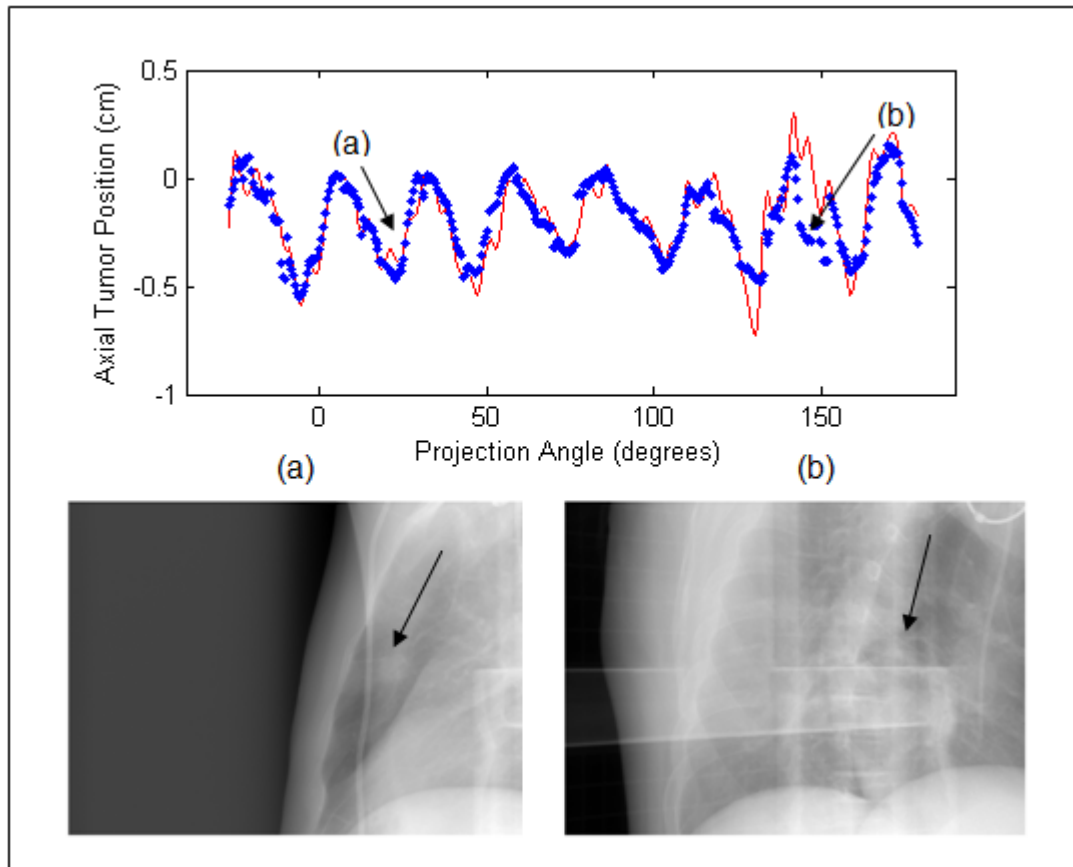
Figure 2.12:   Examples showing poor tracking results when view of tumor is obstructed by other high contrast objects. The projection image corresponding to the good tracking results at point (a) is shown on the left, while the image corresponding to the poor tracking result at point (b) is shown on the right.
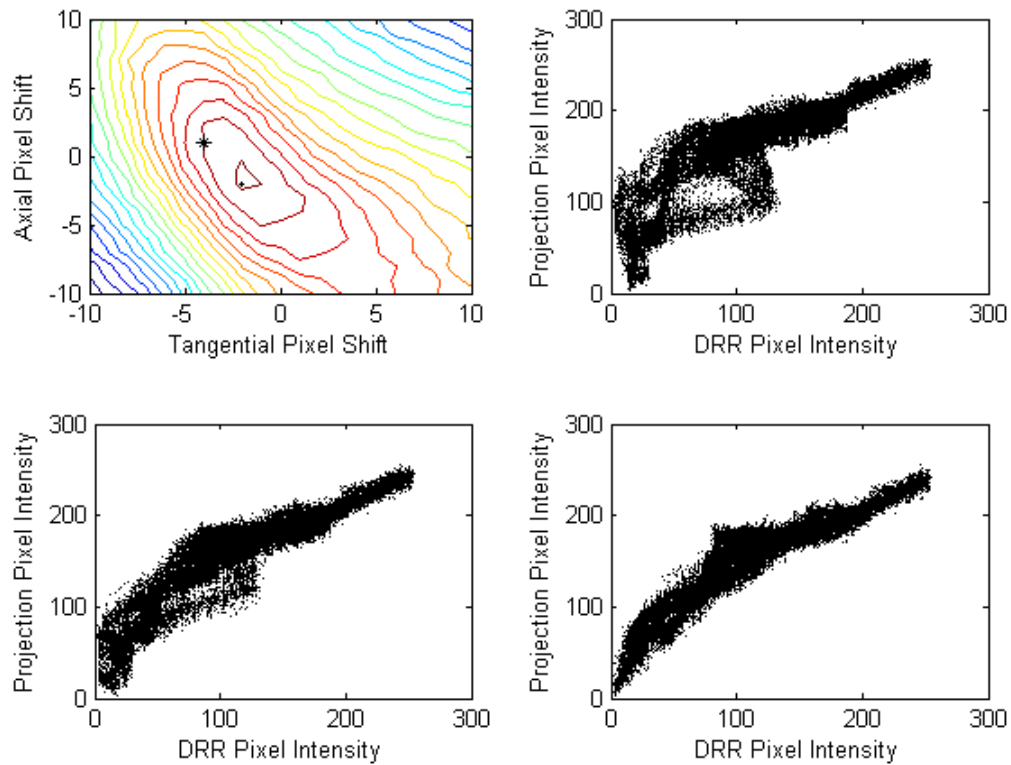
Figure 2.13: A contour map of NMI scores with corresponding joint histograms for a patient projection. Contour lines represent 5% changes. Max NMI is a dot and true position a star. Histograms represent positions 10 (upper right, NMI =0.161), 5 (lower left, NMI =0.173) and 0 pixels away from max NMI (lower right, NMI =0.186).

2.6. Conclusion

An algorithm for direct tumor tracking in rotational cone-beam projections was developed. The feasibility of the algorithm was demonstrated on a digital phantom, a physical phantom, and three patients. While the patient tracking results are promising, future refinement is needed to achieve more clinically palatable accuracy. The largest source of error appears to be difficulty in tracking the tumor at angles where other high contrast objects

intervene close to the tumor in the projections. These errors will be addressed in part by the diaphragm-based tracking work of Chapter 5. The remaining chapters of this dissertation are based upon the tracking algorithm described in this chapter.

This chapter contains material published in Physics in Medicine and Biology 2010. Lewis, John H.; Li, Ruijiang; Watkins, W. Tyler; Lawson, Joshua D.; Segars, W. Paul; Cerviño, Laura I.; Song, William Y.; Jiang, Steve B., IOP Publishing. The dissertation author was the primary investigator and author of this paper.

3.   Daily 3D Trajectory Reconstruction from Rotational Tracking Results

3.1. Overview

Modern highly conformal radiation therapy provides treatments which conform exquisitely to the target's shape, and allow for enhanced normal tissue sparing. With such precisely designed treatments, it is of critical importance to know the exact location of a lung tumor on the day of treatment. Studies have shown that a tumor's mean position and amplitude can change substantially between treatments, so it is not advisable to rely on information about a tumor's trajectory that was acquired during simulation (Seppenwoolde *et al* 2002, Berbeco *et al* 2005a, Berbeco *et al* 2006, Shirato *et al* 2006, Ionascu *et al* 2007, Nishioka *et al* 2008, Sonke *et al* 2008). Modern on-board volumetric imaging techniques like CBCT can provide information about a tumor's location on the day of treatment, which could be used to position the

patient, to recalculate and evaluate the dose distribution that would be delivered by a treatment, or possibly to develop new adaptive treatment plans online (Jaffray *et al* 2002, Langen *et al* 2005, Meeks *et al* 2005, Oldham *et al* 2005, Pouliot *et al* 2005, Yang *et al* 2007). Unfortunately, current CBCT scanners take about 60 seconds or longer to acquire a set of projections for reconstruction. When scanning a lung patient, the patient will breathe multiple times during this interval, and the resultant image of a moving tumor will be greatly blurred by motion artifacts. This blurring makes it difficult or impossible to precisely locate a tumor's position, shape, or size.

The severity of motion artifacts in conventional 3D CBCT scans has motivated a substantial amount of work in 4D CBCT (Sonke *et al* 2005, Dietrich *et al* 2006, Li *et al* 2006b, Li *et al* 2007, Li and Xing 2007). The respiratory correlated volumes generated by 4D CBCT exhibit greatly diminished motion artifacts, and give information about the motion of the tumor and organs on the day of treatment. However, since several phase-binned volumes are reconstructed, the total number of projections must be divided amongst the bins. The lower number of projections available for reconstruction will cause severe view-aliasing artifacts using regular CBCT reconstruction algorithms (Feldkamp *et al* 1984). In order to avoid this problem, acquisition protocols for 4D CBCT have been modified either by slowing down gantry rotations, or by acquiring projections in multiple gantry rotations (Sonke *et al* 2005, Li *et al* 2006b). These methods extend the projection acquisition time by

a factor of four or more, and may also lead to increased imaging dose to the patient. These problems have preventing 4D CBCT from becoming standard for daily patient imaging.

In this chapter, a method for reconstructing the trajectory of a tumor from a set of projections acquired during a normal 3D CBCT acquisition is presented. While the method presented is tailored to handle the possibility of larger tracking errors associated with markerless tracking, the algorithm is general and could be modified slightly for application to tracking results acquired via other methods. As presented here, the algorithm only reconstructs the motion of the centroid of the tumor, and does not give information about the shape of the tumor or other organs on the day of treatment. Depending on the task, often the motion of the tumor provides enough information by itself (*e.g.,* patient positioning), but in some cases it may be desirable to know the shape and size of the tumor too (*e.g.,* dose calculation). A method for using the reconstructed trajectory as determined by the algorithm in this chapter in order to reconstruct the tumor size and shape on the day of treatment will be presented in Chapter 4.

3.2. Methods

Reconstructing the complete 3D trajectory of a tumor from tracking results acquired in a series of rotational 2D projections is an underdetermined

problem unless some additional information about the tumor's trajectory is available. In the case of respiratory induced lung tumor motion, the assumption of periodic regular breathing is reasonable, and is commonly used for phase binning in both 4DCT and 4D CBCT. The reconstruction algorithm employed here uses the same assumption in order to reconstruct a phase-binned tumor trajectory from direct tracking results as acquired by the methods in Chapter 2.

In order to reconstruct the tumor's 3D trajectory, line segments were found connecting the x-ray source with the tracked position of the tumor in the imager for each projection. These line segments were then separated into phase bins based on a respiratory signal (explained below for each data set). Figure 3.1 shows these line segments for one CBCT scan, with each graph representing a different phase bin. In the ideal case where a tumor did not undergo any residual motion within each phase bin and the tracking results were perfect, all of the line segments within one phase bin would intersect at one point in space, representing the 3D position of the tumor within that phase bin. In reality, the tumor does move some within the phase bin, and tracking results exhibit some error, so the line segments will not intersect at one point. In order to approximate the point represented by a set of line segments within a phase bin, a point is found which minimizes $J = \sum_k d_k^2$, where d_k^2 is the squared distance between a point $\mathbf{x}_0$ and a line defined by two points $(\mathbf{x}_{k2}, \mathbf{x}_{1k})$, and k indexes the line segments in each phase bin. To find the

point which minimizes J for a set of lines, the derivative of J with respect to $\mathbf{x}_0$ is set it to 0, and used to solve for $\mathbf{x}_0$

$$\frac{\partial J}{\partial \mathbf{x}_0} = \frac{\partial \sum_k d_k^2}{\partial \mathbf{x}_0} = 0 \, , \tag{3.1}$$

Some markerless tracking results may have significant tracking errors. For example, larger errors may occur when images are acquired from angles at which the tumor is difficult to see due to interfering structures such as the treatment couch, spine, or heart, or when breathing patterns or tissue deformations occur that are not well represented by the reference templates. In order to manage these uncertainties and increase the accuracy of phase-binned trajectory reconstruction, an iterative approach was taken in which the lines farthest away from the calculated point were discarded before the point was recalculated. The iterations terminated when either all lines score within a predefined value d_l, or the total number of lines in a phase bin became lower than a selected threshold. In this way, a phase-binned tumor trajectory was obtained, representing the average tumor motion on the day of treatment. For the purposes of this study, this threshold was chosen to be 20 lines, while d_l was selected as approximately 30% of the expected tumor amplitude (estimated from 4DCT for patient data). This choice of threshold was meant as

a rough upper bound of the largest residual motion expected within any phase bin.
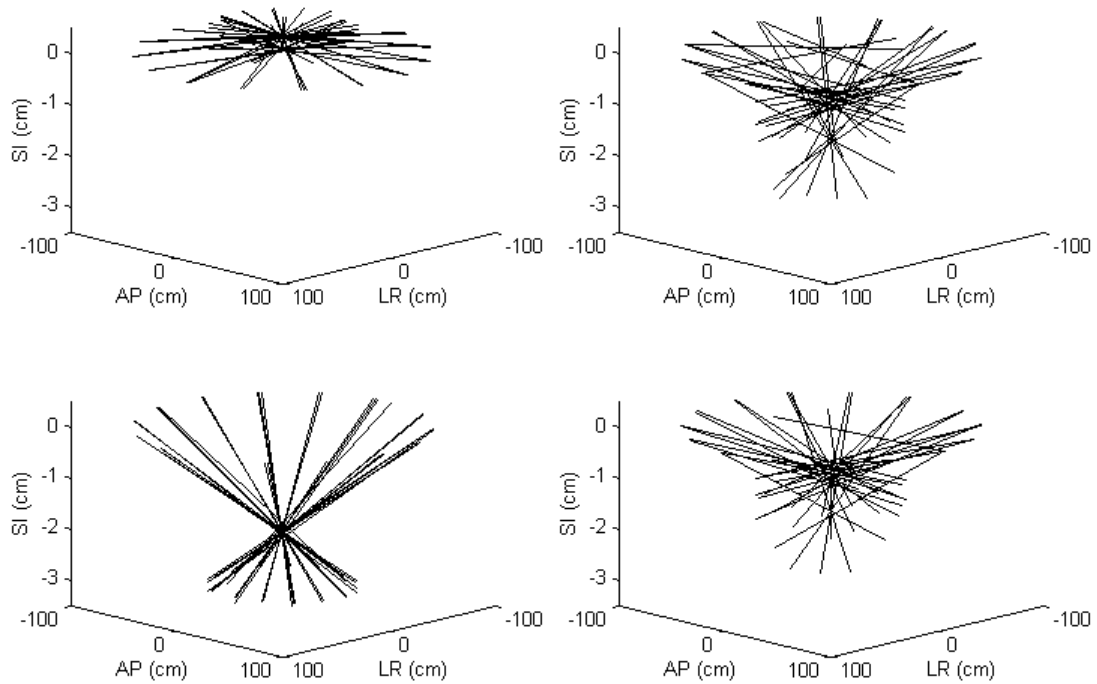
Figure 3.1: Examples of phase-binned tracking results for full exhalation (upper left) mid inhalation (upper right) full inhalation (lower left) mid exhalation (lower right). Line segments connect the source position to the position that the tumor appears at in the imager for each projection.

3.3. Materials

Trajectories reconstructed in this chapter will be derived from the tracking results obtained for the phantoms and patients as described in Chapter 2. In the following sections of this chapter details are given describing

the phase binning process for each phantom and patient, as well as the way ground truth was defined in each case.

3.3.1. Digital NCAT phantom data

The breathing signal used to phase bin the tracking results for 3D trajectory reconstruction of the digital NCAT phantom was based on the known phase of the phantom in each projection. For a trajectory ground truth, the 100-bin high resolution phantom was separated into 10 larger bins, and the average position of the tumor within each of these 10 bins was computed.

3.3.2. Physical phantom data

The breathing signal used to phase bin the tracking results for 3D trajectory reconstruction was extracted from the programmed sinusoidal motion of the phantom. The average position of the target within each of the 10 phase bins was used as ground truth for comparison.

3.3.3. Patient data

Diaphragm motion was used as a breathing signal surrogate for phase binning of tracking results. The maximum and minimum positions of the diaphragm were manually selected for each breathing cycle, defining the

maximum exhale and inhale phase bins. Other phase bins were defined by evenly dividing the time between maximum and minimum positions. Assignment to phase bins could also be based on monitoring of an external surrogate, tidal volume measurements from a spirometer, or directly from tumor tracking results. The simple use of the diaphragm appeared satisfactory in this study.

Since the true 3D trajectory of the tumor is not known in the patient studies, a ground truth was instead approximated based on the clinician-defined tumor positions in each projection. Phase-binned ground truth trajectories were derived by applying the algorithm described in Section 3.2 to the clinician-defined tumor positions in projection images. In the future, a ground truth for the reconstructed trajectory could be better defined based upon a high quality 4D CBCT. Unfortunately we are currently unable to reconstruct such a data set given the clinical imaging protocol at the University of California, San Diego Moores Cancer Center.

3.4. Results

3.4.1. Digital NCAT phantom results

As described in Chapter 2, a digital phantom was created with 2.3 cm SI tumor amplitude, 0.9 cm AP amplitude, 0.2 cm LR amplitude, and a breathing period of 4 seconds. A 1.8 cm diameter tumor was positioned in the

middle of the right lung. The tracking results obtained in Chapter 2 were used to reconstruct the phase-binned tumor trajectory shown in Figure 3.2, with associated errors described in Table 3.1. The reconstructed trajectory was represented by 10 phase bins, with a maximum 3D error of 0.6 mm and a 3D e_{rms} of 0.4 mm.
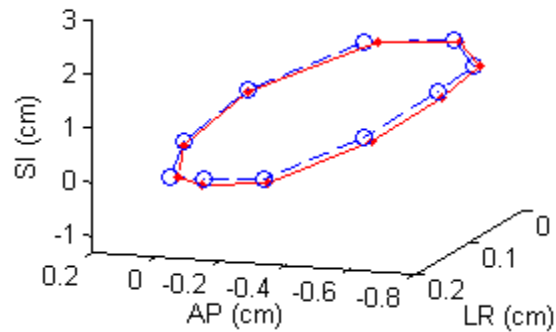
Figure 3.2: A reconstructed tumor trajectory from NCAT phantom tracking results. The blue circles (connected by dashed lines) represent the algorithm output, while the red dots (connected by solid lines) represent the tumor position ground truth.

Table 3.1: Maximum error and e_{rms} in the reconstructed phase-binned tumor trajectory for NCAT phantom.

	max (mm)	erms (mm)
SI	0.5	0.3
LR	0.2	0.1
AP	0.3	0.2
3D	0.6	0.4

3.4.2. Physical phantom results

The physical phantom was programmed to move sinusoidally in the SI direction with 4 second period and 1.5 cm amplitude. 359 projections were

acquired over an arc of 200 degrees with a frequency of 10.7 Hz. The tumor

trajectory reconstructed using the tracking results from Chapter 2 is plotted in

Figure 3.3, with corresponding error values shown in Table 3.2. The trajectory

was represented by 10 phases, and resulted in a maximum 3D error of 1.0

mm, and a 3D e_{rms} of 0.5 mm.
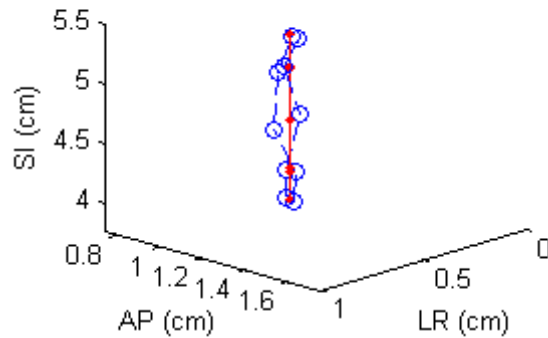
Figure 3.3: A reconstructed tumor trajectory from physical phantom tracking results. The blue circles (connected by dashed lines) represent the algorithm output, while the red dots (connected by solid lines) represent the ground truth target position.

Table 3.2: Maximum error and e_{rms} in the reconstructed phase-binned tumor trajectory for physical phantom.

	max (mm)	erms (mm)
SI	0.4	0.2
LR	0.4	0.3
AP	0.8	0.3
3D	1.0	0.5

3.4.3. Patient results

The tracked tumor for patient 1 was located in the left lower lobe, just above the patient's diaphragm in the periphery of the lung. From the 4DCT acquired during simulation, the tumor was estimated to have 1.8 cm diameter, and motion with 4.4 second period, 1.4 cm SI amplitude, 0.2 cm AP amplitude, and 0.9 cm LR amplitude.

In patient 2 the tracked tumor was located near the center of the left lung. From 4DCT the tumor's trajectory was estimated to have a 2.7 second breathing period and 0.5 cm, 0.3 cm, 0.4 cm amplitudes in the SI, AP, and LR directions respectively. The tumor was approximately 1.2 cm in diameter.

In patient 3 the tracked tumor was located in the lower right lung near the spine. The tumor's trajectory was estimated to have a 3.0 second breathing period and 1.9 cm, 0.1 cm, 0.1 cm amplitudes in the SI, AP, and LR directions respectively. The tumor was approximately 1.2 cm in diameter.

Trajectories for patients 1, 2, and 3 are plotted in Figure 3.4, Figure 3.5, and Figure 3.6 respectively, with corresponding errors reported in Table 3.3, Table 3.4, and Table 3.5 respectively. The trajectories were represented with 10 phase bins for each patient, with a maximum 3D error of 2.0 mm, 1.4 mm, and 2.1 mm for patients 1, 2 and 3 respectively. The 3D e_{rms} was 1.3 mm for patient 1, 0.7 mm for patient 2, and 1.3 for patient 3.
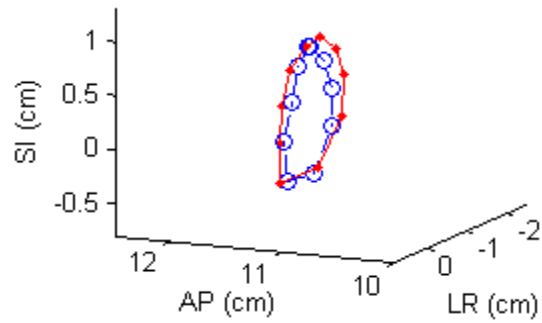
Figure 3.4: A reconstructed tumor trajectory from patient 1 tracking results. The blue circles (connected by dashed lines) represent the algorithm output, while the red dots (connected by solid lines) represent the ground truth tumor position.

Table 3.3: Maximum error and e_{rms} in the reconstructed phase-binned tumor trajectory for patient 1.

	max (mm)	erms (mm)
SI	1.0	0.6
LR	1.7	1.2
AP	0.6	0.4
3D	2.0	1.3
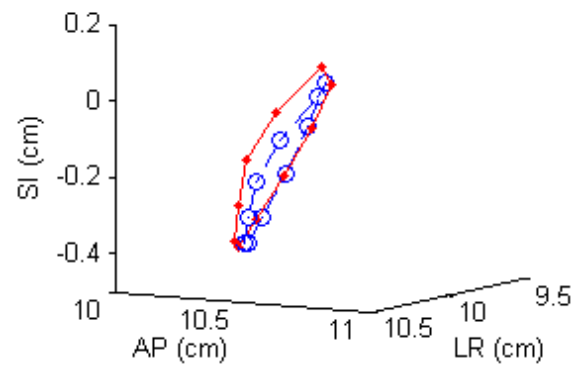
Figure 3.5: A reconstructed tumor trajectory from patient 2 tracking results. The blue circles (connected by dashed lines) represent the algorithm output, while the red dots (connected by solid lines) represent the ground truth tumor position.

Table 3.4: Maximum error and e_{rms} in the reconstructed phase-binned tumor trajectory for patient 2.

	max (mm)	erms (mm)
SI	0.6	0.3
LR	0.9	0.5
AP	0.8	0.4
3D	1.4	0.7
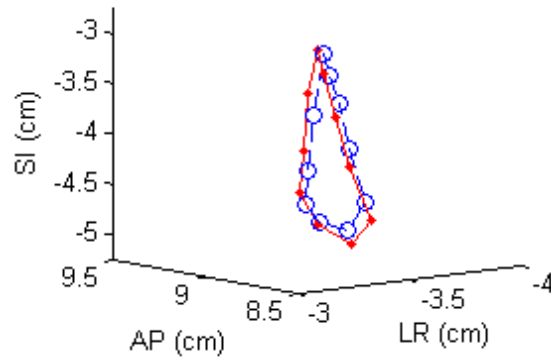
Figure 3.6: A reconstructed tumor trajectory from patient 3 tracking results. The blue circles (connected by dashed lines) represent the algorithm output, while the red dots (connected by solid lines) represent the ground truth tumor position.

Table 3.5: Maximum error and e_{rms} in the reconstructed phase-binned tumor trajectory for patient 3.

	max (mm)	erms (mm)
SI	2.0	1.2
LR	0.4	0.2
AP	0.8	0.4
3D	2.1	1.3

3.5. Discussion

Accurate phase-binned tumor trajectories were successfully reconstructed for both patients and phantoms. In all cases, errors in the reconstructed tumor trajectory were substantially smaller than the errors in the

direct tracking results (reported in Chapter 2). The smaller errors were a result of both the averaging effect of using many tracking results in each phase bin, and the elimination of large outliers using the iterative method described in Section 3.2. All errors in the reconstructed tumor trajectories were 1.0 mm or less in each direction, except for the LR direction of patient 1 (1.7 mm) and the SI direction of patient 3 (2.0 mm). Patient 1 exhibited a large magnitude LR motion (0.9 cm), which probably led to the increased error. The tumor for Patient 3 was located near the spine and had significantly larger tracking errors. Even in these cases, the maximum 3D error did not exceed 2.1 mm. While these errors may be reduced further by improved, more accurate tumor tracking, they are already small enough that the trajectory information could be clinically useful.

The primary way of improving the accuracy of reconstructed tumor trajectories would be to improve the tracking results used. Possible ways to improve the tracking algorithm were discussed in Chapter 2, and will be explored further in Chapter 5. The trajectory reconstruction algorithm itself could possible be improved by developing or more intelligent way of discarding bad tracking results before reconstructing the trajectory. For example, if all templates for a particular cone-beam projection score a very low similarity score, the corresponding tracking result may be considered less reliable. An attempt was made to implement this method, but improved trajectories were not successfully reconstructed. Relying on the actual value of similarity scores

may not be a good choice, since the score also varies depending on image content, which changes significantly for different projection angles.

As with any method that relies on phase-binning of data (such as 4DCT and 4D CBCT), irregular breathing patterns could pose problems for this method of trajectory reconstruction. In fact, if breathing is quite irregular, the usefulness of reconstructing one "representative" trajectory from 10 phase-binned points is very questionable. This technique would not be appropriate for patients who are unable to maintain stable breathing patterns. Breathing-coaching could help to ensure that breathing patterns remain stable.

While the complete trace of the lung tumor's motion during a CBCT scan would provide more information, the most clinically important information is still supplied in a phase-binned trajectory, and it is unclear how beneficial the extra information in a complete trace would be in most clinical settings. Choosing to reconstruct only the phase-binned trajectory also allowed for the simple iterative way of eliminating less reliable tracking results. This algorithm relies on the assumption that the tumor trajectory is periodic and a phase-binned trajectory is therefore meaningful. This assumption is reasonable for respiratory motion, but not good for other types of motion (such as that exhibited by the prostate).

3.6. Conclusion

An algorithm for the reconstruction of a lung tumor trajectory on the day of treatment using only projections acquired during regular 3D CBCT acquisition has been developed. Accurate phase-binned trajectories were reconstructed in each case despite poor markerless tracking results in some projection images. Such a trajectory could be useful for daily analysis of tumor motion, especially for patient setup for gating treatments. The trajectories can also be used to remove motion blurring artifacts from a reconstructed CBCT volume, and to reconstruct a tumor's size and shape on the day of treatment, as will be discussed in Chapter 4.

This chapter contains material published in Physics in Medicine and Biology 2010. Lewis, John H.; Li, Ruijiang; Watkins, W. Tyler; Lawson, Joshua D.; Segars, W. Paul; Cerviño, Laura I.; Song, William Y.; Jiang, Steve B., IOP Publishing. The dissertation author was the primary investigator and author of this paper.

4. Removing Motion Blurring Artifacts

4.1. Overview

In the preceding chapters of this dissertation, methods have been presented to extract tumor centroid motion from a set of cone-beam projections acquired during a regular 60 second 3D CBCT scan. For some applications, such as monitoring daily changes in tumor motion, the previous work is adequate. However, during an extended fractionated radiation therapy, a tumor may change size or deform (Markman 1996, Kim and Spencer 2000, Erridge *et al* 2003, Puglisi *et al* 2004, Melmed *et al* 2005, Kopans 2006, Lotz *et al* 2006, Tuma 2006, Henzel *et al* 2009). In fact, tumor shrinkage is often considered desirable, and may sometimes be used as a measure of a tumor's response to treatment (Rubinstein *et al* 2007, Birchard *et al* 2009, Bruno and Claret 2009, Piessevaux *et al* 2009). There are situations in which knowledge of the daily tumor shape could improve treatment quality. It may be helpful to be aware of daily tumor changes when deciding if dose calculations and

treatment plans derived from images acquired during simulation are still appropriate, or if an adapted plan is necessary. For example, knowledge of changes in a tumor's structure could allow for beam shaping parameters to be adjusted in order to deliver a more appropriately conformal dose distribution.

As discussed in previous chapters, moving objects such as tumors appear distorted in reconstructed CBCT images. In order to reconstruct the correct shape of the tumor, the distorting effects of motion must be removed from the image. In addition to distortions caused by motion, noise in CBCT images increases the difficulty of removing motion artifacts. The problem of removing blurring effects from noisy images has been well studied in the field of image processing, leading to the development of multiple potential solutions including both iterative (*e.g.,* Richardson-Lucy deconvolution) and non-iterative (*e.g.,* Weiner deconvolution) algorithms (Richards.Wh 1972, Lucy 1974, Katsaggelos 1991, Favaro and Soatto 2007). Such algorithms can generally be used to reduce blur caused by various mechanisms, such as optical distortions present in images acquired with microscopes, telescopes, or other imaging devices, and motion distortions present in medical or other images (Ancin *et al* 1996, Carasso 2006, Levoy *et al* 2006, Zhulina 2006). The choice of algorithm depends on the specific requirements of the problem.

A substantial amount of effort has been invested in developing methods to reduce the presence of artifacts caused by motion in conventional CT imaging, positron emission tomography (PET), and magnetic resonance

imaging (MRI) (Atalar and Onural 1991, Wang and Vannier 1995, Willis and Bresler 1995, Crawford *et al* 1996, Ritchie *et al* 1996, Dhanantwari *et al* 2001, Bonnet *et al* 2003, Buhler *et al* 2004, Blondel *et al* 2006, Reyes *et al* 2007, Lewis and Jiang 2009). The problem was first cast as a time-varying tomography problem by Willis and Bresler (1995). Crawford *et al* (1996) adapted the problem to CT, and used a parametric model for respiratory motion to derive an exact reconstruction formula for motion compensation in CT scans. Ritchie *et al* (1996) improved the model by adopting a more realistic motion model for thoracic CT scans. The performance of these algorithms depends critically on the motion model used. When actual motion does not adhere to the model used, the quality of reconstructed images can deteriorate rapidly (Crawford *et al* 1996, Linney and Gregson 2001, Ablitt *et al* 2004). Bonnet *et al* provide a review of methods used to account for motion in x-ray computed tomography (2003).

More recently, methods of reducing respiratory motion artifacts applicable to CBCT have been of great interest (Sonke *et al* 2005, Li *et al* 2006a, Li *et al* 2006b, Li *et al* 2007, Rit and Sarrut 2007, Rit *et al* 2008, Rit *et al* 2009a). The approaches can generally be divided into two categories: 1) techniques which separate acquired projections into bins in order to separately reconstruct multiple respiratory-correlated volumes (*i.e., 4D CBCT)*; and 2) techniques which use a respiratory motion model to compensate for motion in the reconstruction process. The first approach was discussed in detail in

Chapter 3 of this dissertation, with the primary drawback being the need for sufficient sampling during projection acquisition to reconstruct multiple volumes of reasonably high quality. The second approach avoids this problem by using a motion model to allow all acquired projections to be used to reconstruct one motion-compensated volume. The development and widespread use of 4DCT has allowed for patient specific motion models to be derived based on deformable registration between phase-binned volumes. Li *et al* used 4DCT to develop such a model, and incorporated it into a modified FDK algorithm which accounts for deformation during backprojection (2006).

A significant shortcoming of approaches based on motion models derived from 4DCT is the assumption that the motion model derived during simulation is still valid at the time of treatment. Given the dependence of motion compensation algorithms on the accuracy of a motion model, there is a need for a motion deblurring algorithm which incorporates knowledge of a patient's motion *during* CBCT acquisition (*i.e.,* without relying on a model derived from 4DCT). The purpose of this work is to develop such an algorithm based on motion information acquired by object tracking performed on rotational cone-beam projections.

4.2. Methods

4.2.1. Deblurring model

A simple model for the blurring effects of motion on CBCT reconstruction can be written as:

$$i = f * g + n, \tag{4.1}$$

where i is the blurry reconstructed CBCT image, f is a motion blurring function, g is the true, non-blurred volume, and n is some random noise (which we will assume to be Gaussian). Various reconstruction artifacts may be present which complicate the model stated above, but are not considered for these purposes. The goal of deconvolution is then to determine g given some reconstructed CBCT image i. Without any additional knowledge, this is a blind deconvolution problem, and is very difficult to solve. In this work, we will use the tracking methods discussed in previous chapters to construct an estimate of the motion blurring function, and incorporate it into the deconvolution procedure.

A diagram of the motion correction procedure proposed is shown in Figure 4.1. Rotational x-ray projections acquired during a CBCT scan are used separately for tumor tracking and for image reconstruction. The tumor tracking results are used to estimate the motion blurring function f. The motion

blurring function and the reconstructed image are the inputs to a deconvolution algorithm, which outputs the motion-corrected CBCT image.
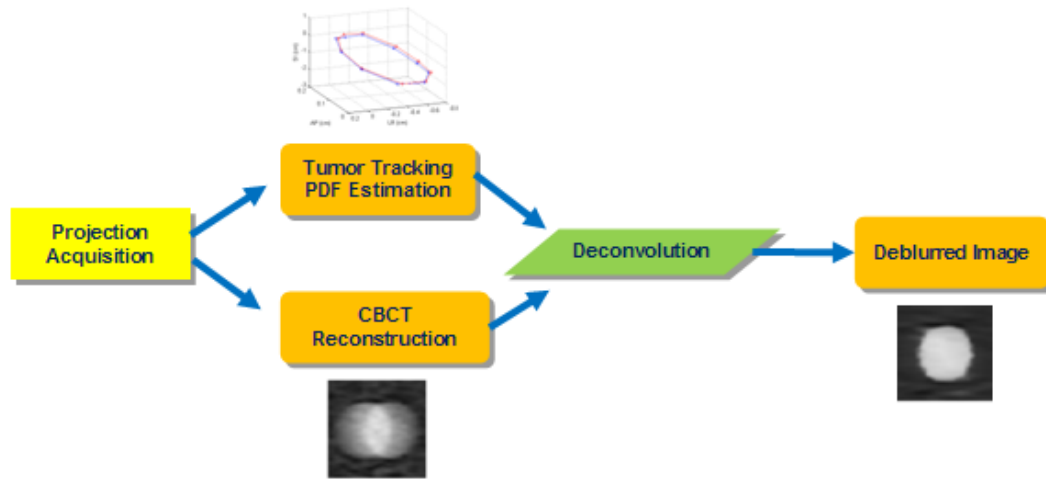
Figure 4.1: A flow chart showing the proposed method of artifact removal for CBCT images. The projections are used both for tracking and image reconstruction, then the blurry reconstructed image and the tracking results are input into the deconvolution algorithm. The motion corrected volume is output.

4.2.2. Deconvolution algorithm

Deconvolution is performed through minimization of the following cost function:

$$E = \left\| f * g - i \right\|_2^2 + \lambda \left\| g \right\|_{TV}, \tag{4.2}$$

where the first (data fidelity) term ensures that the recovered image convolved with the motion blurring function is similar to the original reconstructed volume

in the least mean squared error sense, and the second term is a total variation (TV) norm regularization term with weighting factor λ. The TV norm of g is the L1-norm of the magnitude of the gradient of g, *i.e.,*

$$\|g\|_{TV} = \int |\nabla g(x)| dx. \tag{4.3}$$

This TV norm regularization term has been used in other image processing applications (Rudin *et al* 1992). It has been demonstrated that the TV norm regularization term is able to remove artifacts and noise in the reconstructed images, while preserving sharp edges to a large extent. Other regularization methods such as Tikhonov regularization rely on an L2-norm, and tend to smooth out jump discontinuities, blurring edges in images. For imaging in radiation therapy, boundaries of tumors, organs, and other structures are of primary importance. Therefore, TV norm regularization is a well-suited choice. The choice of regularization based on knowledge of the goals of deconvolution can be thought of in some sense as an incorporation of prior knowledge.

The cost function shown in Equation 4.2 is minimized via gradient descent. The gradient of E with respect to g is

$$-\nabla_g E = -2f * (f * g - i) + \lambda \left(\nabla \cdot \frac{\nabla g}{|\nabla g|} \right). \tag{4.4}$$

This gradient is used to iteratively update g with

$$\frac{dg}{d\tau} = -\nabla_g E,$$ (4.5)

where τ is an artificial time step, until the value of g which minimizes E is determined. This resultant value of g is the final motion-corrected CBCT image. λ controls the smoothness of the image and is selected manually for best image quality.

4.2.3. Motion blurring function estimation

For the purposes of this work, we assume that the motion blurring function can be well estimated by a motion probability density function (PDF) of the target's motion during the CBCT scan. In some sense this is an assumption that the reconstructed CBCT is a time average of the tumor's motion during projection acquisition. This is a reasonable assumption given that the period of a tumor's motion is very small (~4 seconds) compared to the acquisition time for CBCT (~60 seconds).

A motion PDF for the tumor during the CBCT scan can be generated using the tracking and trajectory reconstruction techniques described in Chapters 2 and 3. Reconstructed 3D trajectories of target motion were fit with

cubic splines and up-sampled to generate higher resolution points along the target's trajectory. These points were then convolved with a spherical 3D Gaussian kernel in order to generate a PDF of the target's motion.

4.3. Materials

4.3.1. Digital phantom data

The algorithm was initially tested on the digital NCAT phantom described in Section 2.3.1. The tumor is represented by a 1.8 cm diameter sphere with uniform density. 100 frames were created representing one complete motion cycle with a 4 second period, 2.3 cm SI amplitude, 0.9 cm AP amplitude, and 0.0 cm LR amplitude of tumor motion. These 100 frames were averaged together to generate one motion blurred "average" volume. This generated volume is meant to simulate the time averaging effects of a slow CBCT scan. Motion PDFs were generated using the estimation procedure described above based on tracking and trajectory reconstruction results acquired using the methods of Chapters 2 and 3. The variance of the Gaussian kernel was selected as 0.4 mm based on the estimated error in the reconstructed trajectory. The results of the deblurring algorithm are compared to a generated stationary phantom volume.

4.3.2. Physical phantom data

The deblurring algorithm was tested on the physical phantom described in Section 2.3.2. Two phantom CBCT volumes were acquired: one with the phantom stationary, and one with the phantom moving sinusoidally in the SI direction with 1.5 cm amplitude and 4 second period. The tumor is represented by an approximately spherical object with lengths 2.7 cm, 2.6 cm, and 2.9 cm along the SI, AP, and LR axes respectively. Motion PDFs were generated using the estimation procedure described above based on tracking and trajectory reconstruction results acquired using the methods of Chapters 2 and 3. The variance of the Gaussian kernel was selected as 0.5 mm based on the estimated error in the reconstructed trajectory. The deblurring algorithm was applied to the motion-blurred CBCT volume, which was then compared to the image of the stationary phantom.

4.3.3. Patient data

The algorithm was also applied to an example patient case. Patient 3 from of Chapter 2 was selected because of the tumor's relatively large motion and well defined borders. Patient 1 from Chapter 2 was excluded because the tumor was directly on top of the diaphragm, and its border along the major axis of motion (SI) was difficult to discern. Patient 2 from Chapter 2 was excluded because motion was small, and blurring effects in the reconstructed CBCT were minimal. Deblurring was performed on a CBCT acquired from a lung

cancer patient immediately prior to treatment. A motion PDF was constructed based on the tracking and trajectory reconstruction techniques described in previous chapters. The variance of the Gaussian kernel was selected as 1.3 mm based on the estimated error in the reconstructed trajectory. The tumor being deblurred was located in the lower right lung, near the spine. The trajectory of the tumor had amplitude of approximately 1.9 cm in the SI direction, 0.1 cm in the AP direction, and 0.1 cm in the LR direction, and an average period of 3.0 seconds.

A 4DCT acquired during simulation was used as a reference "stationary" volume to which the deblurred CBCT was compared. The use of 4DCT as a reference is not ideal since anatomy, including the tumor, can move and deform between 4DCT and CBCT acquisitions. The 4DCT only gives an estimate of the correctly deblurred CBCT volume, since differences between the deblurred CBCT and the 4DCT may represent actual anatomical changes, and not errors is the deblurring algorithm. Based on the 4DCT, the tumor measured 1.6 cm along the SI dimension, 1.4 cm along the AP dimension, and 1.1 cm along the LR dimension.

A more ideal volume for comparison to the deblurred CBCT would be a reference 4D data set acquired at the same time as the CBCT. Unfortunately, it is uncommon for 4D volumes to be acquired at the time of treatment, largely due to concerns of increased imaging time and dose, as discussed in

Chapters 2 and 3. Such data is not available at our institution given the clinical imaging protocol used for lung cancer patients.

4.3.4. Evaluation of performance

The algorithm's performance was evaluated based on three criteria: 1) the normalized mean squared error ($NMSE$), defined below; 2) intensity line profiles taken through the tumor; and 3) qualitative image comparison. $NMSE$ is defined as

$$NMSE = \sqrt{\frac{\sum_i \left(A_i - B_i\right)^2}{\sum_i B_i^2}} \quad , \tag{4.6}$$

where i indexes the pixels of the image, and A and B are the images being compared. Since $NMSE$ measures the difference between two images, the deblurred image should have lower $NMSE$ than the original motion-blurred image when each is compared to the stationary reference image. $NMSE$ is however not necessarily the most relevant measure of performance, since it accounts for all differences in the images. For many practical purposes, it is only the shape and size of the tumor that is important. Line profiles shown in the results section give an idea of how accurately the dimensions of the tumor have been recovered, and how sharp the edges of the tumor are (*i.e.,* how

steep the line profile is). The line profiles are used to measure the size of the tumor is at intensity thresholds of -700 HU and -500 HU (often used for contouring of lung tumors in patients). Finally, a qualitative comparison of the images is enough to see any obvious improvements or problems with the deblurred images.

4.4. Results

4.4.1. Digital phantom results

Figure 4.1 and Table 4.1 show results of the deblurring algorithm as applied to the time averaged NCAT volume. Sagittal, coronal, and axial slices which intersect the center of the tumor are shown for the time averaged (left), stationary (middle) and deblurred (right) volumes. Below the images for each volume are shown line profiles measured along the SI (blue) AP (red) and LR (green) directions through the center of the tumor. The corresponding colored lines in the images show the positions of the line profiles.

The $NMSE$ between the stationary and deblurred images is 0.1255, which is a significant improvement over the $NMSE$ between the stationary and time averaged images, 0.2897. If simple thresholds are applied to the image at -700 HU (*i.e.,* tissue somewhat denser than air, but less dense than water), the SI dimension of the tumor (a 1.8 cm sphere) would be measured as 2.8 cm in the time averaged image, 1.8 cm in the stationary image, and 1.9 cm in the

deblurred image. Measurements along the AP axis give 1.1 cm in the time averaged image, 2.2 cm in the stationary image, and 2.2 in the deblurred image. Measurements along the LR axis give 1.2 cm in the motion averaged image, 1.8 cm in the stationary image, and 1.9 cm in the deblurred image. A threshold of -500 HU would result in detection of no tumor in the time averaged image, measurements of 1.8 cm SI by 2.1 cm AP by 1.8 cm LR in the stationary image, and measurements of 1.8 cm by 2.1 cm by 1.8 cm in the deblurred image. The measured tumor size is less dependent on the choice of threshold for the stationary and deblurred images because the line profiles are steeper near the tumor boundaries. Not only does the time averaging effect blur the edges of the tumor, it also lowers the HU of the tumor enough that no part of the tumor is visible at a threshold of -500 HU. The error in the measured AP length of the tumor in the stationary and deblurred images is caused by the vascular structure located directly anterior to the tumor. Qualitatively, the deblurred image is an obvious improvement over the heavily blurred time averaged image when each is compared to the stationary image. The deblurred image is not as sharp as the stationary image, and some artifacts are present, for example at the interface of the tumor and the adjacent vascular structure.
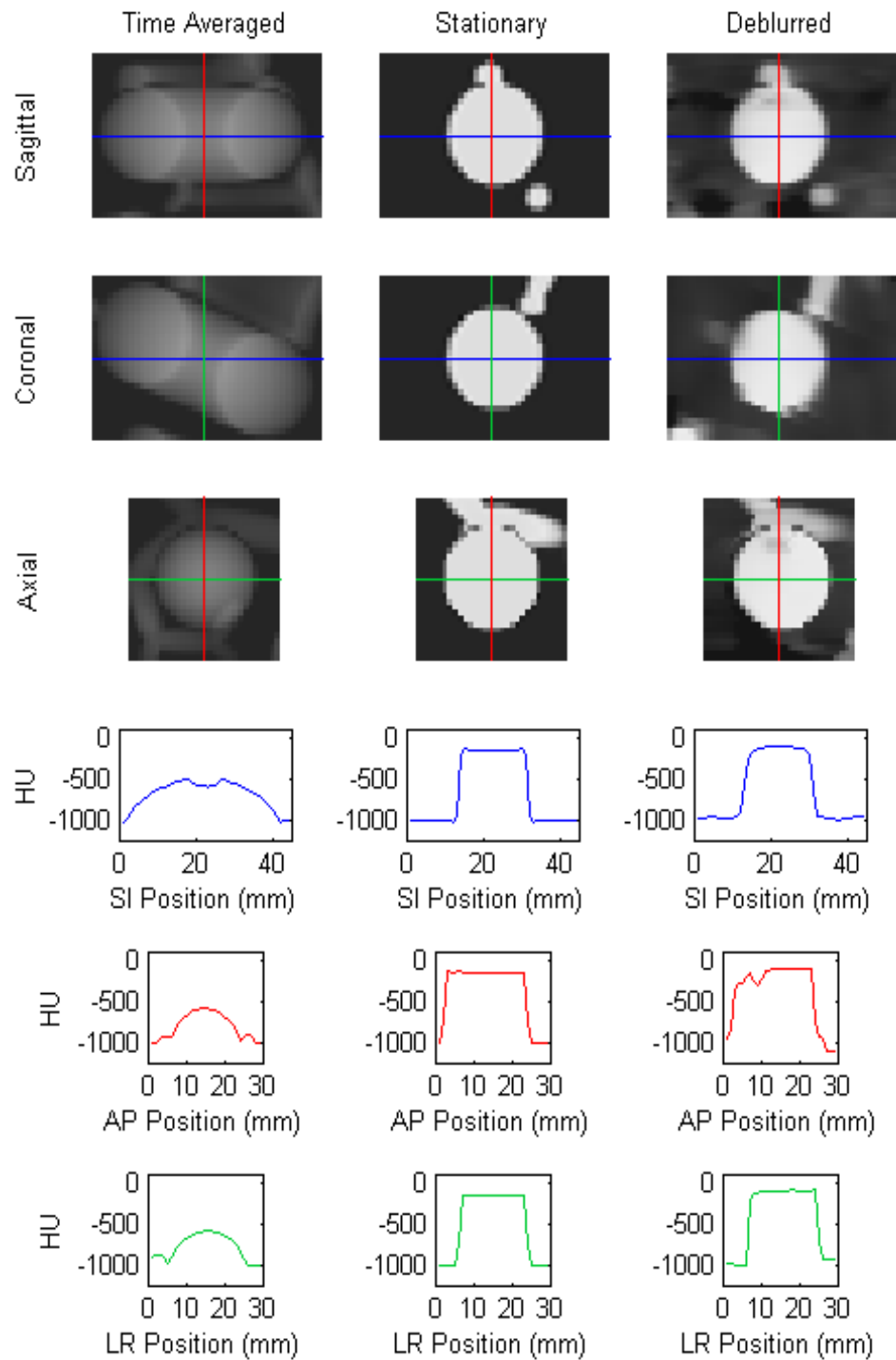
Figure 4.2: Deblurring results for the NCAT phantom. Slices through the center of the tumor for time averaged (left), stationary (middle), and deblurred (right) volumes are shown, with corresponding line profiles along the SI (blue), AP (red) and LR (green) axes. The colored lines in the slices show the position of each line profile.

Table 4.1: A table of NCAT phantom results including the *NMSE* of each volume relative to the stationary image, and the size of the tumor along the SI, AP, and LR axes, as determined by application of -700 HU and -500 thresholds to each image.

	Time Averaged -700/-500 HU	Stationary -700/-500 HU	Deblurred -700/-500 HU
SI (cm)	2.8/0	1.8/1.8	1.9/1.8
AP (cm)	1.1/0	2.2/2.1	2.2/2.1
LR (cm)	1.2/0	1.8/1.8	1.9/1.8
NMSE	0.2897	0	0.1255

4.4.2. Physical phantom results

Figure 4.3 and Table 4.2 show results of the deblurring algorithm as applied to the CBCT of the moving phantom. Sagittal, coronal, and axial slices which intersect the center of the tumor are shown for the moving CBCT (left), stationary CBCT (middle) and deblurred CBCT (right) volumes. Below the images line profiles measured along the SI (blue) AP (red) and LR (green) directions through the center of the tumor are plotted. The corresponding colored lines in the images show the positions of the line profiles.

The *NMSE* was 0.1179 when comparing the stationary CBCT to the moving CBCT, but was reduced to 0.0714 when comparing the deblurred CBCT to the stationary CBCT. At a thresholds of (-700/-500) HU, the SI dimension of the tumor was measured as (3.4/2.5) cm in the moving CBCT, (2.7/2.5) cm in the stationary CBCT, and (2.7/2.5) cm in the deblurred CBCT. Measurements along the AP axis give (2.5/2.3) cm, (2.6/2.5) cm, and (2.5/2.4) cm in the moving, stationary, and deblurred CBCT respectively.

Measurements along the LR axis give (2.6/2.5) cm, (2.9/2.8) cm, and (2.9/2.7) cm in the moving, stationary, and deblurred CBCT respectively. Figure 4.3 shows how blurring along the target's trajectory causes the SI dimension of the tumor to be overestimated in the moving CBCT, while the AP and LR dimensions are slightly underestimated. The correct measurement of the SI tumor size at a threshold of -500 HU in the moving CBCT could be considered somewhat a matter of luck, as the slope of the line profile is shallow at this point, and a small change in the threshold value would alter the determined tumor size significantly. Measurements of the tumor size in the stationary or deblurred images on the other hand are accurate at either threshold value, as steeper line profiles and correspondingly more clearly defined edges are present. Qualitatively, the deblurred CBCT shows an excellent match to the stationary CBCT, and is a large improvement over the moving CBCT.

Figure 4.3: Deblurring results for the physical phantom. Slices through the center of the tumor for moving (left), stationary (middle), and deblurred (right) CBCTs are shown, with corresponding line profiles along the SI (blue), AP (red) and LR (green) axes. The colored lines in the slices show the position of each line profile.
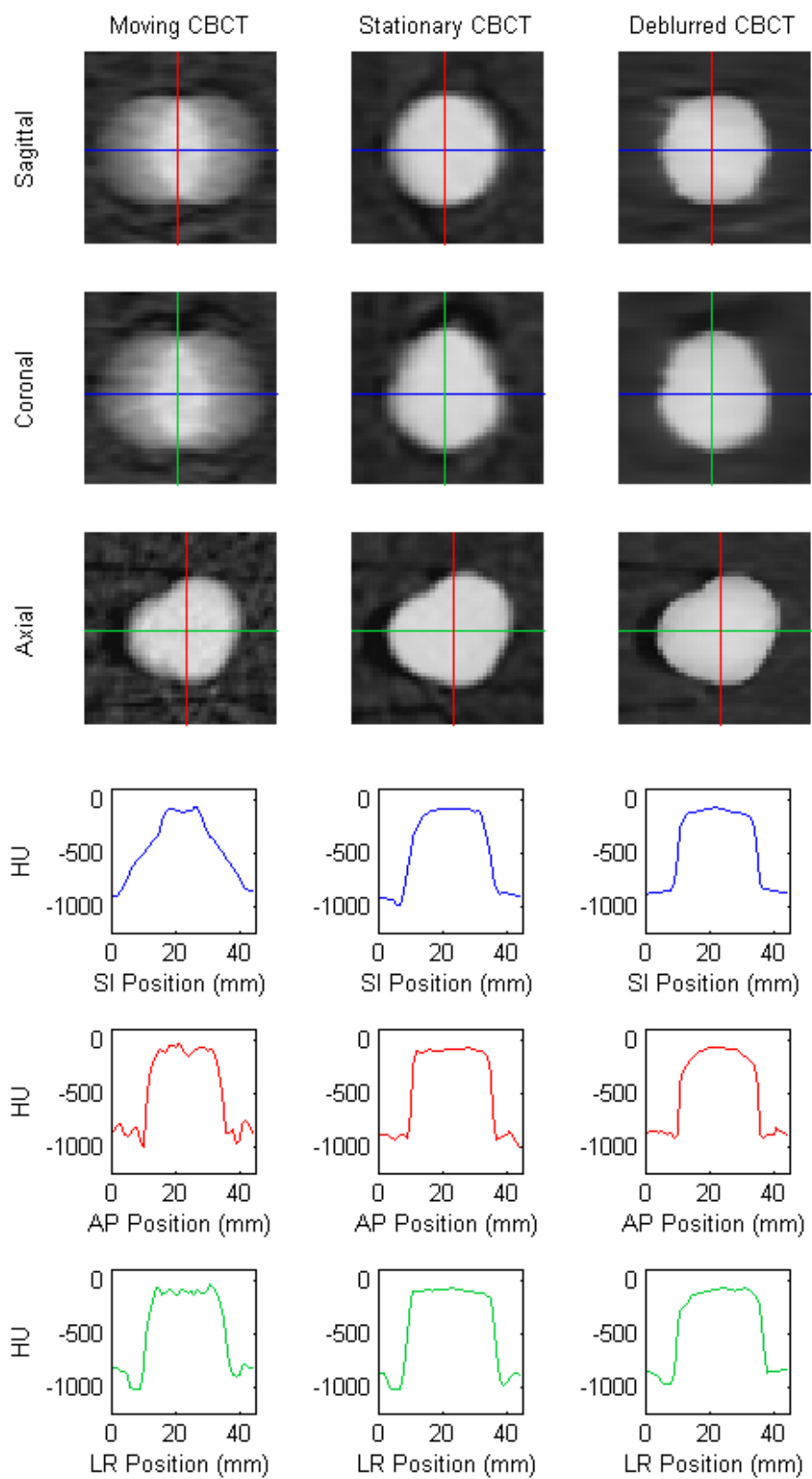
Table 4.2: A table of physical phantom results, including the *NMSE* of each volume relative to the stationary CBCT, and the size of the tumor along the SI, AP, and LR axes, as determined by application of a (-700/-500) HU threshold to each CBCT.

	Moving CBCT -700/-500 HU	Stationary CBCT -700/-500 HU	Deblurred CBCT -700/-500 HU
SI (cm)	3.4/2.5	2.7/2.5	2.7/2.5
AP (cm)	2.5/2.3	2.6/2.5	2.5/2.4
LR (cm)	2.6/2.5	2.9/2.8	2.9/2.7
NMSE	0.1179	0	0.0714

4.4.3. Patient results

Figure 4.4 and Table 4.3 show results of the deblurring algorithm as applied to the CBCT acquired immediately prior to treatment. Sagittal, coronal, and axial slices which intersect the center of the tumor are shown for the CBCT (left), 4DCT (middle) and deblurred CBCT (right) volumes. Below the images line profiles measured along the SI (blue) AP (red) and LR (green) directions through the center of the tumor are plotted. The corresponding colored lines in the images show the positions of the line profiles. The 4DCT is used as a "ground truth" reference in this case. However, the 4DCT was acquired weeks prior to simulation, is subject to its own artifacts, and may not accurately reflect the tumor's form at the time the CBCT was acquired.

The *NMSE* was 0.2929 when comparing the CBCT to the 4DCT, but was reduced to 0.1909 when comparing the deblurred image to the 4DCT. At a thresholds of (-700/-500) HU the SI dimension of the tumor was measured as (4.1/3.1) cm in the CBCT, (2.0/1.6) cm in the 4DCT, and (2.2/1.7) cm in the deblurred image. Measurements along the AP axis give (1.8*/1.4) cm,

(1.8*/1.4) cm, and (1.8*/1.5) cm in the CBCT, 4DCT, and deblurred image respectively. Measurements along the LR axis give (1.1/1.0) cm, (1.2/1.1) cm, and (1.2/1.1) cm in the CBCT, 4DCT, and deblurred image respectively. Measurements along the LR axis are cut off on the right side of the VOI, where the tumor abuts with the spine. For AP measurements denoted with an *, the threshold of -700 HU is not reached along the line profile, and the full size of the VOI is reported. While a threshold of -700 HU would not generally be used in real patient data, results are reported for consistency with the phantom studies of this chapter. Inspection of the line profiles in Figure 4.4 shows that the intensity profiles are somewhat steeper near the edge of the tumor in the deblurred image than in the original CBCT, and that the tumor size matches roughly with that represented in 4DCT. Along the AP and LR axes, the size of the tumor appears to be correctly preserved, and the line profiles near the tumor edges are slightly steeper in the deblurred image as compared to the CBCT. Qualitatively, the size and shape of the tumor appears much clearer in the deblurred image than in the CBCT. However, the deblurred image is noticeably less sharp than the 4DCT, and some of the finer details or textures may not be represented.
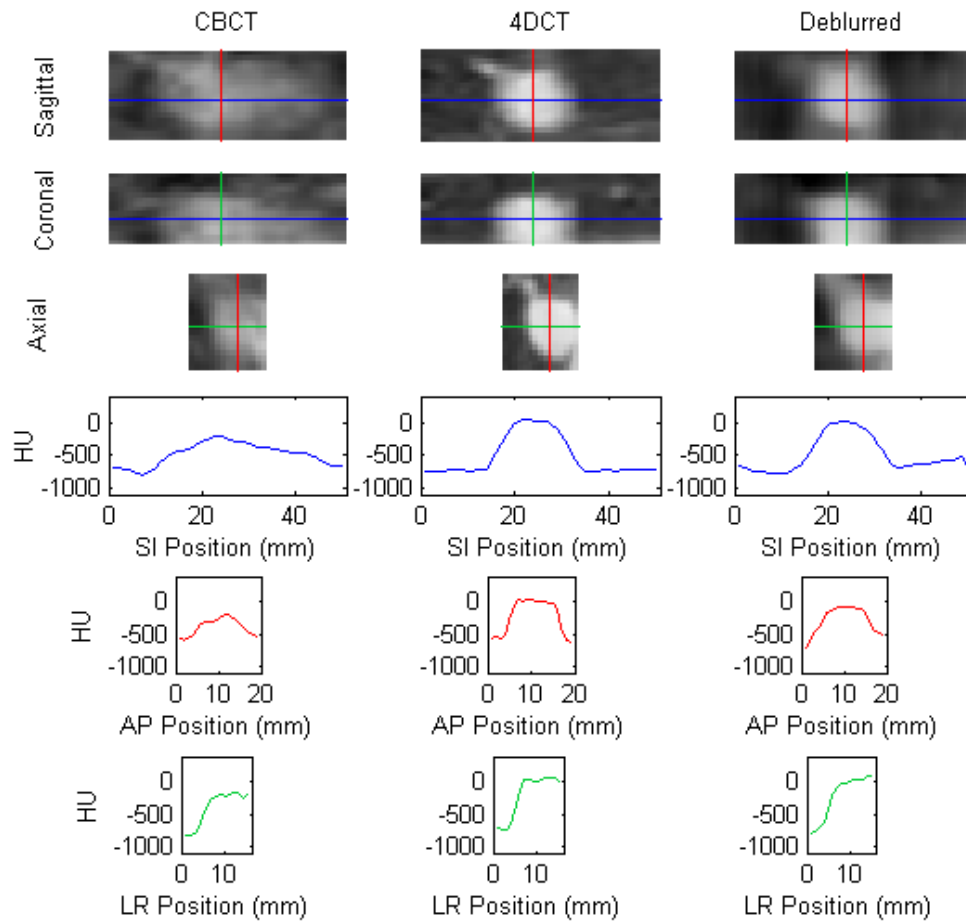
Figure 4.4: Deblurring results for the patient example. Slices through the center of the tumor for CBCT (left), 4DCT (middle), and deblurred (right) volumes are shown, with corresponding line profiles along the SI (blue), AP (red) and LR (green) axes. The colored lines in the slices show the position of each line profile.

Table 4.3: A table of example patient results, including the *NMSE* of each volume relative to the 4DCT, and the size of the tumor along the SI, AP, and LR axes, as determined by application of a (-700/-500) HU threshold to each CBCT.

	CBCT -700/-500 HU	4DCT -700/-500 HU	Deblurred -700/-500 HU
SI (cm)	4.1/3.1	2.0/1.6	2.2/1.7
AP (cm)	1.8*/1.4	1.8*/1.4	1.8*/1.5
LR (cm)	1.1/1.0	1.2/1.1	1.1/1.0
NMSE	0.2929	0	0.1909

4.5. Discussion

The preliminary results reported above show that a deblurring algorithm based on motion tracked *during* CBCT acquisition performed excellently when tested on digital and physical phantom studies. Deblurring also appeared to be effective on an example patient case, though the benefits were less stark than in the phantom cases. Possible sources of error and how they relate to the phantom and patient cases are discussed below, including; 1) the assumption that motion is rigid within the VOI being deblurred; 2) estimation of the motion PDF; 3) the validity of the model used for motion blurring artifacts (Equation 4.1); and 4) choice of regularization in the deconvolution algorithm.

A major advantage of this work is that it uses motion tracked *during* a CBCT scan. Previous works have relied on motion models generated from 4DCT to remove motion blurring artifacts from CBCT (Li *et al* 2006a, Rit *et al* 2009b). When motion changes significantly between 4DCT acquisition and treatment, this dependency may result in poor performance in artifact removal.

By tracking objects on the day of treatment, the method presented here ensures that the motion model is specific to the motion during the CBCT scan. The preliminary results reported above show that a deblurring algorithm based on motion tracked during CBCT acquisition performed excellently when tested on digital and physical phantom studies. Deblurring also appeared to be effective on an example patient case, though the benefits were less stark than in the phantom cases. Some possible sources of error are discussed below, including; 1) the assumption that motion is rigid within the VOI being deblurred; 2) estimation of the motion PDF; 3) the validity of the model used for motion blurring artifacts (Equation 1); and 4) choice of regularization in the deconvolution algorithm.

Since the motion of only one point (the tumor centroid) is tracked, the region over which the "motion model" is accurate is small. The deblurring technique can only be applied to a small VOI near the tracked object, where points inside the VOI can be assumed to move rigidly with the tracked point. If points within the VOI move differently than the tracked object, the algorithm will perform poorly. Larger tumors or any tumor that deforms substantially during the respiratory cycle could pose a problem. In the future, this challenge might be addressed by tracking multiple points, or by combining the tracked motion with previous motion information from 4DCT to generate a motion model for the entire reconstruction volume (though the reliance on a previous motion model should be minimized). As an alternative to the post-processing

approach of this paper, a complete motion model such as this could be incorporated into the reconstruction algorithm (Li *et al* 2006a, Rit *et al* 2009b).

Accurate estimation of a tumor's motion PDF during the CBCT scan is critical to the performance of the deblurring algorithm. The first requirement for PDF estimation is reliable knowledge of the tumor's position. Methods of tumor tracking are discussed in detail in Chapters 1 and 2, with their associated benefits and disadvantages. Tracking results from a CBCT scan would come in the form of a set of 2D tracking results corresponding to the rotational x-ray projections. The methods of this dissertation rely on the assumption of a regular, periodic orbit to reconstruct a closed 3D trajectory from these 2D tracking results, which is in turn used to estimate the motion PDF. If the trajectory is irregular or aperiodic, neither the trajectory nor the corresponding motion PDF will be useful. A somewhat irregular breathing pattern is likely part of the reason that the deblurring results are not as good in the patient data as they are for phantom data.

Other methods of estimating the motion PDF are possible when the assumption of periodic motion is unacceptable. Recently Poulsen *et al* reconstructed motion PDFs from tracking results based on implanted fiducial markers in lung and prostate patients (Poulsen *et al* 2008). Maximum likelihood estimation (MLE) was used to fit a 3D Gaussian PDF based on sets of tracking results acquired in 60 second intervals (corresponding to the approximate time of a regular CBCT scan). This method of PDF estimation

works well when the PDF can be accurately represented by a 3D Gaussian, and is appealing in that in can be applied to targets that exhibit aperiodic motion, such as the prostate. However, in some cases a motion PDF cannot be well modeled by a single 3D Gaussian. For example, a Gaussian would not be a good choice to model a lung tumor trajectory which is completely regular but exhibits some hysteresis (*e.g.,* a circular orbit). Additionally, as discussed in the following paragraph, the deblurring model used in this work may not be applicable when regular periodic motion can not be assumed.

The deblurring algorithm relies on the assumption the model used to describe the creation of motion artifacts in a CBCT volume (Equation 4.1) is appropriate. For a simple time averaged volume, such as the one used in the digital phantom study, the model is clearly valid. For reconstructed CBCT data, the model is also reasonable if the period of a tumor's trajectory is small compared to the gantry rotation time of a CBCT scan (as is the case for lung tumors). Previous work has verified that lung tumors appear spread out over their trajectory in CBCT volumes, and the effect is easily seen in the physical phantom and patient results shown in Section 4.4 (Wang *et al* 2007). The effects of slower (roughly similar to the gantry rotation speed) or aperiodic tumor motion may not be well represented by this simple model because of the more complicated artifacts caused by the interplay of gantry and tumor positions. The success of the algorithm in deblurring the CBCT of the physical phantom suggests that the model is well suited for typical CBCT acquisition

parameters and regular periodic motion similar to what might be expected from a lung tumor.

TV norm was chosen as the regularization term for the cost function in Equation 4.2, but many other regularization terms are possible. The choice of regularization essentially corresponds to incorporation of prior knowledge in the deconvolution algorithm. TV norm regularization assumes that the signal being recovered is piecewise constant. This is a good assumption for lung tumors, where the tumor with approximately constant high density is embedded in lower density lung tissue. TV norm regularization may cause the variations across the tumor or within the lung to be lost, but this is usually not a significant concern since for most practical purposes it is the ability to distinguish between tumor and regular lung tissue that is important. Other forms of edge preserving regularization have been developed which may be better suited for anatomical regions or purposes where it is more important to preserve textures and details. Some examples include neighborhood filters (*e.g.,* bilateral filter, penalty weighted least square, etc.,) and non local means algorithms (Smith and Brady 1997, Buades *et al* 2005, Liu *et al* 2008, Wang *et al* 2009). While these regularization methods may preserve more fine structure than TV norm regularization, they are much more computationally expensive, and would not necessarily improve the ability to determine the shape and size of a lung tumor.

4.6. Conclusion

An algorithm has been developed which removes motion artifacts from CBCT volumes based on tracked object motion in the cone-beam projections used for reconstruction. The procedure was demonstrated to work well for digital and physical phantom studies, and appeared to decrease motion artifacts in patient CBCT. The major advantage of this method is that it relies on information about the motion of the patient acquired in the same projections used for CBCT reconstruction. A drawback is that only one point (a tumor centroid) is tracked, thus the motion correction only works over a small volume which moves similarly to the tracked point. In the future, multiple objects or points may be tracked in order to provide motion information over a larger reconstruction volume.

This chapter contains material being prepared for publication. Lewis, John H.; Li, Ruijiang; Jia, Xun; Watkins, W. Tyler; Song, William Y.; Jiang, Steve B. The dissertation author was the primary investigator and author of this material.

5. Diaphragm-Based Tumor Tracking

5.1. Overview

The importance of accurate knowledge of a tumor's position in modern, highly conformal radiation therapy is well known and has been discussed in detail in the preceding chapters of this dissertation. Methods for tumor tracking can be separated intro three basic categories, each of which has its own benefits and problems.

The first method is direct tumor tracking, which has been the primary focus of this dissertation. In direct tumor tracking, the tumor is localized based on its appearance in fluoroscopic x-ray images. Direct tumor tracking is appealing because there is no requirement for marker implantation and because tracking does not rely on the relationship between the tumor position and the position of a surrogate (implanted or anatomical). The major drawback of direct tumor tracking is the difficulty in automatically detecting the tumor in x-ray images. Tumors appear in many different shapes, sizes, and positions in

the lung, and sometimes have no clear border or texture visible in x-ray images. While a great deal of work has gone into direct or markerless tumor tracking (including Chapter 2 of this dissertation), these challenges have thus far prevented a tracking algorithm from being developed which is reliable enough for common clinical use (Cui *et al* 2007a, Xu *et al* 2008, Lewis *et al* 2009, Li *et al* 2009b, Lin *et al* 2009b).

A second method is tracking based on implanted artificial surrogates, such as gold fiducial markers or wireless transponders (Seiler *et al* 2000, Balter *et al* 2005). An implanted marker is by design easy to track accurately. However, markers may sometimes migrate within the body (Nelson *et al* 2007). Marker migration can lead to poor tumor tracking due to the changing relationship between the marker and tumor positions. Additionally, there are risks of complications associated with marker implantation into lung tumors, including the potential for pneumothorax (Arslan *et al* 2002, Geraghty *et al* 2003). These drawbacks have prevented the use of implanted markers for lung tumor localization in many institutions.

Thirdly, tumor tracking can be performed based on anatomical surrogates. Common surrogate choices include the chest wall, abdomen, carina, or diaphragm. An obvious advantage of anatomical surrogates is that no invasive marker-implantation procedure is required. Additionally, chosen surrogates are generally easily tracked, either by external cameras (*e.g.,* abdomen surface) or in x-ray images (*e.g.,* diaphragm). The major difficulty

with this type of tracking is the development of a stable and reliable model to relate the position of the surrogate to the position of the tumor.

The most commonly used anatomic surrogate is the abdominal surface (Jiang 2006, Kanoulas *et al* 2007, Ruan *et al* 2008, Wu *et al* 2008a). Some forms of external surrogate-based tracking have already attained widespread clinical use, such as the Real-time Position Management (RPM) system for gated radiation therapy or 4DCT sorting (Varian Medical Systems, Inc, Palo Alto, CA) (Jiang 2006). This system uses infrared cameras to track the AP motion of a marker block placed on a patient's abdomen, and relies on a consistent correlation between the block's motion and the tumor's position. Unfortunately it has been shown in multiple studies that the relationship between abdominal motion and lung tumor position can change, both between and during treatments (Bruce 1996, Hoisak *et al* 2004, Tsunashima *et al* 2004). The use of the abdomen as a surrogate during gated radiation therapy can result in large residual tumor motion with the gating window, and frequent target misses (Berbeco *et al* 2005b, Berbeco *et al* 2006, Wu *et al* 2008a). It may be possible to improve accuracy by repeatedly updating the correlation model between the external surrogate and the internal tumor, or through breathing coaching methods (Jiang 2006, Kanoulas *et al* 2007, Wu *et al* 2008a).

A more intuitively appealing solution is to use an internal surrogate such as the diaphragm or carina for tumor tracking. These objects should have a

simpler and more stable relationship with the tumor position. A previous study based on 4DCT showed the carina to be a good surrogate for lung tumor motion, and suggested that it is in fact superior to the diaphragm (van der Weide *et al* 2008). However, this study did not account for a phase shift between the tumor and the diaphragm position. A similar study showed that when a possible phase shift between the diaphragm and tumor motions is accounted for, the diaphragm performs well as a surrogate (Zhang *et al* 2007). The usefulness of the diaphragm as a surrogate for lung tumor motion has since been corroborated by a more comprehensive study in fluoroscopic image sequences (Cervino *et al* 2009). The diaphragm is a particularly appealing surrogate for use with x-ray projections because of its high visibility in the projections. It has been shown to be tracked easily in fluoroscopic images from a fixed angle (Chen *et al* 2001, Vedam *et al* 2003b, Berbeco *et al* 2005a). Retrospective diaphragm tracking in MV CBCT projections has also been successfully performed (Alfredo 2009).

While the diaphragm may perform well as a surrogate for tumor motion in most cases, the relationship between diaphragm and tumor positions will not always remain stable over time. Figure 5.1 shows an example of two fluoroscopic images acquired of at different times during the same treatment session. These images were both acquired at approximately the same phase in the breathing cycle, and with the diaphragm at the same position (as shown by the dotted line). The tumor, marked with a solid black circle, has a

dramatically different position in the two images. Current linear models used to relate tumor and diaphragm positions would not be able to accurately account for this type of discrepancy (Cervino *et al* 2009). It is possible that a more complicated non linear model could account for this type of motion. However, the fundamental problem is that correlation models are based on previous knowledge of the two object's motion (*i.e.,* training data). If the objects move in a way that is not represented in the training data, the model will likely be unable to predict the correct relationship.

In this chapter, a combined tracking method is developed which incorporates both direct and diaphragm-based lung tumor tracking. Direct tumor tracking results are relied on when a tumor is relatively clearly visible in projection images and good accuracy can be expected, while diaphragm tracking is resorted to when direct tracking results are deemed unreliable. The methods by which this distinction is made, and the way in which diaphragm tracking is performed are outlined in the following section.
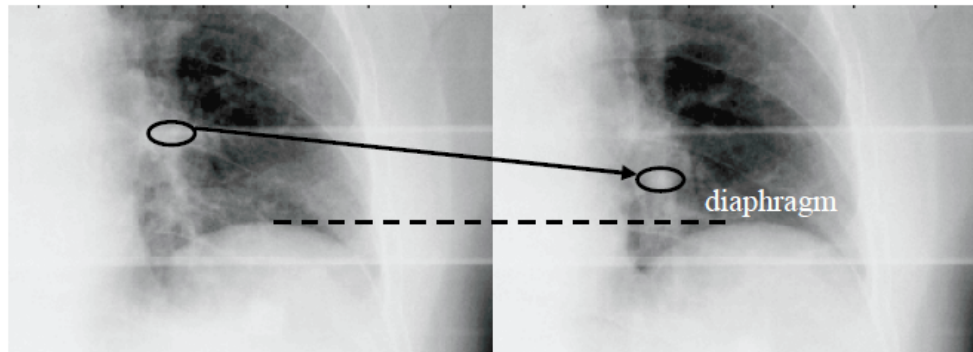
Figure 5.1: Two images from a fluoroscopic sequence acquired during the same treatment. The two images are acquired at approximately the same phase, with the apex of the diaphragm (dotted line) in the same position. The tumor (black circle) is not in the same position.

5.2. Methods

5.2.1. Combined tracking

Direct tumor tracking has been shown to be capable of accurately tracking a tumor in fluoroscopic image sequences taken from the AP direction when the tumor is somewhat easily visible (Cui *et al* 2007a, Xu *et al* 2008). Unfortunately, the same success has not been achieved in lateral images or in images where the tumor is difficult to see. In the case of tracking in rotational projections, there should nearly always been some angles at which the tumor is difficult to see due to intervening objects such as the spine. Figure 5.3 shows the axial tracking results for the second patient in Chapter 2. Arrow (a) points to a tracked position within a region of relatively good tracking accuracy, while arrow (b) points to a position surrounded by relatively bad tracking

results. The corresponding projection images are shown below. In image (a), the tumor is clearly visible. In image (b), corresponding to the bad tracking result, the tumor is behind the spine and is nearly impossible to see. It is not surprising that an automatic tracking algorithm dependent on image information has a relatively easy time tracking a clearly visible object, but trouble when the object is barely distinguishable. A robust markerless tracking algorithm applicable to rotational projection images must have some way of handling this problem.

A practical solution is to implement a combined tracking algorithm which uses surrogate-based tracking for the angles at which the tumor is difficult to track directly. Even at angles where the tumor is difficult to see, a surrogate such as the diaphragm has enough contrast to be clearly visible in the projection image (see Figure 5.3). While reliance on a correlation model between the diaphragm and the tumor is not ideal, it may be less of a problem than attempting to track an object which is practically invisible in the projection image.

A key element to a combined tracking approach is the determination of when a switch from direct tumor tracking to diaphragm-based tracking should occur. As stated above, the angles for which a lung tumor is difficult to see often are the angles for which it overlaps with the spine or other relatively dense structures. The solution presented here is to determine the angles at

which this overlapping is expected, and to rely on diaphragm tracking for those angles.

Using the methods described in Chapter 2, DRRs generated from 4DCT phases are used for direct tumor tracking. In addition to contouring the VOI surrounding the lung tumor's range of motion, another "avoidance" VOI is now contoured surrounding the spine and other high density structures near the posterior center of the thorax. An example of contoured VOIs is shown in Figure 5.4. When DRRs are created, in addition to projection the tumor VOI onto the imager, the avoidance VOI is also projected using the same geometry. If the projected VOIs overlap in the image, the tumor is assumed to be difficult to track, and diaphragm-based tracking is used. If the two areas do not overlap, direct tumor tracking is used (avoiding the dependence on a diaphragm-tumor model).
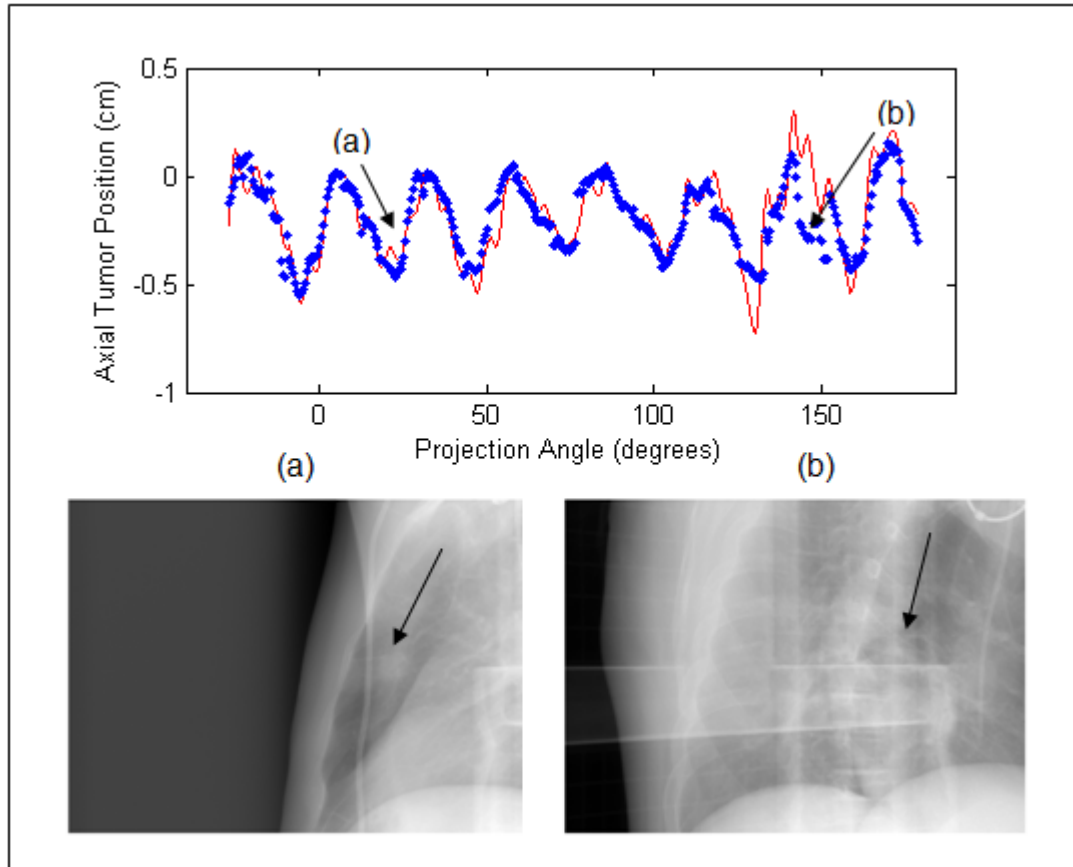
Figure 5.2: The tracking results for patient 2 are shown above, with arrows pointing out two specific tracking results. The projection image corresponding to the good tracking results at point (a) is shown on the left, while the image corresponding to the poor tracking result at point (b) is shown on the right.

Figure 5.3: Tumor VOI (red lines), tumor contour (yellow) and "avoidance" VOI (magenta) shown for an example patient case.

5.2.2. Diaphragm-based tracking

The first step in building a diaphragm-based tracking algorithm is to construct a model relating tumor and diaphragm positions. It has been shown that a simple linear model can be used to accurately model the relationship (Cervino *et al* 2009). A similar model is used in this work:

$$y = a + \sum_{i}^{N} b_i x_i,$$

(5.1)

where x_i is the position of the diaphragm at series of time points indexed by i, b_i and a are parameters fit to the training data, N is the number of previous diaphragm positions incorporated into the model, and y is the tumor position. If N is chosen as 1, then the tumor position depends only on the diaphragm position at the same time instant, and no phase shifts are possible. In order to account for a possible phase shift between diaphragm and tumor motion, N is chosen as 2 for this study. The model was fit using least squares based on the diaphragm apex and tumor positions derived from 4DCT. It has been shown in previous work that a diaphragm-tumor motion model derived during treatment simulation can be employed during later treatment sessions (Cervino *et al*). While the model could be used for tracking in multiple dimensions, we examine only the SI diaphragm and tumor positions in this preliminary study.

Diaphragm tracking in the rotational projections was performed using the template matching algorithm described in Chapter 2. Deformations of the diaphragm surface make tracking based on shifting of fixed templates impractical if applied to a large VOI encompassing the entire surface. Additionally, the diaphragm apex position was used to derive the relationship with the tumor position, and this relationship may change for different regions of the diaphragm. For these reasons, only a narrow VOI around the apex of the diaphragm was used. An example image with projected VOI overlaid is shown in Figure 5.4. The resulting tracked SI motion of the diaphragm apex was input to the correlation model to determine the tumor position. Since the

model is defined in the 3D patient coordinate system, the parameters in Equation 5.1 must be appropriately scaled for application in the imager plane. Similarly to Chapter 2, this scaling was performed based on the source to apex and apex to imager distances as estimated from 4DCT.

The diaphragm apex was chosen as a reference point because it should remain at or close to the diaphragm-lung interface for all projection images. If a point on the diaphragm surface lower than the apex was selected, there would be some angles for which the point was not along the visible interface in the image, and the position of the point could not be detected. Depending upon the curvature of the diaphragm and the relative positions of the source, isocenter, and image detector, even the 3D diaphragm apex may not appear as the highest position of the diaphragm in the 2D projection images or DRR templates. Given the convexity of a diaphragm, and the relatively large source to isocenter distance (100 cm) the apparent apex in the 2D image should represent a point close to the true 3D apex. For this work, we assume that the model derived relating the SI diaphragm apex position to the tumor position is also valid for points near the apex.
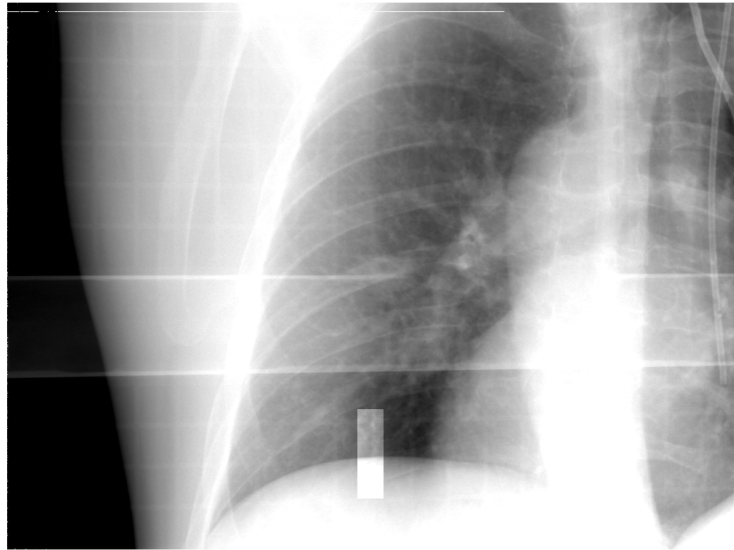
Figure 5.4: An example patient projection, with the projected narrow VOI shown near the apex of the diaphragm.

5.3. Materials

5.3.1. Digital NCAT phantom data

Diaphragm-based and combined tracking were initially tested on the digital NCAT phantom. The NCAT phantom is described in Chapter 2, along with the methods used to simulate projections and templates. The phantom was programmed with 4 second period, 2.3 cm SI tumor amplitude, 0.9 cm AP amplitude, and 0.2 cm left-right (LR) amplitude. Images were simulated at 1 degree intervals over a 360 degree arc, with a gantry rotation time of 61.2 s. The 1.8 cm diameter tumor was positioned in the middle of the right lung. SI tumor and diaphragm apex positions used to fit the model in Equation 5.1

were derived from the same 10-frame dataset used to simulate 4DCT in Chapter 2.

5.3.2. Patient data

The algorithm was also tested on two patients from Chapter 2. The first patient was excluded because the tumor was located on top of the diaphragm apex. In patient 1 (corresponding to patient 2 of Chapter 2) the tracked tumor was located near the center of the left lung. From 4DCT the tumor diameter was estimated as 1.2 cm, with a 2.7 second breathing period and 0.5 cm, 0.3 cm, 0.4 cm amplitudes in the SI, AP, and LR directions respectively. In patient 2 (corresponding to patient 3 in Chapter 2) the tumor was located near the spine in the lower right lung. From 4DCT the tumor diameter was estimated as 1.6 cm, with a 3.0 second breathing period and 1.9 cm, 0.1 cm, and 0.1 cm amplitudes in the SI, AP, and LR directions respectively. The CBCT and 4DCT acquisition protocols are discussed in Chapter 2.

5.4. Results

5.4.1. Digital NCAT phantom results

Tracking results for the digital NCAT phantom are shown in Figure 5.5. Blue dots represent the direct tracking results, the red line is the true tumor

position, and the green dots are the diaphragm tracking results. The tumor positions have been scaled back to the average tumor position using the same procedure described in Chapter 2. The grey region in the graph denotes the angles for which the projected tumor ROI overlaps with the projected "avoidance" ROI, and the combined tracking algorithm switches from direct tracking to diaphragm-based tracking. Since projections span an entire 360 degrees, there are two regions where the tumor and spine overlap.

Cubic splines were fit to the 10 SI tumor and diaphragm apex positions from simulated 4DCT, and the time step (*i.e.,* the time lag between x_1 and x_2) in Equation 5.1 was selected as 0.68s, corresponding to a lag of 4 projections (and 17% of a breathing cycle). The determined coefficients for Equation 5.1 were $b_1 = 0.81$, $b_2 = -0.01$, and $a = 6.26$. The small value for b_2 is expected because there is a simple linear relationship and no phase shift between the diaphragm and the tumor in the respiratory motion model of the NCAT phantom.

Tracking errors are reported for the digital phantom in Table 5.1. Results are reported in terms of the e_{95} and the e_{rms} for direct tracking (as described in Chapter 2), diaphragm based tracking (as described above in Section 5.2.2), and combined tracking. Combined tracking combines direct and diaphragm-based tracking using the technique described in Section 5.2.1. The e_{95} is 1.1 mm with direct tracking, 0.9 mm with diaphragm-based tracking, and 1.1 mm with combined tracking. Corresponding values of e_{rms} are 0.6 mm,

0.4 mm, and 0.6 mm for direct, diaphragm-based, and combined tracking respectively.
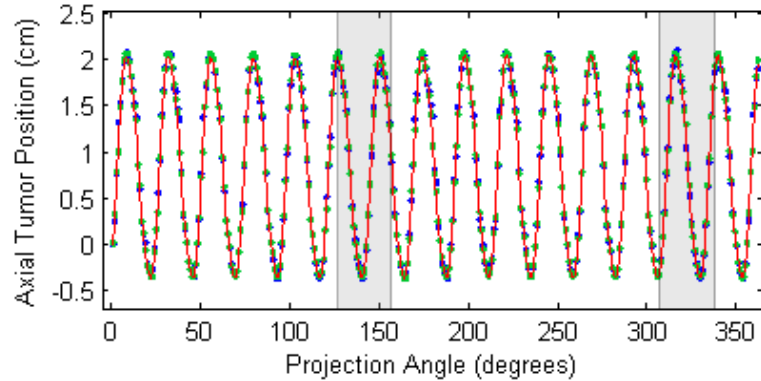
Figure 5.5: Diaphragm tracking results for the digital phantom. The red line is the true tumor position, the blue dots are the direct tracking results, and the green dots are from diaphragm-based tracking. The shaded grey area is the region in which diaphragm-based tracking would be used in a combined tracking scheme.

Table 5.1: Digital phantom tracking errors. Direct tracking (Chapter 2), diaphragm-based tracking (Section 5.2.2) and combined tracking (Section 5.2.1) results are reported.

	e95 (mm)	erms (mm)
Direct	1.1	0.6
Diaphragm	0.9	0.4
Combined	1.1	0.6

5.4.2. Patient results

Tracking results for patient 1 and patient 2 are shown in Figure 5.6 and Figure 5.7 respectively. Blue dots represent the direct tracking results, the red line is the clinician defined ground truth, and the green dots are the diaphragm tracking results. The tumor positions have been scaled back to the

approximate tumor position as estimated from 4DCT using the same procedure described in Chapter 2. The grey region in the graphs denote the angles for which the projected tumor ROI overlaps with the projected "avoidance" ROI, and the combined tracking algorithm switches from direct tracking to diaphragm-based tracking. In patient 1, the diaphragm tracking results are only available in a subset of angles where the diaphragm apex is visible in the projection images. In patient 1, the tumor is located farther from the spine, and the two do not overlap in most projections. In patient 2, the tumor is very close to the spine, and overlaps in about two thirds of the projections used.

Cubic splines were fit to the 10 SI tumor and diaphragm apex positions from 4DCT. The time step in Equation 5.1 was selected as 0.47s, corresponding to a lag of 5 projections (17% of breathing cycle in patient 1, 16% of breathing cycle in patient 2). The determined coefficients for Equation 5.1 were $b_1 = 0.41$, $b_2 = 0.24$, and $a = 6.90$ for patient 1, and $b_1 = 1.24$, $b_2 = -0.43$, and $a = 2.41$ for patient 2.

Tracking errors are reported for patients 1 and 2 in Table 5.2 and Table 5.3 respectively. Results are reported in terms of the e_{95} and the e_{rms} for direct tracking (as described in Chapter 2), diaphragm-based tracking (as described in Section 5.2.2), and combined tracking. Combined tracking combines direct and diaphragm based tracking using the technique described in Section 5.2.1. In patient 1, the e_{95} is 1.9 mm with direct tracking, 1.7 mm with diaphragm-

based tracking, and 1.7 mm with combined tracking. The corresponding e_{rms} values are 1.0 mm, 0.9 mm, and 0.8 mm for direct, diaphragm-based, and combined tracking respectively. In patient 1, the e_{95} is 4.6 mm with direct tracking, 3.0 mm with diaphragm-based tracking, and 2.9 mm with combined tracking. The corresponding e_{rms} values are 2.5 mm, 1.7 mm, and 1.6 mm for direct, diaphragm-based, and combined tracking respectively.
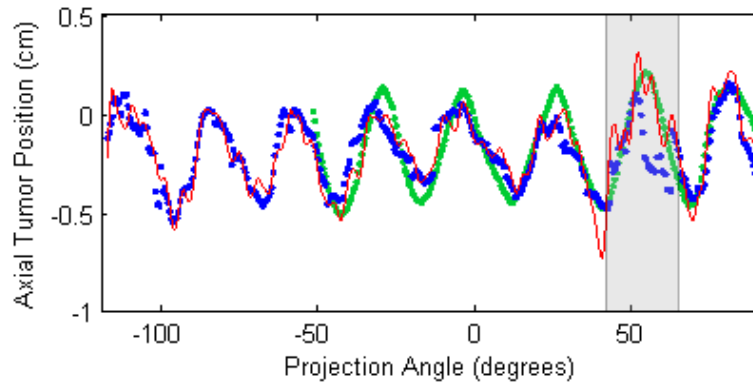
Figure 5.6: Diaphragm tracking results for patient 1. The red line is the clinician defined ground truth position, the blue dots are the direct tracking results, and the green dots are diaphragm-based tracking. The shaded grey area is the region in which diaphragm-based tracking would be used in a combined tracking scheme.

Table 5.2: Patient 1 tracking errors. Direct tracking (Chapter 2), diaphragm-based tracking (Section 5.2.2) and combined tracking (Section 5.2.1) results are reported.

	e95 (mm)	erms (mm)
Direct	1.9	1.0
Diaphragm	1.8	0.9
Combined	1.6	0.8
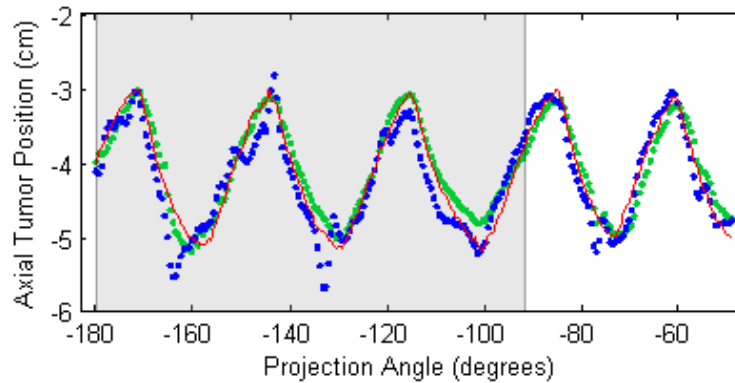
Figure 5.7: Diaphragm tracking results for patient 2. The red line is the clinician defined ground truth position, the blue dots are the direct tracking results, and the green dots are diaphragm-based tracking. The shaded grey area is the region in which diaphragm-based tracking would be used in a combined tracking scheme.

Table 5.3: Patient 2 tracking errors. Direct tracking (Chapter 2), diaphragm-based tracking (Section 5.2.2) and combined tracking (Section 5.2.1) results are reported.

	e95 (mm)	erms (mm)
Direct	4.6	2.5
Diaphragm	3.0	1.7
Combined	2.9	1.6

5.5. Discussion

In the digital phantom every tracking method performed well. Diaphragm-based tracking had slightly smaller errors than direct or combined tracking. This may have been due to the ease in tracking the high contrast diaphragm, and the simple, constant relationship between the diaphragm and tumor positions. Combined tracking does not offer much benefit in the

phantom case because the tumor is easily visible and tracked even when behind the spine. Reconstruction artifacts, imaging noise, and increased anatomic complexity make this a much more difficult task in patient data (along with 4DCT-CBCT registration errors, tissue deformations between 4DCT and CBCT acquisitions, and irregular breathing patterns).

In patient 1, direct tracking had the largest errors, and combined tracking had the smallest errors. However, the differences were very small. A difference of 0.1-0.2 mm is not clinically significant in most practical situations. Furthermore, given the inherent uncertainty in the clinician-defined ground truth, the small differences in performance may not constitute a real improvement. In patient 2, direct tracking had substantially larger errors than either diaphragm-based or combined tracking. Direct tracking was particularly poor for the large set of angles at which the tumor overlapped the spine in projection images. Combined tracking had slightly smaller errors than diaphragm-based tracking, but the difference was again very small.

While a conclusive comparative study would require more data, the results of this preliminary study demonstrate the feasibility of both diaphragm-based and combined tracking methods. In every case, both diaphragm-based and combined tracking performed equally or better than direct tracking alone. The results showed no clear advantage between combined and diaphragm-based tracking. However, as was discussed in Section 5.1 and illustrated in Figure 5.1, lung tumors can move in ways that are hard or impossible to

predict based on the diaphragm alone, or are not represented by the training data used to fit the diaphragm-tumor model. In these cases the model will be unable to accurately predict tumor motion, and diaphragm-based tracking will perform poorly. No such tumor motions were observed in the data used for this study, so the potential benefits of combined tracking were not demonstrated. Still, combined tracking reduced the time that the diaphragm-tumor model was relied upon (reducing the chance of failure) while maintaining comparably small errors to diaphragm-based tracking.

Imaging artifacts in 4DCT can lead to inaccurate diaphragm-tumor models. 4DCT are acquired slice by slice axially, so that the actual breathing cycle of the patient while a slice at the tumor is being acquired is a different cycle than when the diaphragm slice is acquired. These slices are usually binned into volumes based on phase, but if a patient breaths irregularly, the amplitude may be different for these two cycles. In this case, the diaphragm position would not correctly correspond to the tumor position. Nevertheless, diaphragm-tumor models based on 4DCT have been shown to be reliable in previous work (Zhang *et al* 2007, van der Weide *et al* 2008). Problems caused by irregular breathing could potentially be reduced by breathing coaching, or by using amplitude sorting instead of phase sorting. Amplitude sorting is however unpopular clinically because sampling issues lead to missing slices in reconstructed volumes.

The relationship between the diaphragm and tumor could change during the time between 4DCT acquisition and a treatment, reducing the accuracy of the model. Cerviño *et al* showed in a recently study of 21 fluoroscopic sequences acquired from five lung cancer patients that diaphragm-tumor models acquired during the first treatment could be used for accurate tracking in subsequent fluoroscopic sequences (2010). Registration based on bony anatomy was used to transfer the model to between sequences. Despite this study, it seems likely that there will be some instances in which models cannot be applied to multiple treatment days due to anatomical changes. For example, variable levels of matter in the gastrointestinal tract could cause a baseline shift in the diaphragm position. Unless the tumor exhibits the same magnitude baseline shift, the relative positions of the tumor and diaphragm would change.

Both the issues with 4DCT phase-binning errors and with applying a diaphragm-tumor model to subsequent treatment days could be addressed by training the model based on direct tumor tracking results on the day of treatment. In the methods of this chapter, both diaphragm and direct tumor tracking were performed at each angle. When the tracking results are reliable, these results could be used to establish or update the diaphragm-tumor model. As has been the major point of this chapter, direct tumor tracking is not always reliable. A potential solution to use the methods of Section 5.2.1 to determine when tracking results are reliable, and use those results to train the

diaphragm-tumor model. Then the model could be used at the angles for which direct tracking was deemed unreliable. In some cases a CBCT scan may start at an angle where direct tracking is unreliable, as was the case for example in the scan of patient 2. In these cases one would have to either resort to a model from a previous day, or to change the starting angle of the CBCT scan so that accurate direct tracking results are obtained before there is need to switch to diaphragm-based tracking.

This study was limited to only the SI motion of the diaphragm apex and tumor centroid positions. SI motion is generally the largest component of respiratory induced lung tumor motion, but smaller motions do occur in the AP and LR directions (Keall *et al* 2006). A model could be built relating the diaphragm's SI position to a tumor's LR and AP positions based on 4DCT. This extension of diaphragm-based tracking is planned for a future study.

5.6. Conclusion

A combined tracking algorithm was developed which incorporates benefits of both diaphragm-based and direct tumor tracking. The diaphragm apex was tracked using a slightly modified version of the method presented in Chapter 2. Diaphragm positions were then translated to tumor positions based on a simple linear model. By using the diaphragm as a surrogate, large tracking errors associated with angles for which the tumor is difficult to detect

in projection images can be reduced. By using direct tracking when the tumor is clearly visible in projection images, the time spent relying on the (potentially unstable) diaphragm-tumor model is minimized. In this preliminary study, the combined tracking algorithm performed better than or comparably to direct and diaphragm-based tracking in each case. Diaphragm-based tracking also performed well in each case. More data is required to investigate the performance of combined tracking in situations where diaphragm-based tracking may perform poorly. A larger comparative study should be performed before any decisive conclusions are drawn.

6. Conclusion

6.1. Summary and Conclusions

The goals of this dissertation were to develop a real-time localization algorithm that is applicable to rotational cone-beam projections, and to use tracking results from a set of projections acquired during a regular 3D CBCT scan to reconstruct a tumor's trajectory, size. The primary motivation for these goals was to make available more information about a lung tumor's motion and position to be available on the day of treatment, allowing for more accurate and precise radiation treatments. Such enhancements could potentially allow for decreased dose to normal tissues, or escalated dose to the tumor.

In Chapter 2 the algorithm for direct tumor tracking in rotational cone-beam projections was developed. Since tumors are tracked directly in projection images the algorithm does not require surgical implantation of fiducial markers, and does not rely on a stable relationship between the tumor and any surrogate. The feasibility of the algorithm was demonstrated on a digital phantom, a physical phantom, and three patients. While the patient

tracking results are promising, future refinement is needed to achieve more clinically palatable accuracy. A significant source of error appeared to be difficulty in tracking the tumor at angles where other high contrast objects overlapped with the tumor in the projection images. These errors were partially addressed by the diaphragm-based tracking work of Chapter 5.

In Chapter 3 a method was designed for using the rotational 2D tracking results of Chapter 2 to reconstruct 3D lung tumor trajectories. Accurate phase-binned trajectories were reconstructed in each case despite poor direct tracking results in some projection images. The most appealing aspect of this method is that 4D information can be acquired from the projections without the increased scanning time and dose associated with 4D CBCT. However, while the method presented here only provides a set of points representing the motion of the tumor centroid, a 4D CBCT allows for entire volumes to be reconstructed from which motion blurred artifacts have been removed. Depending on the application, knowledge of the tumor motion alone may be sufficient (*e.g.,* patient positioning), but in some cases it is desirable to know the shape and size of the tumor.

In Chapter 4 a method was developed to generate motion-corrected CBCTs of lung tumors using knowledge of a tumor's motion during CBCT acquisition as acquired by the techniques of Chapters 2 and 3 . The method was tested on digital phantom, physical phantom, and example patient cases. Motion blurring artifacts were effectively reduced in each case. While previous

motion-correction strategies relied on motion models derived from 4DCT acquired days or weeks prior to treatment, this method uses motion information acquired in the same dataset used for CBCT reconstruction. A drawback is that only one point (a tumor centroid) is tracked, thus the motion correction only works over a small volume which moves similarly to the tracked point.

In Chapter 5, a tracking algorithm was developed which incorporated benefits of both diaphragm-based and direct tumor tracking. By using the diaphragm as a surrogate, large tracking errors associated with angles for which the tumor is difficult to detect in projection images could be reduced. By using direct tracking when the tumor is clearly visible in projection images, the time spent relying on the (potentially unstable) diaphragm-tumor model is minimized. The method was tested on a digital phantom and two example patient cases. The combined tracking algorithm performed better than or comparably to direct and diaphragm-based tracking in each case. Diaphragm-based tracking also performed well in each case. More data is required to investigate the performance of combined tracking in situations where diaphragm-based tracking may perform poorly.

6.2. Future Work

The work of this dissertation has been limited to algorithm development and feasibility testing. A larger set of testing data is needed for a more comprehensive study of the methods presented in each chapter. A major challenge in patient data is the establishment of ground truth. In markerless tracking, the tumor position in each x-ray projection was defined manually. Since the tumor is hard to see in some projections, there is uncertainty in this definition of tumor position. A better future solution would be to use projection images of tumors with implanted fiducial markers. The markers could be used to establish ground truth, and then images could be processed to remove the markers before the markerless tracking algorithm is tested. Such data would only be available at an institution which uses fiducial markers and acquires CBCT for lung patients.

While the ultimate test of a tracking algorithm is its performance on real patient data, a more rigorous phantom study could also be helpful. In the future the NCAT phantom will be used to simulate more realistic data by adding noise, irregular breathing patterns, registration errors, and interfractional anatomic deformations. While it is not possible to reproduce all of the complexities and variations in real patient images, such a phantom study could be helpful in isolating and testing solutions to specific shortcomings of the tracking algorithms.

As was mentioned in Chapter 4, the motion-compensation algorithm presented is only applicable to a small volume near the tracked tumor. The size of the volume corresponds to the region for which rigid motion (corresponding to the tracked tumor centroid) is an accurate assumption. In future work, multiple targets will be tracked simultaneously so that motion blurring functions can be generated for specific regions of the thorax and motion artifacts can be removed from a larger volume.

References

Abdelnour A F, Nehmeh S A, Pan T, Humm J L, Vernon P, Schoder H, Rosenzweig K E, Mageras G S, Yorke E, Larson S M and Erdi Y E 2007 Phase and amplitude binning for 4D-CT imaging *Phys Med Biol* **52** 3515-29

Ablitt N A, Gao J X, Keegan J, Stegger L, Firmin D N and Yang G Z 2004 Predictive cardiac motion modeling and correction with partial least squares regression *Ieee Transactions on Medical Imaging* **23** 1315-24

Alfredo C S R 2009 Deriving motion from megavoltage localization cone beam computed tomography scans *Phys Med Biol* **54** 4195-212

Ancin H, Roysam B, Dufresne T E, Chestnut M M, Ridder G M, Szarowski D H and Turner J N 1996 Advances in automated 3-D image analysis of cell populations imaged by confocal microscopy *Cytometry* **25** 221-34

Arslan S, Yilmaz A, Bayramgurler B, Uzman O, Nver E and Akkaya E 2002 CT- guided transthoracic fine needle aspiration of pulmonary lesions: accuracy and complications in 294 patients *Med Sci Monit* **8** CR493-7

Atalar E and Onural L 1991 A respiratory motion artifact reduction method in magnetic resonance imaging of the chest *IEEE Trans Med Imaging* **10** 11-24

Balter J M, Ten Haken R K, Lawrence T S, Lam K L and Robertson J M 1996 Uncertainties in CT-based radiation therapy treatment planning associated with patient breathing *Int J Radiat Oncol Biol Phys* **36** 167-74

Balter J M, Wright J N, Newell L J, Friemel B, Dimmer S, Cheng Y, Wong J, Vertatschitsch E and Mate T P 2005 Accuracy of a wireless localization system for radiotherapy *Int J Radiat Oncol Biol Phys* **61** 933-7

Bedford J L 2009 Treatment planning for volumetric modulated arc therapy *Med Phys* **36** 5128-38

Bedford J L, Nordmark Hansen V, McNair H A, Aitken A H, Brock J E, Warrington A P and Brada M 2008 Treatment of lung cancer using volumetric modulated arc therapy and image guidance: a case study *Acta Oncol* **47** 1438-43

Berbeco R I, Mostafavi H, Sharp G C and Jiang S B 2005a Towards fluoroscopic respiratory gating for lung tumours without radiopaque markers *Phys Med Biol* **50** 4481-90

Berbeco R I, Nishioka S, Shirato H, Chen G T and Jiang S B 2005b Residual motion of lung tumours in gated radiotherapy with external respiratory surrogates *Phys Med Biol* **50** 3655-67

Berbeco R I, Nishioka S, Shirato H and Jiang S B 2006 Residual motion of lung tumors in end-of-inhale respiratory gated radiotherapy based on external surrogates *Med Phys* **33** 4149-56

Berson A M, Emery R, Rodriguez L, Richards G M, Ng T, Sanghavi S and Barsa J 2004 Clinical experience using respiratory gated radiation therapy: comparison of free-breathing and breath-hold techniques *Int J Radiat Oncol Biol Phys* **60** 419-26

Birchard K R, Hoang J K, Herndon J E, Jr. and Patz E F, Jr. 2009 Early changes in tumor size in patients treated for advanced stage nonsmall cell lung cancer do not correlate with survival *Cancer* **115** 581-6

Birkfellner W, Seemann R, Figl M, Hummel J, Ede C, Homolka P, Yang X, Niederer P and Bergmann H 2005 Fast DRR generation for 2D/3D registration *Med Image Comput Comput Assist Interv Int Conf Med Image Comput Comput Assist Interv* **8** 960-7

Blondel C, Malandain G, Vaillant R and Ayache N 2006 Reconstruction of coronary arteries from a single rotational X-ray projection sequence *Ieee Transactions on Medical Imaging* **25** 653-63

Bonnet S, Koenig A, Roux S, Hugonnard P, Guillemaud R and Grangeat P 2003 Dynamic X-ray computed tomography *Proceedings of the Ieee* **91** 1574-87

Bortfeld T, Jiang S B and Rietzel E 2004 Effects of motion on the total dose distribution *Semin Radiat Oncol* **14** 41-51

Bortfeld T, Jokivarsi K, Goitein M, Kung J and Jiang S B 2002 Effects of intra-fraction motion on IMRT dose delivery: statistical analysis and simulation *Phys Med Biol* **47** 2203-20

Bortfeld T and Paganetti H 2006 The biologic relevance of daily dose variations in adaptive treatment planning *Int J Radiat Oncol Biol Phys* **65** 899-906

Bruce E N 1996 Temporal variations in the pattern of breathing *J Appl Physiol* **80** 1079-87

Bruno R and Claret L 2009 On the use of change in tumor size to predict survival in clinical oncology studies: toward a new paradigm to design and evaluate phase II studies *Clin Pharmacol Ther* **86** 136-8

Buades A, Coll B and Morel J M 2005 A review of image denoising algorithms, with a new one *Multiscale Modeling & Simulation* **4** 490-530

Buhler P, Just U, Will E, Kotzerke J and van den Hoff J 2004 An accurate method for correction of head movement in PET *IEEE Trans Med Imaging* **23** 1176-85

Burnett S S, Sixel K E, Cheung P C and Hoisak J D 2008 A study of tumor motion management in the conformal radiotherapy of lung cancer *Radiother Oncol* **86** 77-85

Cai J F, Chan R H and Shen Z W 2008 A framelet-based image inpainting algorithm *Applied and Computational Harmonic Analysis* **24** 131-49

Caldwell C B, Mah K, Skinner M and Danjoux C E 2003 Can PET provide the 3D extent of tumor motion for individualized internal target volumes? A phantom study of the limitations of CT and the promise of PET *Int J Radiat Oncol Biol Phys* **55** 1381-93

Carasso A S 2006 APEX blind deconvolution of color Hubble space telescope imagery and other astronomical data *Optical Engineering* **45** -

Cervino L I, Chao A K, Sandhu A and Jiang S B 2009 The diaphragm as an anatomic surrogate for lung tumor motion *Phys Med Biol* **54** 3529-41

Cervino L I, Jiang Y, Sandhu A and Jiang S B Tumor motion prediction with the diaphragm as a surrogate: a feasibility study *Phys Med Biol* **55** N221-N9

Chan T C, Bortfeld T and Tsitsiklis J N 2006a A robust approach to IMRT optimization *Phys Med Biol* **51** 2567-83

Chan T F, Shen J and Zhou H M 2006b Total variation wavelet inpainting *Journal of Mathematical Imaging and Vision* **25** 107-25

Chen G T, Kung J H and Beaudette K P 2004 Artifacts in computed tomography scanning of moving objects *Semin Radiat Oncol* **14** 19-26

Chen Q S, Weinhous M S, Deibel F C, Ciezki J P and Macklis R M 2001 Fluoroscopic study of tumor motion due to breathing: facilitating precise radiation therapy for lung cancer patients *Med Phys* **28** 1850-6

Chetty I J, Rosu M, Tyagi N, Marsh L H, McShan D L, Balter J M, Fraass B A and Ten Haken R K 2003 A fluence convolution method to account for respiratory motion in three-dimensional dose calculations of the liver: a Monte Carlo study *Med Phys* **30** 1776-80

Cheung P C, Sixel K E, Tirona R and Ung Y C 2003 Reproducibility of lung tumor position and reduction of lung mass within the planning target volume using active breathing control (ABC) *Int J Radiat Oncol Biol Phys* **57** 1437-42

Choi N C and Doucette J A 1981 Improved survival of patients with unresectable non-small-cell bronchogenic carcinoma by an innovated high-dose en-bloc radiotherapeutic approach *Cancer* **48** 101-9

Colgan R, McClelland J, McQuaid D, Evans P M, Hawkes D, Brock J, Landau D and Webb S 2008 Planning lung radiotherapy using 4D CT data and a motion model *Phys Med Biol* **53** 5815-30

Coolens C, Webb S, Shirato H, Nishioka K and Evans P M 2008 A margin model to account for respiration-induced tumour motion and its variability *Phys Med Biol* **53** 4317-30

Crawford C R, King K F, Ritchie C J and Godwin J D 1996 Respiratory compensation in projection imaging using a magnification and displacement model *IEEE Trans Med Imaging* **15** 327-32

Cui Y, Dy J G, Alexander B and Jiang S B 2008 Fluoroscopic gating without implanted fiducial markers for lung cancer radiotherapy based on support vector machines *Phys Med Biol* **53** N315-27

Cui Y, Dy J G, Sharp G C, Alexander B and Jiang S B 2007a Multiple template-based fluoroscopic tracking of lung tumor mass without implanted fiducial markers *Phys Med Biol* **52** 6229-42

Cui Y, Dy J G, Sharp G C, Alexander B and Jiang S B 2007b Robust fluoroscopic respiratory gating for lung cancer radiotherapy without implanted fiducial markers *Phys Med Biol* **52** 741-55

D'Souza W D, Naqvi S A and Yu C X 2005 Real-time intra-fraction-motion tracking using the treatment couch: a feasibility study *Phys Med Biol* **50** 4021-33

Dawson L A, Brock K K, Kazanjian S, Fitch D, McGinn C J, Lawrence T S, Ten Haken R K and Balter J 2001 The reproducibility of organ position using active breathing control (ABC) during liver radiotherapy *Int J Radiat Oncol Biol Phys* **51** 1410-21

Dhanantwari A C, Stergiopoulos S and Iakovidis I 2001 Correcting organ motion artifacts in x-ray CT medical imaging systems by adaptive processing. I. Theory *Medical Physics* **28** 1562-76

Dietrich L, Jetter S, Tucking T, Nill S and Oelfke U 2006 Linac-integrated 4D cone beam CT: first experimental results *Phys Med Biol* **51** 2939-52

Erridge S C, Seppenwoolde Y, Muller S H, van Herk M, De Jaeger K, Belderbos J S, Boersma L J and Lebesque J V 2003 Portal imaging to assess set-up errors, tumor motion and tumor shrinkage during conformal radiotherapy of non-small cell lung cancer *Radiother Oncol* **66** 75-85

Favaro P and Soatto S 2007 *3-D shape estimation and image restoration : exploiting defocus and motion blur* (London: Springer)

Feldkamp L A, Davis L C and Kress J W 1984 Practical Cone-Beam Algorithm *Journal of the Optical Society of America a-Optics Image Science and Vision* **1** 612-9

Ford E C, Mageras G S, Yorke E and Ling C C 2003 Respiration-correlated spiral CT: a method of measuring respiratory-induced anatomic motion for radiation treatment planning *Med Phys* **30** 88-97

Freund E, Heinze F and Rossmann J 2004 Direction dependent projection fields for the fast DRR generation for medical 2D/3D registration *Conf Proc IEEE Eng Med Biol Soc* **3** 1751-4

Geraghty P R, Kee S T, McFarlane G, Razavi M K, Sze D Y and Dake M D 2003 CT-guided transthoracic needle aspiration biopsy of pulmonary nodules: needle size and pneumothorax rate *Radiology* **229** 475-81

Group U S C S W 2009 United States Cancer Statistics: 1999-2005 Incidence and Mortality Web-based Report *U.S. Department of Health and Human Services, Center for Disease Control and Prevention and National Cancer Institute*

Haasbeek C J, Spoelstra F O, Lagerwaard F J, van Sornsen de Koste J R, Cuijpers J P, Slotman B J and Senan S 2008 Impact of audio-coaching on the position of lung tumors *Int J Radiat Oncol Biol Phys* **71** 1118-23

Hajnal J V, Hawkes D J and Hill D L G 2001 *Medical image registration* (Boca Raton: CRC Press)

Hall E J and Giaccia A J 2006 *Radiobiology for the radiologist* (Philadelphia: Lippincott Williams & Wilkins)

Heath E, Unkelbach J and Oelfke U 2009 Incorporating uncertainties in respiratory motion into 4D treatment plan optimization *Med Phys* **36** 3059-71

Henzel M, Hamm K, Sitter H, Gross M W, Surber G, Kleinert G and Engenhart-Cabillic R 2009 Comparison of stereotactic radiosurgery and fractionated stereotactic radiotherapy of acoustic neurinomas according to 3-D tumor volume shrinkage and quality of life *Strahlenther Onkol* **185** 567-73

Hoisak J D, Sixel K E, Tirona R, Cheung P C and Pignol J P 2004 Correlation of lung tumor motion with external surrogate indicators of respiration *Int J Radiat Oncol Biol Phys* **60** 1298-306

Ionascu D, Jiang S B, Nishioka S, Shirato H and Berbeco R I 2007 Internal-external correlation investigations of respiratory induced motion of lung tumors *Med Phys* **34** 3893-903

Jacobs F, Sundermann E, de Sutter B, Christiaens M and Lemahieu I 1998 A fast algorithm to calculate the exact radiological path through a pixel of voxel space *Journal of Computing and Information Technology - CIT* **6** 89-94

Jaffray D A, Siewerdsen J H, Wong J W and Martinez A A 2002 Flat-panel cone-beam computed tomography for image-guided radiation therapy *Int J Radiat Oncol Biol Phys* **53** 1337-49

Jiang S B 2006 Technical aspects of image-guided respiration-gated radiation therapy *Med Dosim* **31** 141-51

Jiang S B, Pope C, Al Jarrah K M, Kung J H, Bortfeld T and Chen G T 2003 An experimental investigation on intra-fractional organ motion effects in lung IMRT treatments *Phys Med Biol* **48** 1773-84

Jiang S B, Wolfgang J and Mageras G S 2008 Quality assurance challenges for motion-adaptive radiation therapy: gating, breath holding, and four-dimensional computed tomography *Int J Radiat Oncol Biol Phys* **71** S103-7

Kak A C, Slaney M and IEEE Engineering in Medicine and Biology Society. 1988 *Principles of computerized tomographic imaging* (New York: IEEE Press)

Kanoulas E, Aslam J A, Sharp G C, Berbeco R I, Nishioka S, Shirato H and Jiang S B 2007 Derivation of the tumor position from external respiratory surrogates with periodical updating of the internal/external correlation *Phys Med Biol* **52** 5443-56

Katsaggelos A K 1991 *Digital image restoration* (Berlin ; New York: Springer-Verlag)

Keall P J, Kini V R, Vedam S S and Mohan R 2001 Motion adaptive x-ray therapy: a feasibility study *Phys Med Biol* **46** 1-10

Keall P J, Mageras G S, Balter J M, Emery R S, Forster K M, Jiang S B, Kapatoes J M, Low D A, Murphy M J, Murray B R, Ramsey C R, Van Herk M B, Vedam S S, Wong J W and Yorke E 2006 The management of respiratory motion in radiation oncology report of AAPM Task Group 76 *Med Phys* **33** 3874-900

Keall P J, Starkschall G, Shukla H, Forster K M, Ortiz V, Stevens C W, Vedam S S, George R, Guerrero T and Mohan R 2004 Acquiring 4D thoracic CT scans using a multislice helical method *Phys Med Biol* **49** 2053-67

Kim R Y and Spencer S A 2000 Tumor shrinkage before intracavitary brachytherapy for cancer of the cervix: radiotherapy alone versus concurrent chemoradiotherapy *Cancer J* **6** 377-80

Kini V R, Vedam S S, Keall P J, Patil S, Chen C and Mohan R 2003 Patient training in respiratory-gated radiotherapy *Med Dosim* **28** 7-11

Kopans D B 2006 The effect of changes in tumor size on breast carcinoma survival in the U.S.: 1975-1999 *Cancer* **106** 1863; author reply 4

Kubo H D, Len P M, Minohara S and Mostafavi H 2000 Breathing-synchronized radiotherapy program at the University of California Davis Cancer Center *Med Phys* **27** 346-53

Lacroute P and Levoy M 1994 Fast volume rendering using a shear-warp factorization of the viewing transformation *Proceedings of the 21st Annual Conference on Computer Graphics and Interactive Techniques* 451-8

Langen K M, Meeks S L, Poole D O, Wagner T H, Willoughby T R, Kupelian P A, Ruchala K J, Haimerl J and Olivera G H 2005 The use of megavoltage CT (MVCT) images for dose recomputations *Phys Med Biol* **50** 4259-76

Lemieux L, Jagoe R, Fish D R, Kitchen N D and Thomas D G T 1994 A Patient-to-Computed-Tomography Image Registration Method Based on Digitally Reconstructed Radiographs *Medical Physics* **21** 1749-60

Leong J 1987 Implementation of random positioning error in computerised radiation treatment planning systems as a result of fractionation *Phys Med Biol* **32** 327-34

Levoy M, Ng R, Adams A, Footer M and Horowitz M 2006 Light field microscopy *Acm Transactions on Graphics* **25** 924-34

Lewis J H and Jiang S B 2009 A theoretical model for respiratory motion artifacts in free-breathing CT scans *Phys Med Biol* **54** 745-55

Lewis J H, Li R, Watkins W T, Cervino L I, Lawson J D, Song W Y and Jiang S 2009 Markerless lung tumor tracking in rotational radiotherapy *Med Phys* **36** 2494

Li R, Lewis J H, Cervino L I and Jiang S B 2009a 4D CT sorting based on patient internal anatomy *Phys Med Biol* **54** 4821-33

Li R, Lewis J H, Cervino L I and Jiang S B 2009b A feasibility study of markerless fluoroscopic gating for lung cancer radiotherapy using 4DCT templates *Phys Med Biol* **54** N489-500

Li T, Koong A and Xing L 2007 Enhanced 4D cone-beam CT with inter-phase motion model *Med Phys* **34** 3688-95

Li T, Schreibmann E, Yang Y and Xing L 2006a Motion correction for improved target localization with on-board cone-beam computed tomography *Phys Med Biol* **51** 253-67

Li T and Xing L 2007 Optimizing 4D cone-beam CT acquisition protocol for external beam radiotherapy *Int J Radiat Oncol Biol Phys* **67** 1211-9

Li T, Xing L, Munro P, McGuinness C, Chao M, Yang Y, Loo B and Koong A 2006b Four-dimensional cone-beam computed tomography using an on-board imager *Med Phys* **33** 3825-33

Lin T, Cervino L I, Tang X, Vasconcelos N and Jiang S B 2009a Fluoroscopic tumor tracking for image-guided lung cancer radiotherapy *Phys Med Biol* **54** 981-92

Lin T, Li R, Tang X, Dy J G and Jiang S B 2009b Markerless gating for lung cancer radiotherapy based on machine learning techniques *Phys Med Biol* **54** 1555-63

Linney N C and Gregson P H 2001 Organ motion detection in CT images using opposite rays in fan-beam projection systems *Ieee Transactions on Medical Imaging* **20** 1109-22

Liu Y L, Wang J, Chen X, Guo Y W and Peng Q S 2008 A robust and fast non-local means algorithm for image denoising *Journal of Computer Science and Technology* **23** 270-9

Lotz H T, Pos F J, Hulshof M C, van Herk M, Lebesque J V, Duppen J C and Remeijer P 2006 Tumor motion and deformation during external radiotherapy of bladder cancer *Int J Radiat Oncol Biol Phys* **64** 1551-8

Low D A, Nystrom M, Kalinin E, Parikh P, Dempsey J F, Bradley J D, Mutic S, Wahab S H, Islam T, Christensen G, Politte D G and Whiting B R 2003 A method for the reconstruction of four-dimensional synchronized CT scans acquired during free breathing *Med Phys* **30** 1254-63

Lucy L B 1974 Iterative Technique for Rectification of Observed Distributions *Astronomical Journal* **79** 745-54

Lujan A E, Larsen E W, Balter J M and Ten Haken R K 1999 A method for incorporating organ motion due to breathing into 3D dose calculations *Med Phys* **26** 715-20

Mageras G S, Pevsner A, Yorke E D, Rosenzweig K E, Ford E C, Hertanto A, Larson S M, Lovelock D M, Erdi Y E, Nehmeh S A, Humm J L and Ling C C 2004 Measurement of lung tumor motion using respiration-correlated CT *Int J Radiat Oncol Biol Phys* **60** 933-41

Mageras G S, Yorke E, Rosenzweig K, Braban L, Keatley E, Ford E, Leibel S A and Ling C C 2001 Fluoroscopic evaluation of diaphragmatic motion reduction with a respiratory gated radiotherapy system *J Appl Clin Med Phys* **2** 191-200

Markman M 1996 What does tumor shrinkage mean to the patient receiving chemotherapy? *Cleve Clin J Med* **63** 301-2

Martel M K, Ten Haken R K, Hazuka M B, Kessler M L, Strawderman M, Turrisi A T, Lawrence T S, Fraass B A and Lichter A S 1999 Estimation of tumor control probability model parameters from 3-D dose distributions of non-small cell lung cancer patients *Lung Cancer* **24** 31-7

Maxim P G, Loo B W, Jr., Shirazi H, Thorndyke B, Luxton G and Le Q T 2007 Quantification of motion of different thoracic locations using four-dimensional computed tomography: implications for radiotherapy planning *Int J Radiat Oncol Biol Phys* **69** 1395-401

McGarry R C, Papiez L, Williams M, Whitford T and Timmerman R D 2005 Stereotactic body radiation therapy of early-stage non-small-cell lung carcinoma: phase I study *Int J Radiat Oncol Biol Phys* **63** 1010-5

McLaughlin P W, Narayana V, Kessler M, McShan D, Troyer S, Marsh L, Hixson G and Roberson P L 2004 The use of mutual information in registration of CT and MRI datasets post permanent implant *Brachytherapy* **3** 61-70

McShan D L, Kessler M L, Vineberg K and Fraass B A 2006 Inverse plan optimization accounting for random geometric uncertainties with a multiple instance geometry approximation (MIGA) *Med Phys* **33** 1510-21

Meeks S L, Harmon J F, Jr., Langen K M, Willoughby T R, Wagner T H and Kupelian P A 2005 Performance characterization of megavoltage computed tomography imaging on a helical tomotherapy unit *Med Phys* **32** 2673-81

Melmed S, Sternberg R, Cook D, Klibanski A, Chanson P, Bonert V, Vance M L, Rhew D, Kleinberg D and Barkan A 2005 A critical analysis of pituitary tumor shrinkage during primary medical therapy in acromegaly *J Clin Endocrinol Metab* **90** 4405-10

Moser T, Biederer J, Nill S, Remmert G and Bendl R 2008 Detection of respiratory motion in fluoroscopic images for adaptive radiotherapy *Phys Med Biol* **53** 3129-45

Murphy M J, Adler J R, Jr., Bodduluri M, Dooley J, Forster K, Hai J, Le Q, Luxton G, Martin D and Poen J 2000 Image-guided radiosurgery for the spine and pancreas *Comput Aided Surg* **5** 278-88

Mutaf Y D and Brinkmann D H 2008 Optimization of internal margin to account for dosimetric effects of respiratory motion *Int J Radiat Oncol Biol Phys* **70** 1561-70

Nakamura M, Narita Y, Matsuo Y, Narabayashi M, Nakata M, Sawada A, Mizowaki T, Nagata Y and Hiraoka M 2009 Effect of audio coaching on correlation of abdominal displacement with lung tumor motion *Int J Radiat Oncol Biol Phys* **75** 558-63

Nehmeh S A, Erdi Y E, Ling C C, Rosenzweig K E, Squire O D, Braban L E, Ford E, Sidhu K, Mageras G S, Larson S M and Humm J L 2002 Effect of respiratory gating on reducing lung motion artifacts in PET imaging of lung cancer *Med Phys* **29** 366-71

Neicu T, Shirato H, Seppenwoolde Y and Jiang S B 2003 Synchronized moving aperture radiation therapy (SMART): average tumour trajectory for lung patients *Phys Med Biol* **48** 587-98

Nelson C, Starkschall G, Balter P, Morice R C, Stevens C W and Chang J Y 2007 Assessment of lung tumor motion and setup uncertainties using implanted fiducials *Int J Radiat Oncol Biol Phys* **67** 915-23

Nishioka S, Nishioka T, Kawahara M, Tanaka S, Hiromura T, Tomita K and Shirato H 2008 Exhale fluctuation in respiratory-gated radiotherapy of the lung: a pitfall of respiratory gating shown in a synchronized internal/external marker recording study *Radiother Oncol* **86** 69-76

Okunieff P, Morgan D, Niemierko A and Suit H D 1995 Radiation dose-response of human tumors *Int J Radiat Oncol Biol Phys* **32** 1227-37

Oldham M, Letourneau D, Watt L, Hugo G, Yan D, Lockman D, Kim L H, Chen P Y, Martinez A and Wong J W 2005 Cone-beam-CT guided radiation therapy: A model for on-line application *Radiother Oncol* **75** 271-8

Ozhasoglu C and Murphy M J 2002 Issues in respiratory motion compensation during external-beam radiotherapy *Int J Radiat Oncol Biol Phys* **52** 1389-99

Panakis N, McNair H A, Christian J A, Mendes R, Symonds-Tayler J R, Knowles C, Evans P M, Bedford J and Brada M 2008 Defining the margins in the radical radiotherapy of non-small cell lung cancer (NSCLC) with active breathing control (ABC) and the effect on physical lung parameters *Radiother Oncol* **87** 65-73

Papiez L, McMahon R and Timmerman R 2007 4D DMLC leaf sequencing to minimize organ at risk dose in moving anatomy *Med Phys* **34** 4952-6

Papiez L and Rangaraj D 2005 DMLC leaf-pair optimal control for mobile, deforming target *Med Phys* **32** 275-85

Peng H, Long F and Ding C 2005 Feature selection based on mutual information: criteria of max-dependency, max-relevance, and min-redundancy *IEEE Trans Pattern Anal Mach Intell* **27** 1226-38

Penney G P, Batchelor P G, Hill D L G, Hawkes D J and Weese J 2001 Validation of a two- to three-dimensional registration algorithm for aligning preoperative CT images and intraoperative fluoroscopy images *Medical Physics* **28** 1024-32

Penney G P, Weese J, Little J A, Desmedt P, Hill D L G and Hawkes D J 1998 A comparison of similarity measures for use in 2-D-3-D medical image registration *Ieee Transactions on Medical Imaging* **17** 586-95

Perez C A, Pajak T F, Rubin P, Simpson J R, Mohiuddin M, Brady L W, Perez-Tamayo R and Rotman M 1987 Long-term observations of the patterns of failure in patients with unresectable non-oat cell carcinoma of the lung treated with definitive radiotherapy. Report by the Radiation Therapy Oncology Group *Cancer* **59** 1874-81

Perez C A, Stanley K, Rubin P, Kramer S, Brady L, Perez-Tamayo R, Brown G S, Concannon J, Rotman M and Seydel H G 1980 A prospective randomized study of various irradiation doses and fractionation schedules in the treatment of inoperable non-oat-cell carcinoma of the lung. Preliminary report by the Radiation Therapy Oncology Group *Cancer* **45** 2744-53

Piessevaux H, Buyse M, De Roock W, Prenen H, Schlichting M, Van Cutsem E and Tejpar S 2009 Radiological tumor size decrease at week 6 is a potent predictor of outcome in chemorefractory metastatic colorectal cancer treated with cetuximab (BOND trial) *Ann Oncol* **20** 1375-82

Popescu C C, Olivotto I A, Beckham W A, Ansbacher W, Zavgorodni S, Shaffer R, Wai E S and Otto K 2009 Volumetric Modulated Arc Therapy Improves Dosimetry and Reduces Treatment Time Compared To Conventional Intensity-Modulated Radiotherapy for Locoregional Radiotherapy of Left-Sided Breast Cancer and Internal Mammary Nodes *Int J Radiat Oncol Biol Phys*

Pouliot J, Bani-Hashemi A, Chen J, Svatos M, Ghelmansarai F, Mitschke M, Aubin M, Xia P, Morin O, Bucci K, Roach M, 3rd, Hernandez P, Zheng Z, Hristov D and Verhey L 2005 Low-dose megavoltage cone-beam CT for radiation therapy *Int J Radiat Oncol Biol Phys* **61** 552-60

Poulsen P R, Cho B and Keall P J 2008 A method to estimate mean position, motion magnitude, motion correlation, and trajectory of a tumor from cone-beam CT projections for image-guided radiotherapy *Int J Radiat Oncol Biol Phys* **72** 1587-96

Puglisi F, Mansutti M, Aprile G, Minisini A M, Di Loreto C, Bazzocchi M, Londero V, Cedolini C, Gentile G, Pizzolitto S, Piga A and Sobrero A 2004 Tumor shrinkage evaluation during and after preoperative doxorubicin and cyclophosphamide followed by docetaxel in patients with breast cancer *Anticancer Res* **24** 2487-93

Reyes M, Malandain G, Koulibaly P M, Gonzalez-Ballester M A and Darcourt J 2007 Model-based respiratory motion compensation for emission tomography image reconstruction *Physics in Medicine and Biology* **52** 3579-600

Richards.Wh 1972 Bayesian-Based Iterative Method of Image Restoration *Journal of the Optical Society of America* **62** 55-&

Richter A, Baier K, Meyer J, Wilbert J, Krieger T, Flentje M and Guckenberger M 2008 Influence of increased target dose inhomogeneity on margins

for breathing motion compensation in conformal stereotactic body radiotherapy *BMC Med Phys* **8** 5

Rietzel E, Pan T and Chen G T 2005 Four-dimensional computed tomography: image formation and clinical protocol *Med Phys* **32** 874-89

Rit S and Sarrut D 2007 Cone-beam projection of a deformable volume for motion compensated algebraic reconstruction *Conf Proc IEEE Eng Med Biol Soc* **2007** 6544-7

Rit S, Sarrut D and Desbat L 2009a Comparison of analytic and algebraic methods for motion-compensated cone-beam CT reconstruction of the thorax *IEEE Trans Med Imaging* **28** 1513-25

Rit S, Wolthaus J, van Herk M and Sonke J J 2008 On-the-fly motion-compensated cone-beam CT using an a priori motion model *Med Image Comput Comput Assist Interv* **11** 729-36

Rit S, Wolthaus J W, van Herk M and Sonke J J 2009b On-the-fly motion-compensated cone-beam CT using an a priori model of the respiratory motion *Med Phys* **36** 2283-96

Ritchie C J, Crawford C R, Godwin J D, King K F and Kim Y 1996 Correction of computed tomography motion artifacts using pixel-specific back-projection *Ieee Transactions on Medical Imaging* **15** 333-42

Rohlfing T, Denzler J, Grassl C, Russakoff D B and Maurer C R 2005 Markerless real-time 3-D target region tracking by motion backprojection from projection images *Ieee Transactions on Medical Imaging* **24** 1455-68

Ruan D, Fessler J A, Balter J M, Berbeco R I, Nishioka S and Shirato H 2008 Inference of hysteretic respiratory tumor motion from external surrogates: a state augmentation approach *Phys Med Biol* **53** 2923-36

Rubinstein L V, Dancey J E, Korn E L, Smith M A and Wright J J 2007 Early average change in tumor size in a phase 2 trial: efficient endpoint or false promise? *J Natl Cancer Inst* **99** 1422-3

Rudin L I, Osher S and Fatemi E 1992 Nonlinear Total Variation Based Noise Removal Algorithms *Physica D* **60** 259-68

Schweikard A, Glosser G, Bodduluri M, Murphy M J and Adler J R 2000 Robotic motion compensation for respiratory movement during radiosurgery *Comput Aided Surg* **5** 263-77

Segars W 2001 Development of a new dynamic NURBS-based cardiac-torso (NCAT) phantom. (Chapel Hill, NC: The University of North Carolina)

Segars W P, Lalush D S and Tsui B M W 1999 A realistic spline-based dynamic heart phantom *Ieee Transactions on Nuclear Science* **46** 503-6

Segars W P, Lalush D S and Tsui B M W 2001 Modeling respiratory mechanics in the MCAT and spline-based MCAT phantoms *Ieee Transactions on Nuclear Science* **48** 89-97

Seiler P G, Blattmann H, Kirsch S, Muench R K and Schilling C 2000 A novel tracking technique for the continuous precise measurement of tumour positions in conformal radiotherapy *Physics in Medicine and Biology* **45** N103-N10

Senan S, Chapet O, Lagerwaard F J and Ten Haken R K 2004a Defining target volumes for non-small cell lung carcinoma *Semin Radiat Oncol* **14** 308-14

Senan S, De Ruysscher D, Giraud P, Mirimanoff R and Budach V 2004b Literature-based recommendations for treatment planning and execution in high-dose radiotherapy for lung cancer *Radiother Oncol* **71** 139-46

Seppenwoolde Y, Shirato H, Kitamura K, Shimizu S, van Herk M, Lebesque J V and Miyasaka K 2002 Precise and real-time measurement of 3D tumor motion in lung due to breathing and heartbeat, measured during radiotherapy *Int J Radiat Oncol Biol Phys* **53** 822-34

Sharp G C, Jiang S B, Shimizu S and Shirato H 2004 Tracking errors in a prototype real-time tumour tracking system *Phys Med Biol* **49** 5347-56

Shirato H, Suzuki K, Sharp G C, Fujita K, Onimaru R, Fujino M, Kato N, Osaka Y, Kinoshita R, Taguchi H, Onodera S and Miyasaka K 2006 Speed and amplitude of lung tumor motion precisely detected in four-dimensional setup and in real-time tumor-tracking radiotherapy *Int J Radiat Oncol Biol Phys* **64** 1229-36

Siddon R L 1985 Fast calculation of the exact radiological path for a three-dimensional CT array *Med Phys* **12** 252-5

Smith S M and Brady J M 1997 SUSAN - A new approach to low level image processing *International Journal of Computer Vision* **23** 45-78

Song Y, Zhang P, Wang P, Obcemea C, Mueller B, Burman C and Mychalczak B 2009 The development of a novel radiation treatment modality - volumetric modulated arc therapy *Conf Proc IEEE Eng Med Biol Soc* **1** 3401-4

Sonke J J, Lebesque J and van Herk M 2008 Variability of four-dimensional computed tomography patient models *Int J Radiat Oncol Biol Phys* **70** 590-8

Sonke J J, Zijp L, Remeijer P and van Herk M 2005 Respiratory correlated cone beam CT *Med Phys* **32** 1176-86

Spoelstra F O, van Sornsen de Koste J R, Cuijpers J P, Lagerwaard F J, Slotman B J and Senan S 2008 Analysis of reproducibility of respiration-triggered gated radiotherapy for lung tumors *Radiother Oncol* **87** 59-64

Starkschall G, Desai N, Balter P, Prado K, Luo D, Cody D and Pan T 2007 Quantitative assessment of four-dimensional computed tomography image acquisition quality *J Appl Clin Med Phys* **8** 2362

Suh Y, Yi B, Ahn S, Kim J, Lee S, Shin S and Choi E 2004 Aperture maneuver with compelled breath (AMC) for moving tumors: a feasibility study with a moving phantom *Med Phys* **31** 760-6

Taguchi K 2003 Temporal resolution and the evaluation of candidate algorithms for four-dimensional CT *Med Phys* **30** 640-50

Tang X, Sharp G C and Jiang S B 2007 Fluoroscopic tracking of multiple implanted fiducial markers using multiple object tracking *Phys Med Biol* **52** 4081-98

Thurfjell L, Lau Y H, Andersson J L and Hutton B F 2000 Improved efficiency for MRI-SPET registration based on mutual information *Eur J Nucl Med* **27** 847-56

Trofimov A, Rietzel E, Lu H M, Martin B, Jiang S, Chen G T and Bortfeld T 2005 Temporo-spatial IMRT optimization: concepts, implementation and initial results *Phys Med Biol* **50** 2779-98

Tsunashima Y, Sakae T, Shioyama Y, Kagei K, Terunuma T, Nohtomi A and Akine Y 2004 Correlation between the respiratory waveform measured using a respiratory sensor and 3D tumor motion in gated radiotherapy *Int J Radiat Oncol Biol Phys* **60** 951-8

Tuma R S 2006 Sometimes size doesn't matter: reevaluating RECIST and tumor response rate endpoints *J Natl Cancer Inst* **98** 1272-4

Unkelbach J and Oelfke U 2005 Incorporating organ movements in inverse planning: assessing dose uncertainties by Bayesian inference *Phys Med Biol* **50** 121-39

van der Weide L, van Sornsen de Koste J R, Lagerwaard F J, Vincent A, van Triest B, Slotman B J and Senan S 2008 Analysis of carina position as

surrogate marker for delivering phase-gated radiotherapy *Int J Radiat Oncol Biol Phys* **71** 1111-7

Van Dyk J 1999 *The modern technology of radiation oncology : a compendium for medical physicists and radiation oncologists* (Madison, Wis.: Medical Physics Pub.)

van Herk M 2004 Errors and margins in radiotherapy *Semin Radiat Oncol* **14** 52-64

Vedam S S, Keall P J, Kini V R and Mohan R 2001 Determining parameters for respiration-gated radiotherapy *Med Phys* **28** 2139-46

Vedam S S, Keall P J, Kini V R, Mostafavi H, Shukla H P and Mohan R 2003a Acquiring a four-dimensional computed tomography dataset using an external respiratory signal *Phys Med Biol* **48** 45-62

Vedam S S, Kini V R, Keall P J, Ramakrishnan V, Mostafavi H and Mohan R 2003b Quantifying the predictability of diaphragm motion during respiration with a noninvasive external marker *Med Phys* **30** 505-13

Wang G and Vannier M W 1995 Preliminary-Study on Helical Ct Algorithms for Patient Motion Estimation and Compensation *Ieee Transactions on Medical Imaging* **14** 205-11

Wang J, Li T and Xing L 2009 Iterative image reconstruction for CBCT using edge-preserving prior *Med Phys* **36** 252-60

Wang Z, Wu Q J, Marks L B, Larrier N and Yin F F 2007 Cone-beam CT localization of internal target volumes for stereotactic body radiotherapy of lung lesions *Int J Radiat Oncol Biol Phys* **69** 1618-24

Willis N P and Bresler Y 1995 Optimal Scan for Time-Varying Tomography .1. Theoretical-Analysis and Fundamental Limitations *Ieee Transactions on Image Processing* **4** 642-53

Wolff D, Stieler F, Welzel G, Lorenz F, Abo-Madyan Y, Mai S, Herskind C, Polednik M, Steil V, Wenz F and Lohr F 2009 Volumetric modulated arc therapy (VMAT) vs. serial tomotherapy, step-and-shoot IMRT and 3D-conformal RT for treatment of prostate cancer *Radiother Oncol* **93** 226-33

Wu H, Zhao Q, Berbeco R I, Nishioka S, Shirato H and Jiang S B 2008a Gating based on internal/external signals with dynamic correlation updates *Phys Med Biol* **53** 7137-50

Wu J, Li H, Shekhar R, Suntharalingam M and D'Souza W 2008b An evaluation of planning techniques for stereotactic body radiation therapy in lung tumors *Radiother Oncol* **87** 35-43

Wulf J, Baier K, Mueller G and Flentje M P 2005 Dose-response in stereotactic irradiation of lung tumors *Radiother Oncol* **77** 83-7

Xu Q, Hamilton R J, Schowengerdt R A, Alexander B and Jiang S B 2008 Lung tumor tracking in fluoroscopic video based on optical flow *Med Phys* **35** 5351-9

Yang X, Soma T and Murase K 2008 Phase mutual information for MRI and PET image registration: parameter selection of Log-Gabor filter *Igaku Butsuri* **27** 117-28

Yang Y, Schreibmann E, Li T, Wang C and Xing L 2007 Evaluation of on-board kV cone beam CT (CBCT)-based dose calculation *Phys Med Biol* **52** 685-705

Yeung A R, Li J G, Shi W, Newlin H E, Chvetsov A, Liu C, Palta J R and Olivier K 2009 Tumor localization using cone-beam CT reduces setup margins in conventionally fractionated radiotherapy for lung tumors *Int J Radiat Oncol Biol Phys* **74** 1100-7

Yokoi T, Soma T, Shinohara H and Matsuda H 2004 Accuracy and reproducibility of co-registration techniques based on mutual information and normalized mutual information for MRI and SPECT brain images *Ann Nucl Med* **18** 659-67

Zhang Q, Pevsner A, Hertanto A, Hu Y C, Rosenzweig K E, Ling C C and Mageras G S 2007 A patient-specific respiratory model of anatomical motion for radiation treatment planning *Med Phys* **34** 4772-81

Zhulina Y V 2006 Multiframe blind deconvolution of heavily blurred astronomical images *Applied Optics* **45** 7342-52